The Dissertation Committee for Steven Joseph Younghouse
Certifies that this is the approved version of the following dissertation:

IRRADIATION OF AN ELASTIC PLATE BY A FINITE-AMPLITUDE SOUND BEAM WITH APPLICATIONS TO NONDESTRUCTIVE EVALUATION

Committee:

Mark F. Hamilton, Supervisor

Anthony Bedford

David T. Blackstock

Elmer L. Hixson

Raul G. Longoria

IRRADIATION OF AN ELASTIC PLATE BY A FINITE-AMPLITUDE SOUND BEAM WITH APPLICATIONS TO NONDESTRUCTIVE EVALUATION

by

STEVEN JOSEPH YOUNGHOUSE, B.S., M.S.

DISSERTATION

Presented to the Faculty of the Graduate School of
The University of Texas at Austin
in Partial Fulfillment
of the Requirements
for the Degree of

DOCTOR OF PHILOSOPHY

THE UNIVERSITY OF TEXAS AT AUSTIN

August, 2002

To my Father

ACKNOWLEDGMENTS

I extend my heartfelt gratitude to my supervising professor, Dr. Mark F. Hamilton, whose guidance, assistance, and patience has been invaluable to this research and to my education in the field of acoustics. His continual motivation has contributed greatly to my growth as a student.

Dr. David T. Blackstock, Dr. A. Marc Bedford, Dr. Raul G. Longoria, and Dr. Elmer L. Hixson are thanked for serving as members of the dissertation committee, and for their helpful suggestions.

I would like to thank Dr. B.J. Landsberger for teaching me to operate the ultrasonic apparatus used in this work.

I would also like to thank Dr. Won-Suk Ohm, Dr. Pennia Menounou, and Dr. Douglas Meegan for their suggestions, help, and friendship over the time during which this work was done. Their support has eased immeasurably the many frustrations I faced while undertaking this project.

Many thanks go to Dr. Gary Wilson for his patience during the completion of this dissertation.

Last, but certainly not least, I thank my family (including Brian) for their many years of continual support and love. I especially thank my wife Cindy, without whose inspiration, patience, and support I would not have been able to complete this work.

This work was supported by the National Science Foundation and by the Office of Naval Research.

August, 2002

IRRADIATION OF AN ELASTIC PLATE BY A FINITE-AMPLITUDE SOUND BEAM WITH APPLICATIONS TO NONDESTRUCTIVE EVALUATION

Publication No. _____

Steven Joseph Younghouse, Ph.D.

The University of Texas at Austin, 2002

Supervisor: Mark F. Hamilton

This dissertation describes an investigation of nonlinear effects associated with the interaction of ultrasound with plates. The overriding goal is to assess the potential for using immersion techniques to measure the nonlinear acoustical parameters of plates. Three measurement configurations are described, with both theory and experiment reported. Effects of weak nonlinearity are included in the theoretical models. In the first configuration, the goal is to characterize the nonlinear elastic response of an isotropic, homogeneous plate. Plate resonances were used to enhance the nonlinear acoustical response. An experiment was performed with an aluminum plate in water, but nonlinearity due to wave propagation in the plate could not be distinguished from the nonlinear effects associated with

propagation of sound through the surrounding fluid. In the second configuration, the interaction of ultrasound with bonded plates is considered. In the theoretical model, nonlinear effects are assumed to occur only at the bond. Particular attention is paid to changes in the reflection and transmission coefficients, as well as the second harmonic radiated from the plate, as a function of bond stiffness. Experiments were performed using bonded aluminum and acrylic plates. Measurements are in qualitative agreement with linear theory, but nonlinear effects at the bond were not observed. In the first two configurations, nonlinearity within the plate is taken into account, but not diffraction of the ultrasound beams. In the third configuration, the interaction of a sound beam with a plate at oblique incidence is examined. Here, beam diffraction is taken into account, but plate nonlinearity is considered to be negligible. The theoretical model is based on an angular spectrum method, and accounts for Lamb wave propagation within the plate. At Lamb excitation angles, nonspecular effects occur in the reflected and transmitted sound beams. Second harmonic generation is assumed to occur only in the fluid. Experiments were performed on an aluminum plate in water, and quantitative agreement is found between theory and measurements.

Contents

Chapter 1

INTRODUCTION

Acoustic waves provide a useful means of interrogating a solid to determine its material characteristics and structural integrity. Researchers and practitioners have utilized bulk compressional and shear waves, surface waves, guided waves in plates, and resonance phenomena to characterize materials. Characterization using acoustic waves is advantageous because it is nondestructive and can be performed rapidly. Also, inspection of objects using acoustic waves can often be performed in the field.

Traditional methods for nondestructive evaluation (NDE) using sound waves are based on small-signal acoustic propagation. Information about the structure is obtained by measuring changes in the magnitude and phase (or time delay) of the received signals. These methods can be used to measure two elastic properties of an isotropic solid, e.g., the bulk and shear moduli. Variations observed in these moduli, typically on the order of a few percent, can indicate damage or fatigue in the material.

Of particular interest in recent years has been the finite-amplitude response of an insonified object. The nonlinear response of a material can provide insights into the microstructure of the material. For example, it can be used to examine precipitates in metals, as well as dislocations.[1] Also, the nonlinear elastic properties of a material have been found to be much more sensitive to fatigue and damage than their linear counterparts. Structural inhomogeneities such as dislocations and microcracks can increase the nonlinearity of a solid by orders of magnitude.[2] Linear material parameters, in contrast, are typically relatively insensitive to the presence of these inhomogeneities. Because of this increased sensitivity, measurements of nonlinear effects show promise in NDE applications. Inclusion of nonlinear effects is also important for correctly modeling acoustic propagation in materials with large parameters of nonlinearity.

The most commonly studied manifestation of acoustic nonlinearity is waveform distortion, which is equivalent to the generation of new frequencies. These new frequencies are usually harmonics of a primary signal, or intermodulation components created by waves propagating in the object at different frequencies. The generation of new frequencies is readily measurable, and thus provides a convenient means of quantifying the nonlinearity of a material. For these reasons we shall pay particular attention to the nonlinear generation of new frequencies in this dissertation.

A variety of experimental configurations have been used to measure the nonlinearity of solids and liquids. Many of these configurations are illustrated in Fig. 1.1 (taken from the review article by Zheng *et al.*[1]). In Figs. 1.1(a) and (b), the nonlinearity of the solid and liquid, respectively, is determined by measuring the dependence of the small-signal sound speed on an applied load or pressure (both designated P). The finite-amplitude method is employed in Figs. 1.1(c)–(f). In this method, the nonlinearity is determined by measuring harmonic generation by acoustic waves propagating through the sample. In Fig. 1.1(g) the sample is modulated by a low-frequency signal at frequency Ω, usually near a natural frequency of the sample, and the nonlinearity of the sample is determined by measuring the intermodulation components frequencies $\omega \pm \Omega$ due to interaction with a probe wave of frequency ω (typically $\omega \gg \Omega$).

Figures 1.1(h)–(m) illustrate configurations to measure the nonlinearity of solids and interfaces using surface and shear waves. Some of these methods [i.e., Figs. 1.1(j)–(l)] involve a static load applied to the interface between two solids.

A great deal of the work in linear acoustical NDE has focused on plates and layers. The ubiquity of plates in structures of all types is readily apparent. Guided acoustic waves can even be used to characterize very thin materials such as paper.[3] Layered materials are also of interest, especially when considering the increased use of laminates and composites in fields such as the aerospace industry. However, little work has been done on nonlinear acoustical NDE of plates. While all the finite-amplitude methods illustrated in Fig. 1.1 rely on

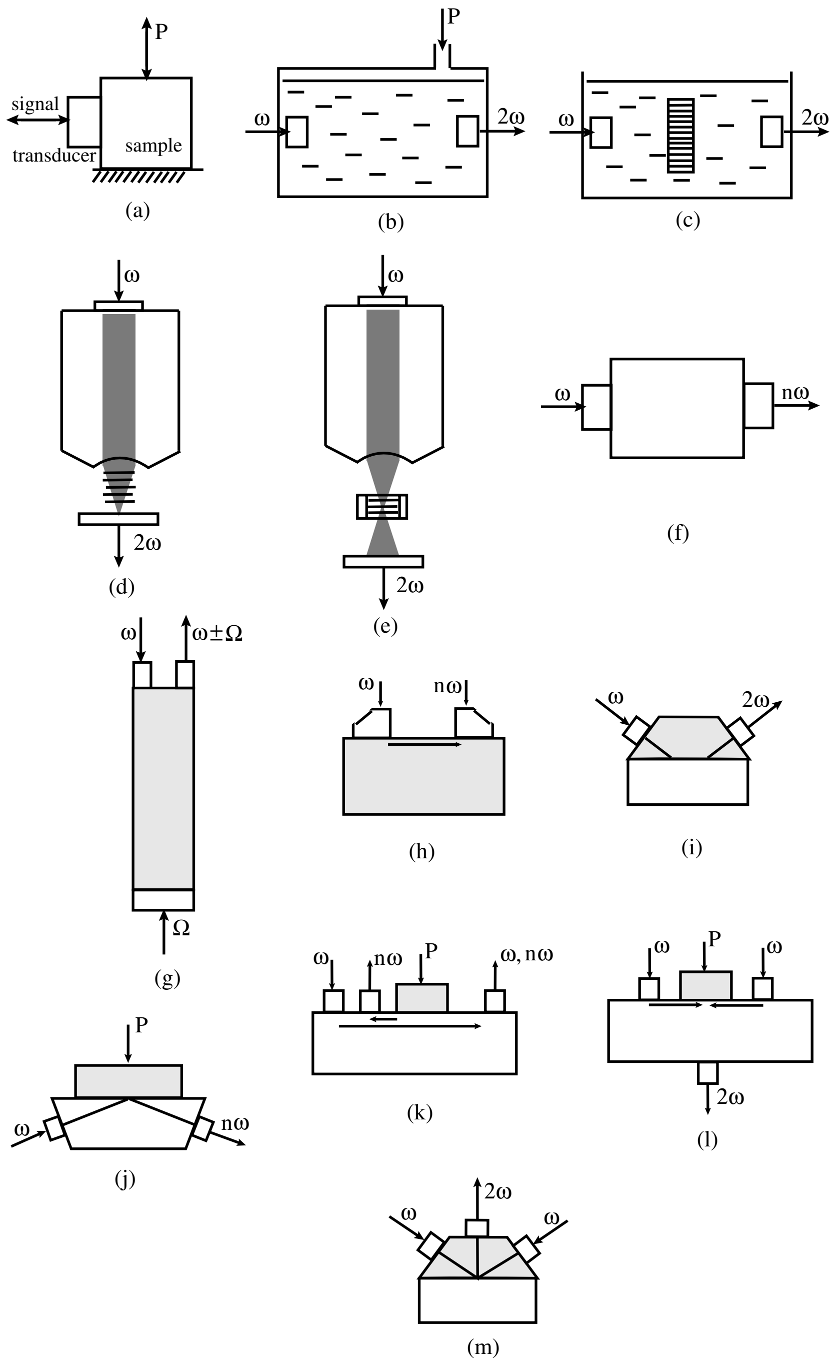

Figure 1.1: Experimental approaches that have been used to investigate nonlinear acoustical approaches to NDE and materials characterization (from Zheng *et al.*[1]).

cumulative nonlinear generation over hundreds of wavelengths for at least one of the waves, for thin plates the acoustic wavelength is typically on the order of the plate thickness. In this case one must therefore rely on resonance effects within the plate to enhance the generation of harmonics over short distances.

The objective of this dissertation is to study the interaction of ultrasound with plates, focusing on potential for use in NDE applications. Models of interactions of ultrasound with plates are presented for three basic situations, with the weakly nonlinear generation of new frequencies taken into account. In the first situation, the objective is to measure the nonlinearity of an isotropic, homogeneous plate using a normally-incident plane wave. In the second situation the single plate is replaced by two plates, joined at a nonlinear planar interface. In the third situation the interaction of a weakly nonlinear sound beam normally incident upon a homogeneous, isotropic plate is examined. We evaluate each of the models by comparison with measurements.

In all three situations the samples are immersed in a fluid bath and irradiated using non-contact transducers. The coupling of a non-contact transducers with a sample is more consistent than the corresponding coupling of a contact transducer. Consistent coupling is especially important when measuring finite-amplitude effects, which depend on the magnitude of the probe wave in the material. Also, when considering industrial applications, non-contact methods offer the advantage of being more easily extended to automated NDE than contact methods.

In Sec. 1.1.1 we discuss earlier investigations in the field of nonlinear acoustic NDE. In Sec. 1.1.2 we review earlier work on the interaction of acoustic waves with plates and layers. Most of this work considered involves small-signal propagation. In Sec. 1.1.3 we review earlier studies of the interaction of sound beams, which have finite beamwidth and exhibit diffraction, with elastic plates and half-spaces. In Sec. 1.1.4 we review earlier studies of the nonlinear interaction of sound beams with homogeneous, isotropic solids. In Sec. 1.2 we present the scope of this dissertation.

1.1 Background

Here we review previous work related to that described in the present dissertation. We have used the concepts discussed by many of these authors, and have extended some of their work. The following discussion is presented to provide context for our investigation, and to clarify the scope of our contribution.

1.1.1 Nonlinear nondestructive evaluation

Acoustic waves have been used for several decades to measure the nonlinearity of solids. Early work focused on the measurement of "classical" nonlinearity, related to the intrinsic structure of the materials on an atomic or molecular scale.[4] This nonlinearity is quantified by the third-order elastic (TOE) constants of a solid.[5] The TOE constants represent the terms at one order higher than associated with the Lamé constants in the Taylor expansion for the strain energy. Third-order elastic constants for anisotropic solids such as crystals have also been studied (see, for example, Ref. 4). In Chap. 2 we consider the effects of classical nonlinearity associated with the TOE constants for a homogeneous, isotropic aluminum plate.

Mechanisms for nonlinearity in solids beyond the intrinsic nonlinearity described by classical models based on TOE constants have received much attention in the last decade.[2,6,7] These types of nonlinearity are often referred to as "anomalous" or "structural," because they are functions of material structure at a scale much larger than interatomic distances, and tend to produce nonlinear responses that are orders of magnitude larger than the intrinsic nonlinearity of a material. At the same time, the linear acoustic parameters of a material are often less sensitive to the presence of these inclusions. Anomalous nonlinear response can occur within the bulk of a solid, or at a boundary between solids. In the work reported in this dissertation we examine only the anomalous nonlinearity at a contact boundary. However, we discuss here some of the work that is related to anomalous nonlinearity distributed throughout the bulk of a solid because it illustrates the large magnitude of the nonlinear effects associated with such media. This in turn is partial motivation for our own work. Also, although experiments in Chap. 2 are performed on an isotropic aluminum plate, the theory developed in that chapter is for a general quadratic nonlinearity in the plate, which includes some features of anomalous nonlinearity.

Over the last decade, researchers have been investigating the potential for using nonlinear ultrasound to evaluate so-called "microinhomogeneous" media,[7,8] that is, media containing inhomogeneities that are small with respect to a wavelength but large compared to interatomic distances.[9] Examples of microinhomogeneous media include rocks, fatigued metals,[10] and materials containing microcracks.[11,12] Because such microinhomogeneities often serve as nuclei for fracture,[13] understanding the response of these materials to acoustic inspection can lead to improved techniques for nondestructive testing. Also, the nonlinearity in solids with microinhomogeneities can be two to four orders of magnitude stronger than nonlinearity in homogeneous solids.[8] For example, Korotkov *et al.*[10] performed experiments on metal samples stressed to different levels of plastic strain. The authors interrogated the samples using high-amplitude, low-frequency "pump" waves, along with lower-amplitude, high-frequency "probe" waves. Nonlinearity was proportional to the magnitudes of the sidebands in the received probe signal. The authors found that the nonlinearity of the samples increased by over an order of magnitude as the samples fatigued.

Researchers have examined the nonlinear acoustic response of granular media.[14–18] Examples of granular media include sand and some rocks, so the nonlinear response of this class of material is of particular interest among Earth scientists. Belyaeva *et al.*[16,17] showed theoretically and experimentally that the heightened quadratic and cubic nonlinearity of granular media is due to the nonlinear force-displacement relationship at the contact between grains. Nonideal packing of the grains was found to further enhance nonlinearity.[17,18]

Nonlinearity in materials with cracks is very important to researchers of nonlinear NDE.[11,12,19] For a solid containing even a low concentration of cracks, the quadratic and cubic parameters of nonlinearity can increase by orders of magnitude, while corresponding changes in the linear elastic parameters are only on the order of one percent.[12] This phenomenon can be envisioned by considering the stress-strain relationship for such a material. In compression, the cracks are closed and the strain in the material is similar to that of a portion of the material without cracks. However, the strain of the material in tension is much larger than it would be if there were no cracks. The disparity causes waveform distortion of a compression wave that propagates in the material. The distortion may be interpreted as harmonic generation. This nonlinearity can be enhanced by using a low-frequency, high-amplitude pump wave to open the cracks, while simultaneously irradiating the sample with a high-frequency probe wave.[11]

Materials that exhibit hysteresis in their stress-strain relationship are another example of a departure from "classical" nonlinearity. Rocks are one class of materials that typically display hysteretic nonlinearity.[14] McCall and Guyer,[20] and later Van den Abeele *et al.*,[21] theoretically studied the nonlinear response of hysteretic materials to elastic waves. The authors modeled rocks as a random distribution of small-scale hysteretic elements. One result found was that the cubic nonlinear response of the hysteretic material is strongly frequency-dependent.

Use of nonlinear ultrasound to evaluate concrete structures has been of interest recently. It has been noted[22] that much of the infrastructure made with concrete in this country is aging, and a reliable way to assess fatigue is badly needed. Traditional, linear ultrasound testing methods are inadequate because concrete is a complex material, and measurements of linear material properties do not always indicate damage reliably. Inspection using nonlinear ultrasound may be a much more accurate means of determining whether a concrete structure is damaged.[23,24]

Next consider contact acoustic nonlinearity (CAN), which arises at the interface between two or more solids. (We address the topic of contact nonlinearity between two plates in Chap. 3.) Considerable interest in CAN has developed over the last few decades.[25–33] Researchers have observed nonlinear effects such as second-harmonic generation,[27–29] intermodulation distortion,[31] and chaos[32] due to CAN. The most basic mechanism of contact nonlinearity is discussed by Richardson,[28] who examined a contact boundary between infinite half-spaces that supports compression, but not tension. The result is a rectification of the acoustic wave transmitted through the boundary as the two media "clap" each other in the presence of wave propagation. Another form of contact nonlinearity results from the force-displacement relationship for two elastic spheres in contact.[34] Nonlinearity of this type is known as Hertzian nonlinearity. The effects of Hertzian nonlinearity on the propagation of acoustic waves through granular media has been studied by a number of authors.[15–18]

Rudenko and Vu[30] modeled CAN at a rough interface between two semi-infinite solids. In their model, the contact boundary is populated by a random distribution of springs with the same stiffness but different lengths. As the compression at the boundary increases, more springs come into contact at the boundary, resulting in an increased stiffness. The resulting nonlinearity in the stress-strain relationship results in distortion of a wave reflected from, or transmitted through, the boundary. Results of this model were found to be in qualitative agreement with related experimental results.[26]

The potential for use of nonlinear NDE to examine the quality of adhesive bonds has been studied, particularly in the last decade.[35–37] In 1991 Achenbach and Parikh[35] proposed measuring nonlinearity at adhesive joints to measure bond quality. They postulated that the nonlinear response of a bond could be used to extrapolate the point at which the stress-strain curve had zero slope. The interrogation methods included both large-amplitude probe waves propagating in free plates and small-amplitude probe waves propagating in pre-stressed plates. Rothenfusser *et al.*[37] examined the second harmonic generated in and through two thin, polished fused silica plates joined with a bond of varying thickness. The authors found that the amplitude of the transmitted second harmonic increased as the adhesive thickness was increased, then reached a maximum at a certain adhesive thickness, and decreased monotonically as the thickness increased further. The explanation the authors gave for the observed behavior was that the second harmonic was generated in the adhesive bond due to resonant amplification of the fundamental within this thin layer.

1.1.2 Interaction of ultrasound with plates and layers

The topic of propagation of acoustic waves in plates and layers is very important in the field of NDE, and a great deal of research has been done on the subject. Plates support propagation of guided waves within the plate, which contain a combination of both compressional and shear components. These waves are known as Lamb waves.[38] One recent focus is the use of Lamb waves for the NDE of composites and laminates.[3] These materials are used increasingly in the aerospace industry, among others, and reliable testing methods need to be developed because of their unique failure characteristics and critical applications.[3,39–42] A thorough review of investigations of Lamb waves is outside the scope of this dissertation, and the interested reader is directed to the literature review by Chimenti.[3]

In this dissertation we consider the interaction of ultrasound with plates immersed in water. If the plate is immersed, the acoustic energy is re-radiated into the fluid. The Lamb wave is then called "leaky." Merkulov[43] determined analytically the attenuation of a leaky Lamb wave due to radiation of the acoustic energy into the fluid. Typical attenuation of a Lamb wave on the order of 1 MHz for a 1 mm thick steel plate in water was found to be on the order of 1 np/cm. For a sound beam whose width is on the order of a few centimeters, this result indicates that the acoustic energy leaked into the fluid from the Lamb wave interferes with the reflected or transmitted sound beam, and thus distorts the beam pattern.

Very little work has been done on the nonlinear propagation of Lamb waves. Because Lamb waves are dispersive, harmonic generation is complicated to predict, and efficient second-harmonic generation occurs only for certain frequencies and modes.[44] In immersed plates, the large attenuation due to leakage hinders the cumulative generation of harmonics due to nonlinearity in the plate.

Small-signal reflection and transmission of a plane wave from an immersed plate has also been thoroughly examined. Any consideration of interactions of a sound beam with a plate involving oblique incidence must include the effects of Lamb waves; however, the focus of these investigations is on the pressure outside of the plate, rather than the guided wave propagating inside the plate. As mentioned previously, because of the leakage of Lamb wave energy into the surrounding fluid, the excitation of Lamb waves has a significant impact on the reflected and transmitted fields. We study this phenomenon in Chap. 4.

One of the first theoretical and experimental studies of transmission of a sound beam through a plate was performed by Schoch.[45] He developed a plane-wave transmssion coefficent for oblique incidence and discussed the connection of transmission phenomena for an immersed plate with the Lamb waves that exist in a free plate. He also modeled transmission of a diffracting sound beam by using a spatial Fourier decomposition of the sound beam into a continuum of plane-wave components that propagate in different directions. This is the technique we use here to account for diffraction in sound beams. In a series of theoretical papers, Fiorito *et al.*[46–50] examined reflection and transmission characteristics of fluid layers and plates. Expressions for transmission and reflection coefficients using a resonance formalism were developed for plane waves at oblique angles of incidence. The authors expanded the reflection and transmission coefficients so that transmission maxima (and reflection minima) were represented as poles and zeros in terms of the expanded transmission and reflection coefficients. For our models we use exact plane-wave reflection and transmission coefficients rather than resonance decompositions. We thus have valid solutions for arbitrary angles of incidence. However, resonance decompositions do provide physical insight.

Guidarelli *et al.*[51,52] performed transmission experiments on immersed elastic plates. The measured effects of Lamb waves on the received sound were found to be in good agreement with the theory of Fiorito *et al.*[48] In 1975 Barnard *et al.*[53] performed experiments on transmission through lossy plates. Their theoretical model made use of plane-wave transmission coefficients derived for lossless plates, and included losses *ad hoc* by rendering the sound speeds complex.

1.1.3 Finite-beamwidth phenomena

In the interaction of sound beams with thick solids and plates, phenomena have been observed that cannot be explained by conventional specular reflection and transmission. Near certain angles of incidence the beam patterns of the reflected and transmitted waves become distorted. The distortions are related to spreading of the sound beams due to the finite lateral dimension of the beam and are thus referred to as finite-beamwidth, or bounded-beam, phenomena. We study these phenomena in Chap. 4.

Along with his studies of the interaction of sound beams with plates,[45] Schoch predicted in 1952 the lateral displacement of a sound beam reflected from a solid at certain angles of incidence.[54] In 1973 Neubauer[55] used Schlieren visualization to study experimentally the reflection of a sound beam from a half-space. In addition to observing a displacement of the reflected sound beam, he observed a null in the reflected field when the angle of incidence of the sound beam was near the Rayleigh angle, which is the angle at which the interface phase velocity equals the speed of the Rayleigh surface wave. Bertoni and Tamir[56] employed an asymptotic analysis to explain the presence of the null as the interference of the specularly reflected sound beam with the leaky Rayleigh wave radiated into the fluid. A complex Laurent expansion, valid only for angles of incidence near the Rayleigh angle, was used to represent the Rayleigh-angle phenomena in terms of poles of the reflection coefficient. Ngoc and Mayer[57] used a numerical method rather than an asymptotic analysis to study changes in the reflected sound beam as the angle of incidence deviated from the Rayleigh angle.

In 1976 Plona *et al.* examined experimentally the reflection and transmission of sound beams through plates.[58] The authors used Schlieren visualization to observe nonspecular effects (similar to those observed by Neubauer for thick solids). These nonspecular phenomena were observed at angles of incidence near Lamb angles of the plate. In 1986 Rousseau and Gatignol[59] used an asymptotic analysis to study nonspecular effects associated with reflection and transmission of Gaussian sound beams incident upon a plate. Of particular interest in their article is the situation in which multiple Lamb waves are excited simultaneously. The authors found that if one Lamb wave is antisymmetric and the other is symmetric, then the resulting field is the result of superposition of the nonspecular effects from both Lamb waves. However, if both Lamb waves are symmetric or antisymmetric, the Lamb waves interact strongly within the plate.

1.1.4 Nonlinear interaction of sound beams with homogeneous, isotropic solids

A number of studies deal with nonlinear interaction of a liquid-borne sound beam with a homogeneous, isotropic solid. An early study was performed by Van Buren and Brezeale,[60] who investigated theoretically and experimentally the phase shift associated with the reflection of finite-amplitude waves from a plate. Plane waves were considered in the model. Multiple reflections from the plate were considered, but resonance effects were not included in the analysis (the effects of plate thickness on the reflected field were not considered). Ngoc *et al.*[61] predicted the reflection of a sound beam from a plate or half-space, with nonlinearity of the fluid taken into account. They used a nondiffracting model, however. Saito[62] presented an analytic theory of second-harmonic generation produced by a diffracting Gaussian beam normally incident upon a hard plate in a fluid. The author confirmed the theoretical predictions experimentally. He experimentally investigated the diffraction of the finite-amplitude sound beam from an edge.

Nazarov[63] explored theoretically the potential for measuring the nonlinearity of a layer using a plane wave at normal incidence. The idea was to exploit the perfect transmission at the pass-band frequencies of a layer so that, when the fundamental is tuned to a pass band of the layer, the incident plane wave at both the fundamental and second-harmonic frequencies passes completely through the layer. Second-harmonic signal is generated by the finite-amplitude pressure field in the layer at the fundamental frequency and radiated back towards the source. The nonlinearity of the layer can be determined by measuring this second harmonic. We examine this idea in detail in Chap. 2.

Landsberger and Hamilton[64] theoretically and experimentally examined the reflection and transmission of a diffracting sound beam from a thick solid (no multiple reflections). Second-harmonic generation in the fluid and solid was included. A Fourier spectrum decomposition was used to express the sound beam from a plane piston source in terms of plane waves propagating in different directions. The second harmonic generated by a sound beam transmitted through a block of acrylic was measured and matched with numerical predictions that accounted for the cumulative second harmonic generation through both the fluid and solid. Although the second harmonic generated in the fluid was of the same order as the second harmonic generated in the solid, the agreement between the numerical predictions and experimental results was good enough that the two sources of second harmonic could be distinguished, and the parameter of nonlinearity of the solid could be estimated.

Our work in Chap. 4 is essentially an extension of the work by Landsberger and Hamilton, in which we consider plates rather than thick solids. For a plate, the Lamb angles replace the Rayleigh angle as the angles at which nonspecular effects are expected to occur. In general more than one Lamb angle exists for a plate. Also, the Lamb angles depend on the frequency of the incident sound, whereas the Rayleigh angle does not. This frequency dependence means that the transmitted and reflected fields at the second harmonic frequency are different from those at the fundamental frequency. For example, nonspecular effects can occur in the reflection or transmission of the second harmonic component without corresponding effects for the fundamental component.

Throughout this dissertation, reflection from and transmission through interfaces are described by linear theory. Although there is a contribution to harmonic generation due to the finite motion of the interface, this is a local effect that is significant only at distances on the order of one wavelength away from the interface. This local effect has been discussed in detail by Blackstock in relation to finite motion of plane piston sources.[65]

1.2 Scope of this dissertation

This dissertation is both experimental and theoretical in nature. We consider the interaction of sound waves with layers and plates with thicknesses on the order of one wavelength in the material. We develop and evaluate models of such interactions, including effects of nonlinearity. The dissertation is divided into three main sections. First, we consider the irradiation of an isotropic, nonlinear layer by plane waves at normal incidence. Next, the case of a plane wave normally incident upon two linear layers joined at a nonlinear planar interface is examined. Finally, the reflection and transmission of a diffracting sound beam at oblique incidence upon a plate is considered. The theoretical models of these interactions are compared to measurements.

In Chap. 2 we consider the second harmonic and sum frequency generated in an isotropic, homogeneous layer by normally incident plane waves. We first review the linear transmission and reflection of a plane wave from a layer. Next, the second harmonic generated in the plate by a normally incident plane wave, as considered by Nazarov,[63] is reviewed. Sound beams are used to approximate plane waves in the experiments. Difficulties with experimental implementation are discussed. Theory is then developed for the sum-frequency signal generated in the plate by two normally incident plane waves with different frequencies, incident from opposite sides of the plate. An experiment performed using two normally incident sound beams is reported, which is compared with theory for two normally incident plane waves.

In Chap. 3 we develop theory for the interaction of a plane wave at normal incidence upon two layers joined with a compliant, nonlinear boundary. Wave propagation in the plates and in the surrounding fluid is assumed to be linear, and second-harmonic generation is assumed to take place only at the boundary between the plates, because of the contact nonlinearity there. Measurements of reflection and transmission of a sound beam from plates joined with an adhesive bond of varying quality are presented and compared with theory on a qualitative basis. A pair of bonded aluminum plates and a pair of bonded acrylic plates are both used, and results for the fundamental, second, and third harmonic are presented. An impulse response method is also investigated as an alternative means to measure the transmission coefficient for the plate.

In Chap. 4 we examine theoretically and experimentally the reflection and transmission of a diffracting sound beam from a plate. The sound beam is, in general, incident obliquely upon the plate, and distortion of the reflected and transmitted sound beams occurs. An angular spectrum method is used to include diffraction of a beam radiated by a plane piston source. Nonlinear generation of the second harmonic in the fluid is taken into account. Theoretical predictions are compared with measurements at the fundamental and second-harmonic frequencies, over a range of angles of incidence from normal to over 30°.

The results and conclusions are summarized in Chap. 5. In App. A we discuss the experimental apparatus used to make the measurements. Appendix B gives the full solution for the sum-frequency signal radiated from a plate due to two plane waves, normally incident from opposite sides. In App. C we examine the interaction of highly distorted (sawtooth) waves with isotropic, homogeneous plates and two bonded plates.

Chapter 2

NONLINEAR RESPONSE OF AN ISOTROPIC PLATE

In this chapter we investigate the potential for using a resonance method to measure the nonlinear response of a plate. The idea is to exploit the increase in efficiency of harmonic generation when the excitation frequency is near a natural frequency of the sample. In contrast to most implementations of a resonance technique, which are performed using a contact transducer (see, for example, Ref. 1), we immerse our sample in a fluid bath and irradiate it with a sound beam. The advantage of using a sound beam in a fluid bath is that no coupling gel, which may not provide reliable or repeatable coupling, is required. A fluid bath may be practical in industrial applications if a method is devised to easily immerse and then remove the samples.

Previous work discussed in Sec. 1.1.4 motivates this study. Of particular relevance is the investigation by Nazarov,[63] who theoretically explored a method of exploiting resonance effects in a plate to measure its nonlinearity. Also of relevance is the investigation by Landsberger and Hamilton,[64] who demonstrated a method for estimating the coefficient of nonlinearity, which is related to the third-order elastic constants, for a thick isotropic solid immersed in a fluid bath.

In this chapter we develop models that describe the nonlinear generation of new frequency components in an isotropic, lossless plate due to normally incident plane waves. We begin by reviewing the analysis of Nazarov and discussing problems with the experimental implementation of this technique. Then an alternative configuration is considered, in which two plane waves of different frequencies are incident upon the plate from opposite sides. The latter model is compared with measurements we made on an aluminum plate immersed in water. Aluminum was chosen because the ratio of specific acoustic impedances of aluminum to water is large enough to cause significant resonance effects, yet small enough that a steady state is reached fairly quickly in the plate.

We examine plane waves at normal incidence to the plate. One reason for doing so is to keep the analysis as simple as possible, so that the feasiblility of measuring the nonlinearity of a plate in an immersion test may be determined more easily. By considering plane waves at normal incidence, complications associated with the excitation of shear waves in the plate are avoided. For the experiments, plane waves are approximated by sound beams.

2.1 Review of theory for reflection and transmission

In order to predict the harmonic generation in a plate due to a normally-incident plane wave, we first require expressions for the linear response of the plate to the wave. Here we obtain the linear solution for the reflection and transmission of a plane wave with angular frequency ω normally incident upon the plate.

The solution for the reflection and transmission of a plane wave incident on a fluid layer is given elsewhere (see, for example, Sec. 4E of Ref. 66). The configuration is shown in Fig. 2.1. A plane wave with pressure amplitude P_i incident upon the plate from $x < 0$ gives rise to a reflected wave with amplitude P_r, a transmitted wave with amplitude P_t, and waves in the layer with amplitudes A and B, propagating in the positive and negative directions, respectively. The acoustic pressure p is

$$p = \frac{1}{2} \begin{cases} P_i e^{j(\omega t - k_f x)} + P_r e^{j(\omega t + k_f x)} + \text{c.c.}\,, & x < 0\,, \\ A e^{j(\omega t - k_s x)} + B e^{j(\omega t + k_s x)} + \text{c.c.}\,, & 0 \le x \le l\,, \\ P_t e^{j[\omega t - k_f (x - l)]} + \text{c.c.}\,, & x > l\,, \end{cases} \tag{2.1}$$

where $k_{f,s} = \omega / c_{f,s}$, and c_f and c_s are the small-signal sound speeds in the surrounding fluid and the layer, respectively.

The layer in Fig. 2.1 is taken to be an elastic plate. When discussing waves in solids, it is conventional to write equations in terms of stress σ rather than pressure. However, we consider plates immersed in liquid, and because we consider only normally incident plane waves, the waves in both the liquid and the

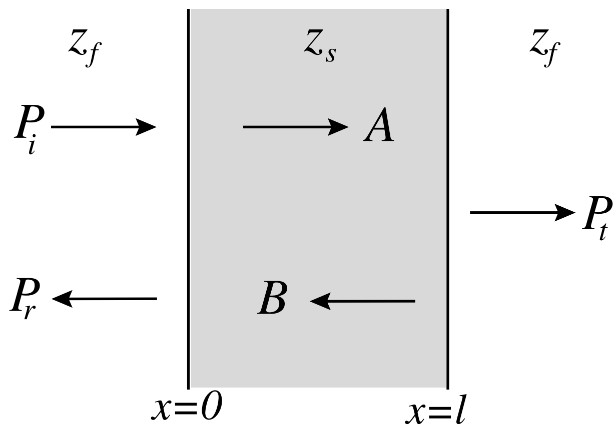

Figure 2.1: Interaction with plate of plane wave with amplitude P_i incident from the left.

solid plate are longitudinal. It is therefore convenient here to use the same wave variables for both the liquid and the solid. We choose sound pressure rather than stress, which are related by

$$\sigma = -p\,. \tag{2.2}$$

Likewise, we also use particle velocity $u = \partial\xi/\partial t$ rather than strain $\partial\xi/\partial x$, where ξ is the particle displacement in the medium.

The particle velocity u is determined by applying to Eqn. (2.1) the linearized equation of momentum conservation in one dimension,

$$\frac{\partial p}{\partial x} = -\rho_0 \frac{\partial u}{\partial t}\,, \tag{2.3}$$

where ρ_0 is the unperturbed density of the medium. Doing so gives

$$u = \frac{1}{2}\begin{cases} \left(P_i e^{j(\omega t - k_f x)} - P_r e^{j(\omega t + k_f x)}\right)/z_f + \text{c.c.}\,, & x < 0\,, \\ \left(A e^{j(\omega t - k_s x)} - B e^{j(\omega t + k_s x)}\right)/z_s + \text{c.c.}\,, & 0 \le x \le l\,, \\ \left(P_t e^{j[\omega t - k_f (x-l)]}\right)/z_f + \text{c.c.}\,, & x > l\,, \end{cases} \tag{2.4}$$

where $z_f = \rho_f c_f$ and $z_s = \rho_s c_s$ are the specific acoustic impedances of the surrounding fluid and the solid plate, respectively, and ρ_f and ρ_s are the corresponding unperturbed densities. The expressions for the transmission and reflection coefficients are determined by imposing continuity of pressure and particle velocity across the interfaces at $x = 0$ and $x = l$, and solving the resulting system of equations for P_r/P_i and P_t/P_i. The transmission coefficient is

$$W \equiv \frac{P_t}{P_i} = \frac{1}{\cos k_s l + \frac{j}{2}\left(\frac{z_f}{z_s} + \frac{z_s}{z_f}\right)\sin k_s l}\,, \tag{2.5}$$

and the reflection coefficient is

$$V \equiv \frac{P_r}{P_i} = \frac{j\left(\frac{z_s}{z_f} - \frac{z_f}{z_s}\right)\sin k_s l}{2\cos k_s l + j\left(\frac{z_f}{z_s} + \frac{z_s}{z_f}\right)\sin k_s l}\,. \tag{2.6}$$

In Fig. 2.2 the transmission and reflection coefficients are plotted as a function of frequency for an aluminum plate. Parameters for aluminum and water are given in Table A.1. Perfect transmission is achieved for frequencies at which

$$\lambda_n = 2l/n\,, \tag{2.7}$$

where λ_n is the wavelength in the plate and n is an integer. Pass-band frequencies f_n^{pass} are thus given by

$$f_n^{\text{pass}} = \frac{nc_s}{2l}\,. \tag{2.8}$$

In Fig. 2.2, $f_n \approx 1, 2, 3, \ldots$ MHz. At frequencies $f = f_n^{\text{pass}}$ the reflection coefficient vanishes. However, the reflection minimum is very sharp, and the reflection coefficient grows rapidly as the frequency deviates from the pass-band frequency. The transmission coefficient reaches a minimum of approximately $-j2z_f/z_s$ for

$$\lambda_n^{\text{stop}} = 4l/(2n-1)\,, \tag{2.9}$$

where the superscript "stop" is included to distinguish these wavelengths from the pass-band wavelengths of Eqn. (2.7). In Fig. 2.2 the transmission minima are at frequencies $f_n^{\text{stop}} \approx 0.5, 1.5, 2.5, \ldots$ MHz. For an aluminum plate in water

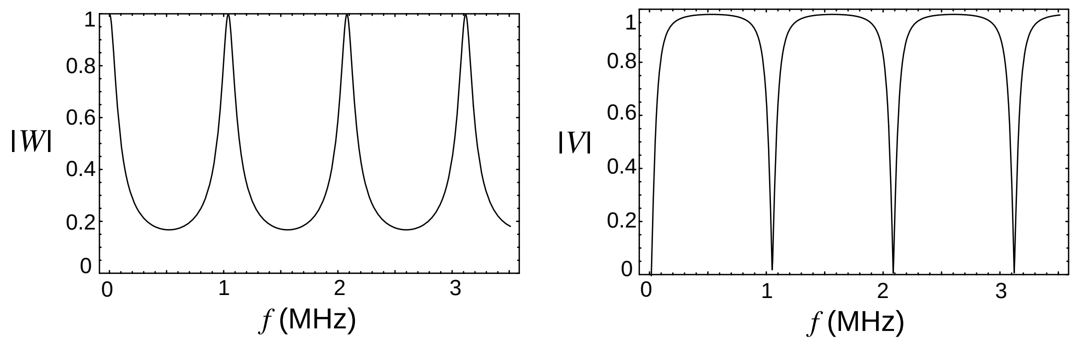

Figure 2.2: Transmission and reflection coefficients for an aluminum plate in water. Material paramters for the plate are given in Table A.1.

$z_s/z_f \approx 12$, so the minumum value of the transmission coefficient is approximately 0.17. These transmission minima correspond to reflection maxima,

$$V_{\max} = \frac{1 - z_f^2/z_s^2}{1 + z_f^2/z_s^2}\,, \quad f = f_n^{\text{stop}}\,, \tag{2.10}$$

which for the aluminum plate in water is 0.986.

Now consider an incident plane wave that is composed of several components with frequencies that are harmonics (integer multiples) of the fundamental frequency. For example, a finite-amplitude plane wave generates harmonic components as it propagates. Equation (2.10) indicates that if the fundamental frequency is tuned to a pass-band frequency, harmonics of the signal at pass-band frequencies are also passed. Thus, in addition to the component of the signal at the fundamental frequency, all harmonic components are also transmitted completely through the plate.

2.2 Theory for second-harmonic generation

In this section we explore the possibility of measuring the parameter of nonlinearity of a plate by using a time-harmonic excitation from a normally-incident plane wave, and exploiting resonance in the plate. As mentioned in the preface to this chapter, this possibility was first explored by Nazarov.[63] Nazarov's analysis is reviewed here in our context, and in Sec. 2.3 it is extended to the case of two plane waves of different frequencies incident from opposite directions.

The scheme considered here is illustrated in Fig. 2.3. A time-harmonic plane wave $p_f^{(1)}$ generated by the sound source in the fluid (f) is normally incident upon a plate. As $p_f^{(1)}$ propagates through the fluid, it generates a second harmonic component $p_f^{(2)}$. The standing waves in the plate at the fundamental frequency excited by the incident wave cause the solid (s) to radiate a second harmonic component $p_s^{(2)}$ back towards the source. In general, both $p_f^{(1)}$ and $p_f^{(2)}$ are reflected from the plate. However, as pointed out in Sec. 2.1, when $p_f^{(1)}$ is tuned to a pass-band frequency, the second harmonic generated in the fluid $p_f^{(2)}$ is also at a pass-band frequency, and it is transmitted through the plate. Thus, when $p_f^{(1)}$ is at a pass-band frequency, only $p_s^{(2)}$ propagates back towards the source. Moreover, at these pass-band frequencies resonance causes amplification in the plate. It is reasonable to expect the nonlinear generation of $p_s^{(2)}$ to be enhanced by the amplification.

Throughout this section, reflection from and transmission through interfaces are described by linear theory. As discussed in Sec. 1.1.4, contribution to second harmonic generation by finite motion of the interface is a local effect that is significant only at distances on the order of one wavelength away from the interface.

2.2.1 Primary field in the plate

The second harmonic is generated in the plate by the internal wave field at the fundamental frequency. In Sec. 2.1 equations were developed that describe the reflection and transmission of a plane wave at normal incidence to a plate. Solving Eqns. (2.1) and (2.4) for A and B also allows us to solve for the field in the plate. The amplitudes A and B are

$$A = \frac{\left(1 + \frac{z_s}{z_f}\right) e^{jk_s l} P_i}{2\cos k_s l + j(\frac{z_f}{z_s} + \frac{z_s}{z_f}) \sin k_s l}\,, \tag{2.11}$$

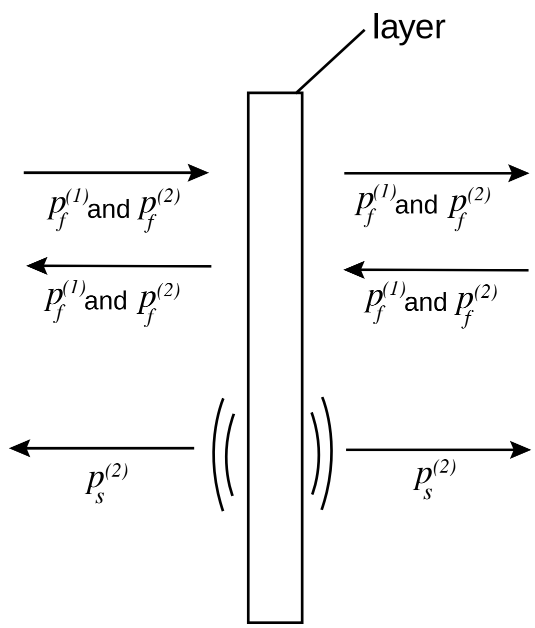

Figure 2.3: Geometry for second-harmonic generation in the plate. Waves $p_f^{(1)}$ and $p_f^{(2)}$ are not reflected at pass band frequencies, and thus only $p_s^{(2)}$ propagates towards the source.

$$B = \frac{\left(1 - \frac{z_s}{z_f}\right) e^{-jk_s l} P_i}{2\cos k_s l + j(\frac{z_f}{z_s} + \frac{z_s}{z_f}) \sin k_s l} \,. \tag{2.12}$$

The amplitude in the plate, which we denote P_{pl}, is

$$P_{\text{pl}} = Ae^{-jk_s x} + Be^{jk_s x} = P_i \left[\frac{\cos k_s(l-x) + j\frac{z_s}{z_f} \sin k_s(l-x)}{\cos k_s l + \frac{j}{2}\left(\frac{z_f}{z_s} + \frac{z_s}{z_f}\right) \sin k_s l} \right] . \tag{2.13}$$

The magnitude and phase of Eqn. (2.13) are shown in Fig. 2.4 for an aluminum plate. The frequency for which $\lambda_1^{\text{stop}} = 4l$ corresponds to the first transmission minimum in Fig. 2.2. Since the reflection coefficient is approximately unity at that frequency, there is pressure (stress) doubling at $x = 0$. The first transmission maximum is at $\lambda_1^{\text{pass}} = 2l$. The maximum amplitude P_{max}, given by

$$P_{\text{max}} = \frac{z_s}{z_f} |P_i| \tag{2.14}$$

is at $x = l/2$. For aluminum, Eqn. (2.14) gives a pressure amplification of approximately 12. At $\lambda_2^{\text{stop}} = 4l/3$ we have the second transmission minimum. The maximum pressure amplification in the plate is a factor of 2 at $x = 0$ and $x = 2/3$. The second transmission maximum is at $\lambda_2^{\text{pass}} = l$, and $|P_{\text{pl}}| = P_{\text{max}}$ at $x = l/4$ and $x = 3l/4$.

From Eqn. (2.13) and Fig. 2.4 we see that the amplification in the plate is greatest near pass-band frequencies, for which $\lambda_n^{\text{pass}} = 2l/n$. It is thus reasonable to expect that the most efficient second harmonic generation occurs at those frequencies. From Eqn. (2.14) we see that the amplification in the plate at the pass bands is proportional to z_s/z_f, so it is reasonable to expect that the second harmonic generated in the plate will be stronger as the ratio of the impedance of the plate to the impedance of the fluid increases.*

*Because, for a thick solid, increasing z_s/z_f decreases the amount of wave energy transmitted into the solid, it may be counterintuitive that the amplification factor in the plate increases as z_s/z_f increases. However, this amplification occurs only for a sinusoidal incident wave at steady state. The number of cycles of the incident wave required to reach a steady state, and to achieve amplification, increases as z_s/z_f increases.

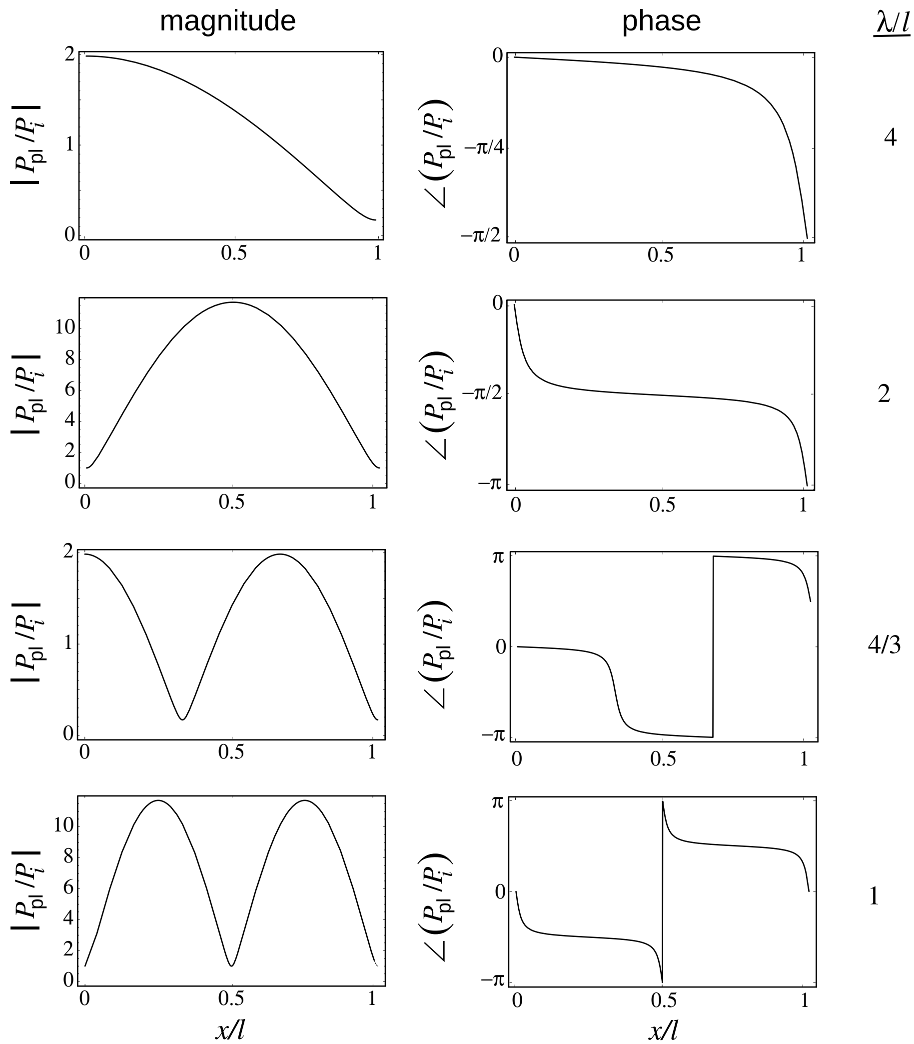

Figure 2.4: Wave amplitude in plate due to plane wave incident from $x < 0$. Stop bands are at $\lambda_n^{\text{stop}} = 4l, 4l/3$. Pass bands are at $\lambda_n^{\text{pass}} = 2l, l$.

2.2.2 Second-harmonic radiation from the plate

In this section we model the second-harmonic component generated within the plate due to finite-amplitude effects there. The nonlinear equation we use to model finite-amplitude, longitudinal waves in one dimension is (see, for example, Ref. 67)

$$\left(\frac{\partial^2}{\partial x^2} - \frac{1}{c_s^2}\frac{\partial^2}{\partial t^2}\right)p = -\frac{\beta_s}{\rho_s c_s^4}\frac{\partial^2 p^2}{\partial t^2} - \left(\frac{\partial^2}{\partial x^2} + \frac{1}{c_s^2}\frac{\partial^2}{\partial t^2}\right)\mathcal{L}\,, \tag{2.15}$$

where $\mathcal{L} = \frac{1}{2}(\rho_s u^2 - p^2/\rho_s c_s^2)$ is a Lagrangian density, u is the particle velocity, and β_s is the coefficient of nonlinearity. For a solid

$$\beta_s = -\left(\frac{3}{2} + \frac{\mathcal{A} + 3\mathcal{B} + \mathcal{C}}{\rho_s c_s^2}\right)\,, \tag{2.16}$$

where $\mathcal{A}$, $\mathcal{B}$, and $\mathcal{C}$ are Landau's third-order elastic constants, and $\rho_s c_s^2 = K + \frac{4}{3}\mu$, where K is the bulk modulus and μ is the shear modulus.[34] For liquids, the analogous coefficient β_f is usually expressed as

$$\beta_f = 1 + B/2A\,, \tag{2.17}$$

where B/A is referred to as the parameter of nonlinearity.[68*]

Equation 2.15 is valid for a lossless fluid. However, as discussed in Sec. 2.1 for this analysis we consider plane waves at normal incidence to the plate, so no shear waves are excited. Hence the plate may be treated as a fluid layer.

The method of successive approximations is used to solve Eqn. (2.15). We introduce $p = p^{(1)} + p^{(2)}$ and $u = u^{(1)} + u^{(2)}$, where $|p^{(1)}| \gg |p^{(2)}|$ and $|u^{(1)}| \gg |u^{(2)}|$, and define amplitudes $P^{(n)}$ and $U^{(n)}$ such that

$$p^{(n)} = \frac{1}{2}P^{(n)}e^{jn\omega t} + \text{c.c.}\,,\;\; n = 1, 2, \tag{2.18}$$

$$u^{(n)} = \frac{1}{2}U^{(n)}e^{jn\omega t} + \text{c.c.}\,,\;\; n = 1, 2. \tag{2.19}$$

---

*In Eqn. (2.17), A and B are related to the Taylor series expansion of the equation of state for the fluid, and are not to be confused with the wave amplitudes in the solid A and B used everywhere else in this chapter.

Although the squares of $p^{(1)}$ and $u^{(1)}$ contain dc terms as well as terms at 2ω, only terms describing second-harmonic signals are of interest. Substituting Eqns. (2.18) and (2.19) into Eqn. (2.15) gives, at second order,

$$\left(\frac{d^2}{dx^2}+4k_s^2\right)P^{(2)}=\frac{2k_s^2\beta_s}{\rho_s c_s^2}(P^{(1)})^2-\frac{1}{4}\left(\frac{d^2}{dx^2}-4k_s^2\right)\left(\rho_s(U^{(1)})^2-\frac{(P^{(1)})^2}{\rho_s c_s^2}\right). \quad (2.20)$$

Using Eqns. (2.1) and (2.4) along with Eqns. (2.18) and (2.19), we express $(P^{(1)})^2$ and $(U^{(1)})^2$ as [recall Eqn. (2.1)]

$$(P^{(1)})^2 = A^2e^{-j2k_sx}+B^2e^{j2k_sx}+2AB\,, \quad (2.21)$$

$$(U^{(1)})^2 = \frac{1}{z_s^2}\left(A^2e^{-j2k_sx}+B^2e^{j2k_sx}-2AB\right). \quad (2.22)$$

The first and second terms in both Eqns. (2.21) and (2.22) represent waves propagating in the positive and negative directions, respectively. The third terms represent a pulsation of the plate, with no spatial dependence.

Substituting Eqns. (2.21) and (2.22) into Eqn. (2.20) gives

$$\left(\frac{d^2}{dx^2}+4k_s^2\right)P^{(2)} = \frac{2k_s^2\beta_s}{\rho_s c_s^2}\left[A^2e^{-j2k_sx}+B^2e^{j2k_sx}+2AB\left(1-\frac{1}{\beta_s}\right)\right]. \quad (2.23)$$

Equation (2.23) has the same form as the equation of motion of a forced simple harmonic oscillator (with x in place of t). The solution for $P^{(2)}$ is

$$P^{(2)} = (H_1+S_1x)\,e^{-j2k_sx}+(H_2+S_2x)\,e^{j2k_sx}+S_3\,, \quad 0\le x\le l\,, \quad (2.24)$$

where H_1 and H_2 are amplitudes in the homogeneous solution and

$$S_1x = j2k_sx\frac{\beta_sA^2}{4\rho_sc_s^2}\,, \quad S_2x=-j2k_sx\frac{\beta_sB^2}{4\rho_sc_s^2}\,, \quad S_3=\frac{AB}{\rho_sc_s^2}(\beta_s-1)\,, \quad (2.25)$$

are amplitudes in the particular solution. In addition, waves are radiated from the plate to the left and right with pressure amplitudes $P^{2\omega}_{\text{left}}$ and $P^{2\omega}_{\text{right}}$. The total expression for $P^{(2)}$ is

$$P^{(2)} = \begin{cases} P^{2\omega}_{\text{left}}e^{j2k_fx}\,, & x<0\,, \\ (H_1+S_1x)\,e^{-j2k_sx}+(H_2+S_2x)\,e^{j2k_sx}+S_3\,, & 0\le x\le l\,, \\ P^{2\omega}_{\text{right}}e^{j2k_f(x-l)}\,, & x>l\,. \end{cases} \quad (2.26)$$

The second-order particle velocity in the plate, $U^{(2)}$, is determined by applying the linearized momentum equation, Eqn. (2.3), to Eqn. (2.26).* Doing so yields

$$U^{(2)} = \begin{cases} -P_{\text{left}}^{2\omega} e^{j2k_f x}/z_f \,, & x < 0 \,, \\ \Big[(H_1 + S_1 x)\, e^{-j2k_s x} - (H_2 + S_2 x)\, e^{j2k_s x} \Big] / z_s \,, & 0 \le x \le l \,, \\ P_{\text{right}}^{2\omega} e^{j2k_f (x-l)}/z_f, & x > l \,. \end{cases} \tag{2.27}$$

Pressure and particle velocity are matched across interfaces at $x = 0$ and $x = l$. The four resulting equations are solved for $H_1, H_2, P_{\text{left}}^{2\omega}$, and $P_{\text{right}}^{2\omega}$. The expressions for $P_{\text{left}}^{2\omega}$ and $P_{\text{right}}^{2\omega}$, the only ones needed for the field outside the plate, are

$$P_{\text{left}}^{2\omega} = \frac{\Big(\frac{z_f}{z_s} - 1\Big) S_1 l e^{-j2k_s l} - \Big(1 + \frac{z_f}{z_s}\Big) S_2 l e^{j2k_s l} + \Big(j \frac{z_f}{z_s} \sin 2k_s l + \cos 2k_s l - 1\Big) S_3}{2\cos 2k_s l + j\left(\frac{z_f}{z_s} + \frac{z_s}{z_f}\right) \sin 2k_s l}, \tag{2.28}$$

$$P_{\text{right}}^{2\omega} = \frac{\Big(1 + \frac{z_f}{z_s}\Big) S_1 l + \Big(1 - \frac{z_f}{z_s}\Big) S_2 l + \Big(j \frac{z_f}{z_s} \sin 2k_s l + \cos 2k_s l - 1\Big) S_3}{2\cos 2k_s l + j\left(\frac{z_f}{z_s} + \frac{z_s}{z_f}\right) \sin 2k_s l} \,. \tag{2.29}$$

We are particularly interested in the second harmonic generated near the pass-band frequencies. At the first pass-band frequency, for which $\lambda_1 = 2l$, Eqns. (2.28) and (2.29) reduce to

$$P_{\text{left}}^{2\omega} = -j \frac{\pi \beta_s P_i^2}{8 \rho_s c_s^2} \left(\frac{z_s}{z_f} - \frac{z_f}{z_s} \right) , \tag{2.30}$$

$$P_{\text{right}}^{2\omega} = j \frac{\pi \beta_s P_i^2}{8 \rho_s c_s^2} \left(3\frac{z_s}{z_f} + \frac{z_f}{z_s} \right) . \tag{2.31}$$

Note also that the term $\Big(j \frac{z_f}{z_s} \sin 2k_s l + \cos 2k_s l - 1\Big) S_3$ in Eqns. (2.28) and (2.29) vanishes at pass-band frequencies. This suggests that the second harmonic generated by the spatially independent vibration of the plate [the third terms in Eqns. (2.21) and (2.22)] does not contribute significantly to the radiated second harmonic near frequencies of interest to us.

*Small-signal acoustic relations may be applied to second-order quantities, because the resulting errors are at third order or higher.

Equation (2.28) is plotted as a function of frequency in Fig. 2.5 for an aluminum plate in water. Parameters for aluminum and water are given in Table A.1. The most significant second harmonic radiation occurs at the pass-band frequencies at approximately $1, 2, 3, \ldots$ MHz, for which $\lambda_n^{\text{pass}} = nl/2$. The magnitude of the second harmonic generated in the plate near the pass bands increases with frequency because S_1 and S_2 in Eqn. (2.28) are proportional to k_s. For the frequencies of interest (low MHz), the second harmonic generated is on the order of $\sim 10^{-9} P_i^2$ Pa (where P_i is in Pa). For a source pressure on the order of 1 MPa this corresponds to a radiated second harmonic on the order of ~ 1 kPa.

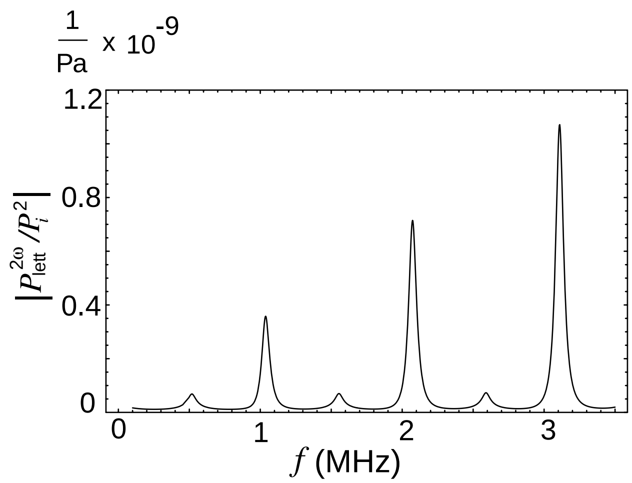

Figure 2.5: Predicted second harmonic radiated to the left from plate vs. source frequency. Maxima correspond to pass-band frequencies in the plate.

In Fig. 2.6 we compare an approximate expression for the radiation of second harmonic to the right with the full expression, Eqn. (2.29). The approximate expression is given by setting $S_3 = 0$ in Eqn. (2.29). Doing so is equivalent to ignoring the spatially invariant terms in Eqns. (2.21) and (2.22). The difference in magnitudes between the full and approximate expressions is almost imperceptible, except near the frequencies of minimum transmission (stop bands), 1.5 and 2.5 MHz. The phases are compared near the first pass band (indicated

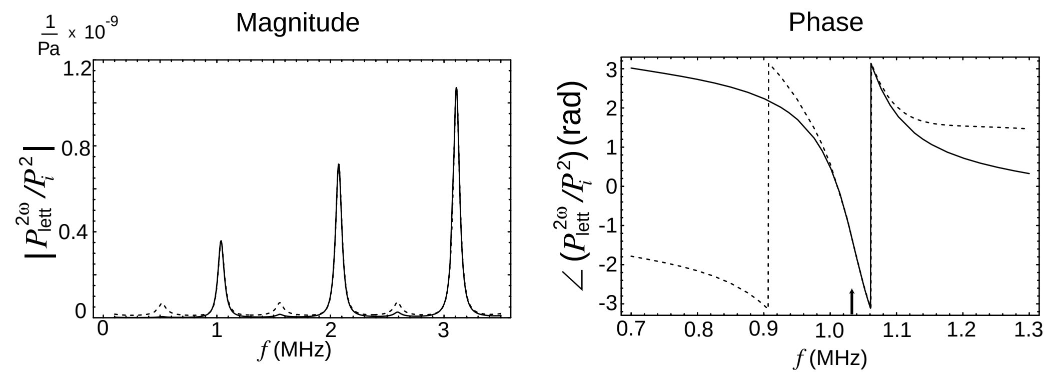

Figure 2.6: Comparison of magnitude and phase between exact (- - -) and approximate (——) expressions for the second harmonic radiated into the fluid to the left. Phases are compared near the first pass-band frequency, indicated by the arrow.

by the arrow). The comparison of the phases also shows very good agreement near the pass-band frequency, but there are significant differences between the solutions away from the pass-band frequency. The same is true for comparisons near higher pass-band frequencies. However, because second harmonic generation occurs mostly near the pass-band frequencies, and we do not expect to perform measurements away from there, it is a reasonable approximation for practical purposes to set $S_3 = 0$. Although this approximation does not simplify Eqns. (2.29) and (2.28) significantly, an analogous approximation of the expressions for the sum-frequency radiation which is developed in Sec. 2.3, simplifies the expressions there considerably.

2.2.3 Experiment

An experiment corresponding to the theory developed in Secs. 2.1 and 2.2 was attempted. A sound beam generated by a plane, circular, piston transducer irradiated an aluminum plate at normal incidence. A PVDF membrane hydrophone was placed between the source and the plate. (Properties of the sources, hydrophone, and plate are given in App. A.) The frequency of the incident sound beam was chosen to correspond to either f_1^{pass} near 1 MHz or f_2^{pass} near 2 MHz.

Substantial difficulties were encountered. While diffraction effects are not taken into account in the analysis, a real sound beam generated by a plane piston source of radius a has a directivity given by (see, for example, Sec. 13B of Ref. 66)

$$D(\theta) = \frac{2J_1(ka\sin\theta)}{ka\sin\theta}, \tag{2.32}$$

where θ is the angular deviation from the beam axis. In the farfield of a 1-MHz, 1-in.-diameter source in water, for example, the pressure drops by 3 dB approximately 2 degrees from the axis. The transmission and reflection coefficients for a plate depend on the angle of incidence as well as the frequency, so the reflection coefficient for components of the sound beam at the fundamental and second harmonic frequencies that are not perfectly normal to the plate is in general not zero, even at pass-band frequencies. The reflected signals at the second harmonic are very difficult (if not impossible) to distinguish from the second harmonic radiated from the plate.

Figure 2.7 illustrates the problem. Although diffraction is discussed in detail in Chap. 5, for purposes of discussion here we show the angular spectrum associated with a 1-MHz, 1-in.-diameter plane piston source. (Directivity, which is proportional to angular spectrum at large distances from the source,[69] is shown.) This angular spectrum is the distribution of pressure in the sound beam with propagation angle. The magnitude of the plane-wave reflection coefficient, $|V|$, for an aluminum plate in water at the first pass band, $f_1 = 1.04$ MHz (dashed line), is superimposed on the angular spectrum. As the angle of incidence deviates from normal, the reflection coefficient rapidly increases from zero. However, the sound beam contains significant energy that propagates within a few degrees from normal incidence. For this reason, even if the sound beam is tuned to a pass band and is normally incident upon the plate, significant reflection of the sound beam at the fundamental and second-harmonic frequencies can occur.

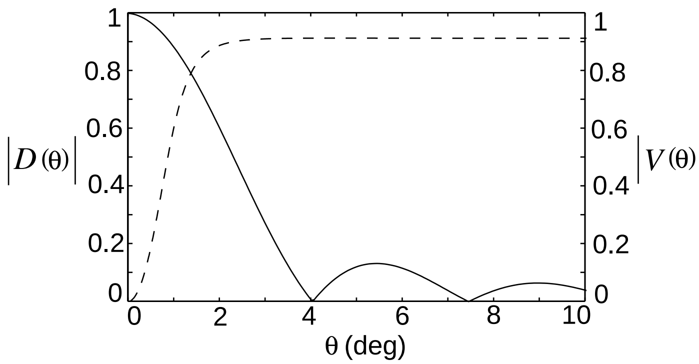

Figure 2.7: Angular spectrum $|D(\theta)|$ (—) for a 1 in. plane piston source compared with magnitude of the reflection coefficient $|V(\theta)|$ (- -) at the pass-band frequency $f_1 = 1.04$ MHz.

For a real sound beam, Fig. 2.7 shows that some wave reflection is unavoidable, even at pass-band frequencies. In Sec. 2.3 we propose an alternative experimental arrangement to measure the nonlinearity of a plate. In this arrangement the plate is irradiated from both sides by sound beams with different primary frequencies. We measure the sum-frequency component, rather than the second harmonic, at the receiver. While second harmonic is generated by the incident and reflected primary field in the fluid as well as in the plate, the sum-frequency component that is measured by the receiver is generated only in the plate and by the interaction of the primary sound beams in the fluid between the plate and the receiver. (Sum-frequency components can be generated elsewhere, but those interactions either are precluded by use of tone bursts or do not propagate to the hydrophone). Moreover, by positioning the receiver close to the plate we can minimize the sum-frequency component generated in the fluid.

2.3 Theory for sum-frequency generation

Here we consider an alternative configuration to measure β_s for an immersed plate. We irradiate the plate with two plane waves, each with a different frequency, and measure the sum-frequency pressure at the receiver. This is done to make it easier to distinguish the signal generated by nonlinear interaction of the waves in the plate from signals generated by nonlinear interaction of waves in the fluid.

Figure 2.8 illustrates the configuration. Two plane waves with frequencies f_1 and f_2 are incident upon the plate from opposite sides. The amplitudes of the incident plane waves are designated P_{1i} for the wave from the left, as in Sec. 2.1, and P_{2i} for the wave from the right. The wave incident from the left gives rise to waves in the plate with amplitudes A_1 and B_1, and the wave incident from the right gives rise to waves in the plate with amplitudes A_2 and B_2. The interaction of the four waves in the plate generates signals at $2f_1$, $2f_2, f_+ = f_1 + f_2$, and $f_- = f_1 - f_2$, which are radiated into the fluid. In the following analysis we consider the waves radiated into the fluid at the sum frequency f_+ to the left and right with amplitudes P^+_{left} and P^+_{right}, respectively.

The method used to solve for P^+_{left} and P^+_{right} is essentially the same as that used to solve for $P^{2\omega}_{\text{left}}$ and $P^{2\omega}_{\text{right}}$ in Sec. 2.2. First the sum-frequency signal generated due to nonlinear wave interaction in the plate is determined. Then the amplitudes P^+_{left} and P^+_{right} are determined by equating pressure and particle velocity across the fluid/plate boundaries.

2.3.1 Primary wave field in the plate

The total first-order pressure is $p^{(1)} = p_1 + p_2$, where

$$p_1 = \frac{1}{2}\begin{cases} P_{1i}e^{j(\omega_1 t - k_{f1}x)} + P_r e^{j(\omega_1 t + k_{f1}x)} + \text{c.c.}\,, & x < 0\,, \\ A_1 e^{j(\omega_1 t - k_1 x)} + B_1 e^{j(\omega_1 t + k_1 x)} + \text{c.c.}\,, & 0 \le x \le l\,, \\ P_{1t}e^{j[\omega_1 t - k_{f1}(x-l)]} + \text{c.c.}\,, & x > l\,, \end{cases} \tag{2.33}$$

$$p_2 = \frac{1}{2}\begin{cases} P_{2t}e^{j(\omega_2 t + k_{f2}x)} + \text{c.c.}\,, & x < 0\,, \\ A_2 e^{j(\omega_2 t - k_2 x)} + B_2 e^{j(\omega_2 t + k_2 x)} + \text{c.c.}\,, & 0 \le x \le l\,, \\ P_{2i}e^{j[\omega_2 t - k_{f2}(x-l)]} + P_{2r}e^{j[\omega_2 t + k^f_2(x-l)]} + \text{c.c.}\,, & x > l\,, \end{cases} \tag{2.34}$$

where $k_{1,2} = \omega_{1,2}/c_s$ and $k_{f1,f2} = \omega_{1,2}/c_f$. Equation (2.34) has the same form as Eqn. (2.1). The pressure p_2 is illustrated in Fig. 2.9. The amplitudes A_2 and B_2

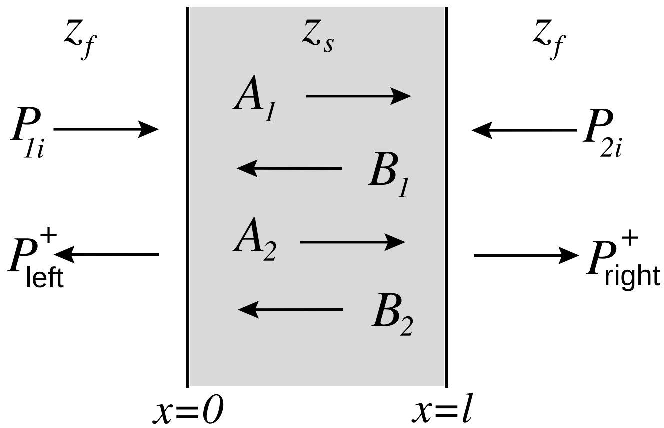

Figure 2.8: Geometry for analyzing sum-frequency generation. Incident plane waves with amplitudes P_{1i} and P_{2i} give rise to A_1, B_1, A_2, and B_2, which interact in the plate and radiate waves with amplitude P^+_{left} and P^+_{right} into the fluid.

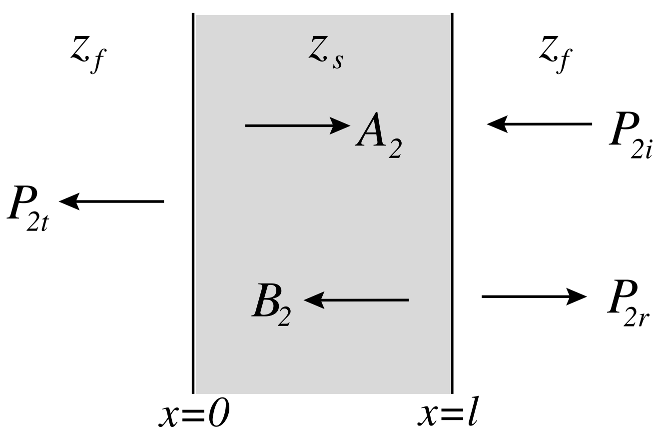

Figure 2.9: Irradiation of plate of thickness l by plane wave of amplitude P_{2i} from right.

are

$$\frac{A_2}{P_{2i}} = \frac{1 - \frac{z_s}{z_f}}{2\cos k_2 l + j(\frac{z_f}{z_s} + \frac{z_s}{z_f})\sin k_2 l}\,, \tag{2.35}$$

$$\frac{B_2}{P_{2i}} = \frac{1 + \frac{z_s}{z_f}}{2\cos k_2 l + j(\frac{z_f}{z_s} + \frac{z_s}{z_f})\sin k_2 l}\,. \tag{2.36}$$

The wave amplitude in the plate due to P_{2i} is

$$P_{\text{pl2}} = A_2 e^{-jk_2 x} + B_2 e^{jk_2 x}\,. \tag{2.37}$$

Substituting Eqns. (2.35) and (2.36) into Eqn. (2.37) yields

$$\frac{P_{\text{pl2}}}{P_{2i}} = \frac{\cos k_2 x + j\frac{z_s}{z_f}\sin k_2 x}{\cos k_2 l + \frac{j}{2}\left(\frac{z_f}{z_s} + \frac{z_s}{z_f}\right)\sin k_2 l}\,. \tag{2.38}$$

According to Eqn. (2.38), the amplitude in the plate due to a plane wave incident from the right is the mirror-image of the amplitude in the plate due to a plane wave incident from the left (shown in Fig. 2.4).

2.3.2 Sum-frequency signal radiated from plate

The first-order pressure and particle velocity in the plate are expressed as the sum of four plane waves in the plate,

$$\begin{aligned} p^{(1)} &= \frac{1}{2}\Big(A_1 e^{j(\omega_1 t - k_1 x)} + B_1 e^{j(\omega_1 t + k_1 x)} \\ &\quad + A_2 e^{j(\omega_2 t - k_2 x)} + B_2 e^{j(\omega_2 t + k_2 x)}\Big) + \text{c.c.}\,, \end{aligned} \tag{2.39}$$

$$\begin{aligned} u^{(1)} &= \frac{1}{2z_s}\Big(A_1 e^{j(\omega_1 t - k_1 x)} - B_1 e^{j(\omega_1 t + k_1 x)} \\ &\quad + A_2 e^{j(\omega_2 t - k_2 x)} - B_2 e^{j(\omega_2 t + k_2 x)}\Big) + \text{c.c.}\,, \end{aligned} \tag{2.40}$$

where the amplitudes A_1, B_1, A_2, and B_2 are the same as those determined in Secs. 2.2.1 and 2.3.1. We use the one-dimensional second-order wave equation, Eqn. (2.15), in the quasilinear approximation to predict the pressure generated at the sum frequency. Because only terms that are time-harmonic with angular frequency $\omega_+ = \omega_1 + \omega_2$ are considered, we assume pressures and velocities of the form

$$(p^{(1)})^2 = \frac{1}{4}(P^{(1)})^2 e^{j\omega_+ t} + \text{c.c.}\,, \quad p^+ = \frac{1}{2}P^+ e^{j\omega_+ t} + \text{c.c.}\,, \tag{2.41}$$

$$(u^{(1)})^2 = \frac{1}{4}(U^{(1)})^2 e^{j\omega_+ t} + \text{c.c.}\,, \quad u^+ = \frac{1}{2}U^+ e^{j\omega_+ t} + \text{c.c.}\,, \tag{2.42}$$

where $k_+ = \omega_+/c_s$. Equations (2.41) and (2.42) are substituted into Eqn. (2.15) to give

$$\left(\frac{d^2}{dx^2} + k_+^2\right)P^+ = \frac{\beta_s k_+^2}{2\rho_s c_s^2}(P^{(1)})^2 - \frac{1}{4}\left(\frac{d^2}{dx^2} - k_+^2\right)\left(\rho_s (U^{(1)})^2 - \frac{(P^{(1)})^2}{\rho_s c_s^2}\right)\,. \tag{2.43}$$

Squaring Eqns. (2.39) and (2.40) and retaining only sum-frequency terms gives

$$(P^{(1)})^2 = 2\Big(A_1 A_2 e^{-jk_+ x} + A_1 B_2 e^{-jk_- x} + B_1 A_2 e^{jk_- x} + B_1 B_2 e^{jk_+ x}\Big)\,, \tag{2.44}$$

$$(U^{(1)})^2 = \frac{2}{z_s^2}\left(A_1 A_2 e^{-jk_+ x} - A_1 B_2 e^{-jk_- x} - B_1 A_2 e^{jk_- x} + B_1 B_2 e^{jk_+ x}\right)\,, \tag{2.45}$$

where $k_- = (\omega_1 - \omega_2)/c_s$. We solve the second-order inhomogeneous ordinary differential equation of the form

$$\begin{aligned}\left(\frac{d^2}{dx^2} + k_+^2\right)P^+ = {} & \frac{\beta_s k_+^2}{\rho_s c_s^2}\left(A_1 A_2 e^{-jk_+ x} + B_1 B_2 e^{jk_+ x}\right) \\ & + \frac{(\beta_s - 1)k_+^2 - k_-^2}{\rho_s c_s^2}\left(A_1 B_2 e^{-jk_- x} - A_2 B_1 e^{jk_- x}\right)\,.\end{aligned} \tag{2.46}$$

The solution is

$$P^+(0 < x < l) = (\mathcal{D}x + \mathcal{C}_1)\, e^{-jk_+ x} + (\mathcal{E}x + \mathcal{C}_2)\, e^{jk_+ x} + \mathcal{F}e^{-jk_- x} + \mathcal{G}e^{jk_- x}\,, \tag{2.47}$$

where

$$\begin{aligned} \mathcal{D} &= \frac{j\beta_s k_+^2 A_1 A_2}{2k_+ \rho_s c_s^2}\,, \quad \mathcal{E} = \frac{-j\beta_s k_+^2 B_1 B_2}{2k_+ \rho_s c_s^2}\,, \\ \mathcal{F} &= \frac{(\beta_s - 1)k_+^2 - k_-^2}{(k_+^2 - k_-^2)\rho_s c_s^2} A_1 B_2\,, \quad \mathcal{G} = \frac{(\beta_s - 1)k_+^2 - k_-^2}{(k_+^2 - k_-^2)\rho_s c_s^2} A_2 B_1\,, \end{aligned} \tag{2.48}$$

and $\mathcal{C}_1$ and $\mathcal{C}_1$ are the two homogeneous solutions of Eqn. (2.46). The amplitudes of the waves radiated into the fluid are

$$P^+ = \begin{cases} P^+_{\text{left}} e^{jk_{f+}} & x < 0\,, \\ P^+_{\text{right}} e^{-jk_{f+}(x-l)} & x > l\,, \end{cases} \tag{2.49}$$

where $k_{f+} = \omega_+/c_f$. Particle velocity is determined by applying the momentum equation to Eqns. (2.47) and (2.49). The expressions for P^+_{left} and P^+_{right}, given in App. B, are obtained by equating pressure and velocity across interfaces at $x = 0$ and $x = l$.

2.3.3 Approximate expression for sum-frequency radiation

The expressions for the sum-frequency signals radiated into the fluid are simplified considerably when only inhomogeneous terms with spatial dependence $e^{\pm jk_+ x}$ are included. If f_1 and f_2 are the same, the factor $e^{\pm jk_- x}$ is unity, so terms with this spatial dependence are identified as analogues to the third terms in the numerators of Eqns. (2.28) and (2.29), which are the spatially-independent terms in the monofrequency analysis. Because the effect of the analagous terms is small at frequencies of interest in the monofrequency section (recall Fig. 2.6), it is possible that the effects of terms with spatial dependence $e^{\pm jk_- x}$ in the bifrequency configuration are also small. Here we develop the expressions for P^+_{left} and P^+_{right}, including only terms with spatial dependence $e^{\pm jk_+ x}$. In App. B, the resulting simplified expressions are compared with the full expressions. Differences between the solutions are within a few percent at all frequencies considered.

The equation that describes the weakly nonlinear generation of sum-frequency sound in a plate, with only forcing terms with spatial dependence $e^{\pm jk_+ x}$ taken into account, is

$$\left(\frac{d^2}{dx^2} + k_+^2\right) P^{(2)} = \frac{\beta_s k_+^2}{\rho_s c_s^2} \left(A_1 A_2 e^{-jk_+ x} + B_1 B_2 e^{jk_+ x}\right) . \tag{2.50}$$

We solve Eqn. (2.50) in the same manner as in Sec. 2.3.2 to obtain

$$P^+(0 < x < l) = (\mathcal{D}x + \mathcal{C}_1)\, e^{-jk_+ x} + (\mathcal{E}x + \mathcal{C}_2)\, e^{jk_+ x}\,, \tag{2.51}$$

where $\mathcal{D}$ and $\mathcal{E}$ are defined in Eqn. (2.48). Pressure amplitudes in the fluid are given in Eqn. (2.49). The particle velocity in the plate and in the fluid is determined by applying Eqn. (2.3) to Eqns. (2.51) and (2.49), respectively. Equating pressures and particle velocities across boundaries at $x = 0$ and $x = l$ and solving the resulting equations for P^+_{left} and P^+_{right} gives the expressions for the sum-frequency signals radiated into the fluid:

$$P^+_{\text{left}} = -\frac{j\beta_s k_+ l}{2\rho_s c_s^2} \frac{A_1 A_2 (1 - \frac{z_f}{z_s}) e^{-jk_+ l} + B_1 B_2 (1 + \frac{z_f}{z_s}) e^{jk_+ l}}{\cos k_+ l + \frac{j}{2}(\frac{z_f}{z_s} + \frac{z_s}{z_f}) \sin k_+ l}\,, \tag{2.52}$$

$$P^+_{\text{right}} = \frac{j\beta_s k_+ l}{2\rho_s c_s^2} \frac{A_1 A_2 (1 + \frac{z_f}{z_s}) - B_1 B_2 (1 - \frac{z_f}{z_s})}{\cos k_+ l + \frac{j}{2}(\frac{z_f}{z_s} + \frac{z_s}{z_f}) \sin k_+ l}\,. \tag{2.53}$$

The function $|P^+_{\text{right}}|$ is plotted in Fig. 2.10 for the case of an aluminum plate in water. Properties for the plate are given in Table A.1. The point at which f_1 and f_2 are at the pass bands is indicated by an arrow. The peak value of P^+_{right} does not occur at the pass-band frequencies where the amplitudes in the plate are at a maximum. Rather, the maximum values of P^+_{right} occur slightly away from the pass bands. Figure 2.11 shows $|P^+_{\text{right}}|$ as a function of f_1 with f_2 slightly below the pass band at 2.05 MHz (left), at the pass band at 2.075 MHz (center), and slightly above the pass band at 2.10 MHz (right). Arrows indicate the pass band at 1.04 MHz for f_1. It is shown in Fig. 2.11 that there are two resonances over the range of frequencies considered, one at which f_1 is slightly above the pass band and f_2 is slightly below the pass band, and the other at which f_1 is slightly below the pass band and f_2 is slightly above the pass band. The maximum sum-frequency radiation over the displayed range of frequencies is approximately $|P^+_{\text{right}}/P_{1i}P_{2i}| = 2.5 \times 10^{-9}$ Pa^{-1} (P_{1i}, P_{2i} having units of Pa). For example, for magnitudes of P_{1i} and P_{2i} around 200 kPa, $|P^+_{\text{right}}|$ is on the order of 50 Pa.

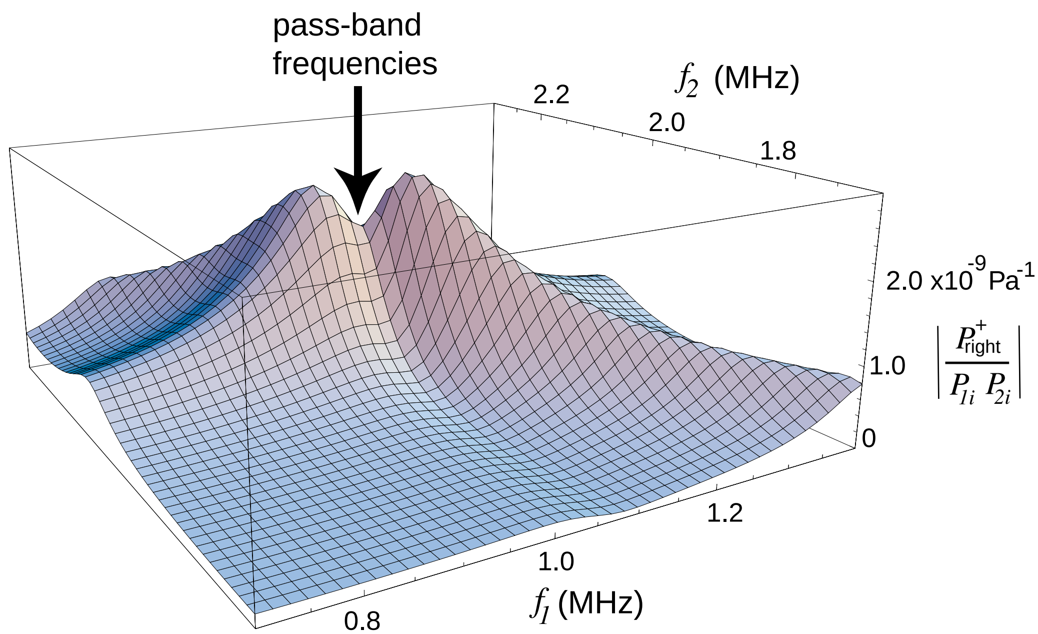

Figure 2.10: Radiation from plate.

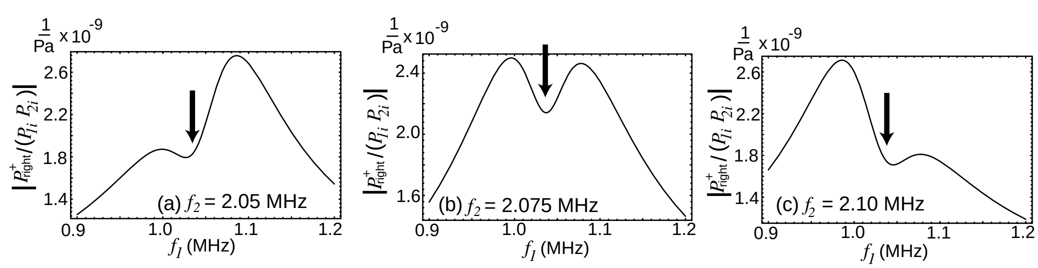

Figure 2.11: Radiation from plate: (a) $f_2 = 2.05$ MHz, slightly below the pass band; (b) f_2 at the pass band, 2.075 MHz; (c) $f_2 = 2.10$ MHz, slightly above the pass band. Arrows indicate the pass band for f_1, 1.04 MHz.

2.4 Experiment

2.4.1 Experimental arrangement

An experiment corresponding to the theory presented in Sec. 2.3.2 was performed. It was pointed out in Sec. 2.2.3 that, if a sound beam is used, there are differences between plane-wave theory and measurement due to diffraction effects. With that in mind, the focus of the experiment was to determine whether the arrangement discussed in Sec. 2.3.2 is feasible. One aspect that needed to be determined was the minimum distance the hydrophone could be placed from the plate. Although the hydrophone is approximately impedance matched to the water, there is some mismatch and, as a result, some reflection of an incident sound beam ($|W| \approx 0.95$ at 2 MHz[75]). If the hydrophone is placed too close to the plate, multiple reflections occur between the hydrophone and the plate. Another aspect that needed to be determined was the maximum amplitude that could be chosen for the primary sound beams before overloading the receiving apparatus. This imposed a limit on the attainable signal-to-noise ratio.

As shown in Fig. 2.12, two sources are placed on opposite sides of the plate. A PVDF membrane hydrophone is placed between one of the sources and the plate to measure the sound radiated from the plate. The membrane hydrophone is positioned at a distance d_h from the plate.

There are two contributions to sum-frequency pressure measured at the hydrophone. One is the sum-frequency pressure radiated from the plate, with amplitude P_s^+. The other is the sum-frequency pressure with amplitude P_f^+ generated in the fluid by the interaction of the sound beams propagating together from the plate to the receiver. This is illustrated in Fig. 2.13. It is straightforward, though, to predict the sum-frequency pressure generated in the fluid if the amplitudes of the sound beams at the primary frequencies are measured. It is also straightforward to measure the amplitudes of the sound beams at the primary frequencies at the same point at which the amplitude of the sum-frequency signal is measured. For this reason we develop an equation in which the sum-frequency

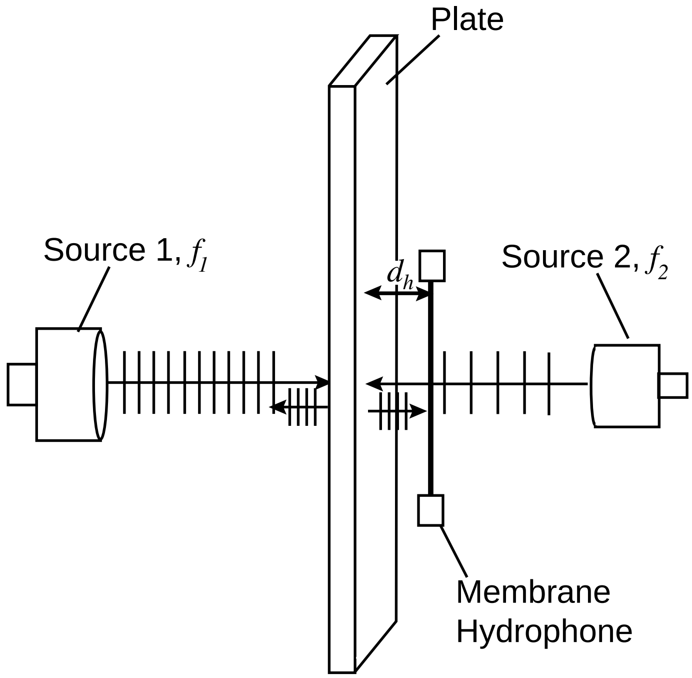

Figure 2.12: Experimental arrangement for two-beam experiment.

signal generated in the plate is expressed as a deviation from the sum-frequency signal that would be generated from two plane waves propagating together.

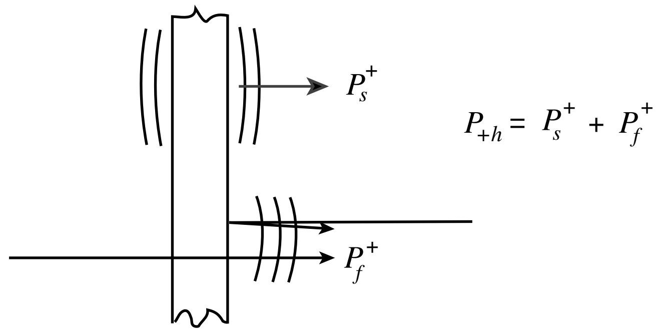

Figure 2.13: The sum-frequency pressure measured at the hydrophone, P_{+h}, is composed of P_f^+ plus P_s^+.

We denote the pressures received at the hydrophone as P_{1h}, P_{2h}, and P_{+h}, at frequencies f_1, f_2, and f_+, respectively. We wish to develop an equation that predicts the behavior of P_{+h} with respect to the product $P_{1h}P_{2h}$, accounting for sum-frequency generation in the plate and in the fluid. First we must relate P_{1h} and P_{2h} to the waves incident upon the plate with amplitudes of the incident waves P_{1i} and P_{2i}. Using Eqn. (2.5) for the linear transmission through the plate, we obtain

$$\frac{P_{1h}}{P_{1i}} = \frac{1}{\cos k_1 l + \frac{j}{2}\left(\frac{z_f}{z_s} + \frac{z_s}{z_f}\right)\sin k_1 l}\,, \tag{2.54}$$

and using Eqn. (2.6) for the linear reflection from the plate, we have

$$\frac{P_{2h}}{P_{2i}} = \frac{j\left(\frac{z_s}{z_f} - \frac{z_f}{z_s}\right)\sin k_2 l}{2\cos k_2 l + j\left(\frac{z_f}{z_s} + \frac{z_s}{z_f}\right)\sin k_2 l}\,, \tag{2.55}$$

where $k_{1,2} = \omega_{1,2}/c_s$.

In the quasilinear approximation, the amplitude of the sum-frequency pressure generated by plane waves with amplitudes P_{1h} and P_{2h} in the distance d_h from the plate to the hydrophone is[70]

$$P_f^+ = j\frac{\beta_f \omega_+ d_h P_{1h} P_{2h}}{2\rho_f c_f^3} e^{-jk_+ x}\,. \tag{2.56}$$

From Eqns. (2.53)–(2.56), the predicted amplitude $P_{+h} = P_f^+ + P_s^+$ of the sum-frequency pressure at the hydrophone, normalized by $|P_f^+|$, is

$$\frac{2\rho_f c_f^3}{\beta_f \omega_+ d_h}\left(\frac{P_{+h}}{P_{1h}P_{2h}}\right) = j + \left(\frac{\beta_s}{\beta_f}\right)\left(\frac{\rho_f c_f^3}{\rho_s c_s^3}\right)\left(\frac{l}{d_h}\right)\frac{\left(\frac{z_f}{z_s}-1\right)\left(\frac{z_s}{z_f}+1\right)}{\left(\frac{z_s}{z_f}-\frac{z_f}{z_s}\right)\sin k_2 l}$$
$$\times\frac{\cos k_1 l + j\frac{z_s}{z_f}\sin k_1 l}{\cos\left(k_1+k_2\right)l + \frac{j}{2}\left(\frac{z_f}{z_s}+\frac{z_s}{z_f}\right)\sin\left(k_1+k_2\right)l}\,. \qquad (2.57)$$

Equation (2.57) shows that if β_f and the linear material parameters are known, we can determine β_s by measuring P_{+h}, P_{1h}, and P_{2h}.

Several features of Eqn. (2.57) merit discussion. Complex pressure amplitudes (i.e., magnitude and relative phase) P_{1h}, P_{2h}, and P_+ are measured simultaneously at the receiver, which is convenient for purposes of an experiment. Moreover, the right-hand side of Eqn. (2.57) does not depend on the magnitudes of the incident waves P_{1i} and P_{2i}. However, it is strongly dependent, in both magnitude and phase, on k_1 and k_2. Another feature is that the second term on the right-hand side of Eqn. (2.57) is proportional to $\rho_f c_f^3/\rho_s c_s^3$. This implies that increasing the ratios of sound speed and density between the plate and the surrounding fluid, while increasing the resonant amplification in the plate, will decrease the ratio of the sum-frequency signal generated in the plate to the sum-frequency signal generated in the fluid.

The two sources used in the experiment were both circular plane piston transducers. The source at f_1 had a radius of 1.91 cm and resonance frequency of 1 MHz, with an effective source pressure of 254 kPa, and the source at f_2 had a radius of 1.26 cm and a resonance frequency of 2.25 MHz with a source pressure of 108 kPa. The source at f_1 was placed 250 mm from the plate, and the source at f_2 was placed 257 mm from the plate. The small difference in distances is an adjustment so that the steady-state portion of the tone bursts from each source arrived at the hydrophone at the same time. The nominal distance of 250 mm is approximately $z_0/3$, where $z_0 = ka^2/2$ is the Rayleigh distance. This distance from the sources to the plate was chosen to avoid nearfield oscillations. The hydrophone was placed at $d_h = 25$ mm from the plate, on the side with the source of frequency f_2.

The plate used was of aluminum, with the material parameters given in Table A.1. The height and width of the plate were sufficient that any reflections from plate edges did not arrive in time to interfere with the primary pulse. A stand, shown in Fig. 2.14, was built to hold the plate upright. The apparatus was aligned such that the sound beams were parallel to each other and normal to the plate to within approximately 0.1°.

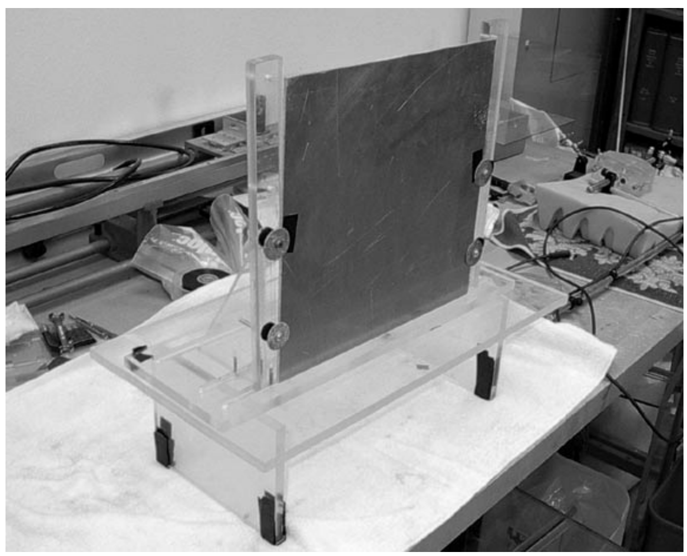

Figure 2.14: Photograph of the stand built to hold plates upright in the water.

2.4.2 Results and discussion

The results of this experiment are shown in Fig. 2.15. In Fig. 2.15(a) the magnitude of the quantity Φ, which is defined as

$$\Phi \equiv \frac{2\rho_f c_f^3}{\beta_f \omega_+ d_h} \left(\frac{P_{+h}}{P_{1h} P_{2h}} \right) , \tag{2.58}$$

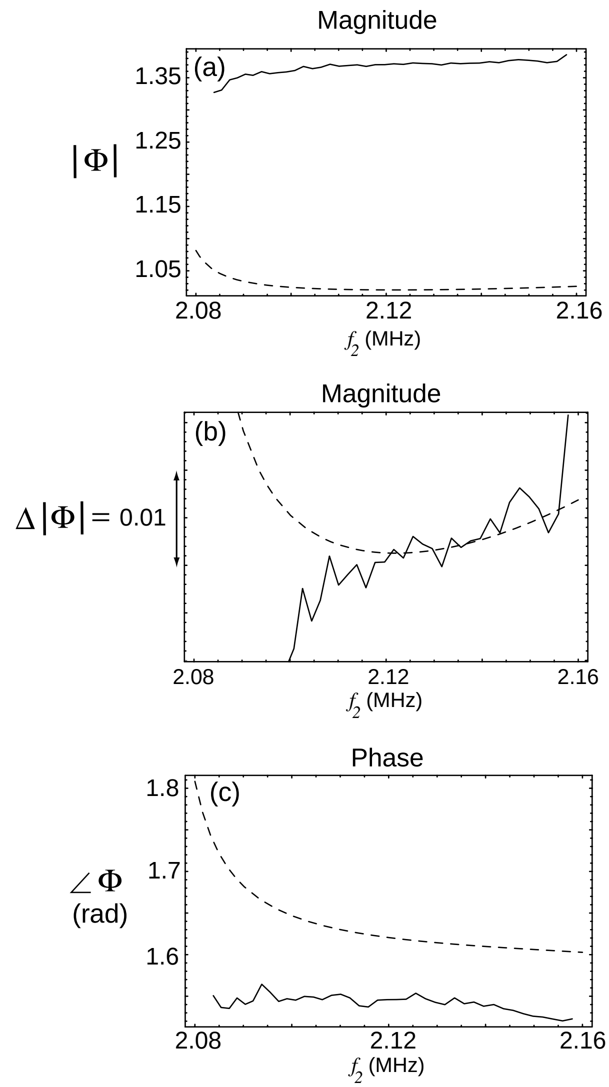

Figure 2.15: Comparison of experimental results of two-beam experiment (——) with theory (- - -) with an aluminum plate in water.

is compared with the theoretical prediction. The theory underestimates the measurement. The discrepancy between theory and measurement is equivalent to a deviation in P_{+h} of about 2 dB from plane-wave theory. In Fig. 2.15(b) we ignore the discrepancy between the magnitudes of the prediction and theory, and only compare the slopes. There is some qualitative agreement between the slopes for $f_2 \gtrsim 2.12$ MHz. For $f_2 \lesssim 2.12$ MHz the measured slope deviates significantly from the theory. This is close to a critical frequency at which a Lamb wave is excited in the plate, so rapid variations of the acoustic field in the plate were probably occurring as the frequency was varied. The noise present in the measurement indicates that the magnitude of changes in Φ due to the nonlinearity of the plate are at the same level as the noise floor of the experimental apparatus.

In Fig. 2.15(c) the measurement of the phase of Φ is compared with the theory. Although there is a discrepancy between the phases, there is qualitative agreement beween the phase changes in the theory and in the measurements at frequencies $\gtrsim 2.1$ MHz. Even so, changes in the phase from $f_2 = 2.1$ to 2.16 MHz are very small, on the order of 2°, approaching the limitations in resolution of the apparatus.

Although the sum-frequency signal generated in the plate is very weak, we felt that it may be possible to detect it with some accuracy given the capability the apparatus has for making high-resolution measurements. However, Fig. 2.15 shows significant differences between theory and experiment. Moreover, changes in the magnitude and phase of Φ over the bandwidth of the source are very small. While differences between theory and measurement can potentially be resolved by including diffraction effects in the model, we felt there was little value in doing so because changes in the received signal needed to estimate β_s are too small to be measured accurately.

In Sec. 2.3.2 we proposed a bifrequency technique to determine β_s for an immersed plate. A plane-wave model was developed to predict the sum-frequency signal radiated from the plate. An experiment was performed to determine the feasibility of the technique is reported in Sec. 2.4. The apparatus was configured in the most favorable manner we could conceive for measuring the nonlinearity of the plate. Even so, changes in Φ that are attributable to the nonlinearity of the plate are too small to provide an accurate estimate of β_s.

Chapter 3

NONLINEAR RESPONSE OF BONDED PLATES

As discussed in Chap. 1, nondestructive evaluation methods that exploit contact nonlinear phenomena show promise for the detection of cracks and disbonds, because the detection of contact nonlinearity can be a strong indicator of damage or defects in a sample. While material parameters related to linear acoustic propagation change on the order of a few percent when defects such as microcracks are present,[3] nonlinear effects associated with defects can increase by orders of magnitude.[6] Of particular relevance to the work in this chapter is the nonlinearity associated with a contact boundary between solids. A number of experimenters have reported the nonlinear transmission and reflection of acoustic waves at a contact interface.[1]

In this chapter we consider the interaction of a plane wave with two homogeneous, elastic, isotropic plates that meet at a planar nonlinear interface. The interface is modeled as a nonlinear spring. It is hoped that, in an experiment, the contact boundary between the plates will be the source of anomalous nonlinearity. We therefore assume in our analysis that the generation of a second harmonic takes place only at the boundary between the two plates, and not within the plates themselves. There are two aspects of our investigation that distinguish it from previous work. First, we consider plate-like samples in which resonant behavior is anticipated, in contrast to earlier studies of contact nonlinearity at interfaces (with the exception of the study by Rothenfusser *et al.*,[37] discussed in Sec. 1.1.1) that consider the contact between solid half-spaces. Moreover, we perform our experiment using sound beams generated by immersion transducers, rather than using contact transducers coupled directly to the samples.

3.1 Linear Theory

In this section we develop expressions for the linear transmisison and reflection of a plane wave normally incident upon two plates connected by a compliant interface. Such an interface may be a model for two solids with rough surfaces pressed together (see, for example, Ref. 30), or for two bonded solids (see, for example, Ref. 71). Because the incident plane wave is normal to the interface, no shear waves are generated in the plate. (The same is approximately true for directional sound beams.) The excitation is time-harmonic, and a steady state is assumed in our analysis.

3.1.1 General linear reflection and transmission

The configuration we consider is illustrated in Fig. 3.1. A plane wave of pressure amplitude P_i and angular frequency ω is incident normally upon two isotropic plates. A plane wave with pressure amplitude P_r is reflected back towards the source, and another with amplitude P_t is transmitted out from the far side of the plates. The standing waves in the interior are represented by plane waves of amplitude A_1 and B_1 propagating forward and backward, respectively, in the first plate, and A_2 and B_2 propagating forward and backward in the second plate. (In Chap. 2, the subscripts 1 and 2 indicated which source generated the wave. In this chapter, the subscripts denote a wave in the first or second plate.) The total thickness of the two plates is l, the first plate has thickness d, and the second plate has thickness $h = l - d$.

We express the acoustic pressure p in the four regions as

$$p = \frac{1}{2}\begin{cases} P_i e^{j(\omega t - k_f x)} + P_r e^{j(\omega t + k_f x)} + \text{c.c.}\,, & x < 0\,, \\ A_1 e^{j(\omega t - k_{s1} x)} + B_1 e^{j(\omega t + k_{s1} x)} + \text{c.c.}\,, & 0 \le x \le d\,, \\ A_2 e^{j[\omega t - k_{s2}(x-d)]} + B_2 e^{j[\omega t + k_{s2}(x-d)]} + \text{c.c.}\,, & d \le x \le l\,, \\ P_t e^{j[\omega t - k_f (x-l)]} + \text{c.c.}\,, & x > l\,, \end{cases} \tag{3.1}$$

where $k_i = \omega/c_i$, c_f is the sound speed in the fluid, and $c_{s1,s2}$ is the longitudinal wave speed in plate 1 or 2. Because we assume that wave propagation is only in

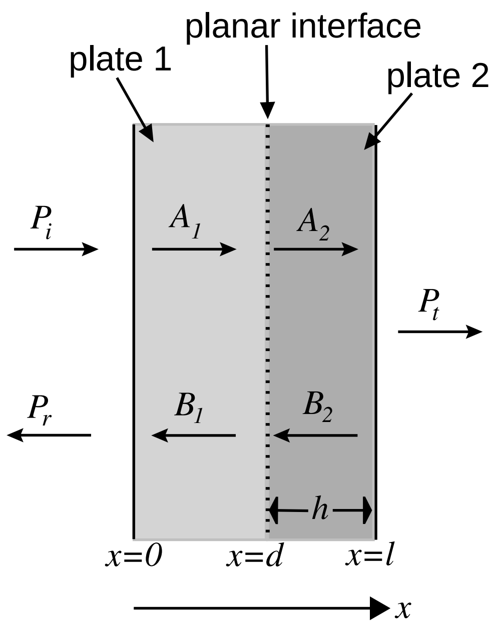

Figure 3.1: System of plane waves for two immersed plates with a planar interface, and incident wave arriving from the left.

the x direction, we define u to be the x component of the particle velocity vector, and there is no particle velocity in the y or z direction. We determine u using Eqn. (3.1) and the linearized momentum equation in one dimension, Eqn. (2.3). As in Chap. 2, equations for fluids are used for the plate because the motion is entirely one-dimensional. The result is

$$u = \frac{1}{2}\begin{cases} g_f\left(P_i e^{j(\omega t - k_f x)} - P_r e^{j(\omega t + k_f x)}\right) + \text{c.c.}\,, & x < 0\,, \\ g_{s1}\left(A_1 e^{j(\omega t - k_{s1} x)} - B_1 e^{j(\omega t + k_{s1} x)}\right) + \text{c.c.}\,, & 0 \le x \le d\,, \\ g_{s2}\left(A_2 e^{j[\omega t - k_{s2}(x-d)]} - B_2 e^{j[\omega t + k_{s2}(x-d)]}\right) + \text{c.c.}\,, & d \le x \le l\,, \\ g_f P_t e^{j[\omega t - k_f(x-l)]} + \text{c.c.}\,, & x > l\,, \end{cases} \tag{3.2}$$

where we define the conductances g_j as

$$g_j = \frac{1}{z_j} = \frac{1}{\rho_j c_j}\,. \tag{3.3}$$

The index notation is the same, with $j = f, s1, s2$ corresponding to fluid, plate 1, and plate 2, respectively.

We determine boundary conditions at $x = d$ using a spring model, illustrated in Fig. 3.2.[30] Here,

$$\xi_{d\pm} \equiv \xi(d \pm \delta/2, t)\,, \quad \delta \to 0\,, \tag{3.4}$$

where ξ is particle displacement, and the gap of width δ is populated by linear springs of infinitesimal lengths and stiffness per unit area κ. (In Sec. 3.2 we consider springs with quadratic nonlinearity.) At $x = d$ the pressure (stress) is equal across the interface (because the springs are massless elements), so we set [with $d_\pm$ defined in Eqn. (3.4)]

$$p_{d-} = p_{d+}\,. \tag{3.5}$$

The condition for the springs at the interface (Hooke's Law) is

$$p\big|_{x=d} = \kappa(\xi_{d-} - \xi_{d+})\,. \tag{3.6}$$

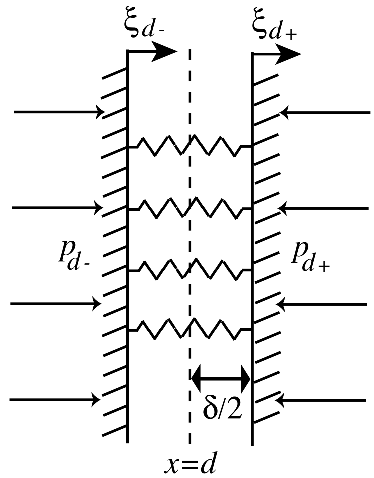

Figure 3.2: Compliant planar interface at $x = d$.

Taking the time derivative of Eqn. (3.6) to give the boundary condition in terms of pressure and particle velocity yields

$$\left.\frac{\partial p}{\partial t}\right|_{x=d} = \kappa(u_{d-} - u_{d+})\,. \tag{3.7}$$

Because all waves are time-harmonic with angular frequency ω, Eqns. (3.1) and (3.2) and the boundary conditions at $x = d$ give

$$A_1 e^{-jk_{s1}d} + B_1 e^{jk_{s1}d} = A_2 + B_2\,, \tag{3.8}$$

and

$$j\omega C\left(A_1 e^{-jk_{s1}d} + B_1 e^{jk_{s1}d}\right) = g_{s1}\left(A_1 e^{-jk_{s1}d} - B_1 e^{jk_{s1}d}\right) - g_{s2}\left(A_2 - B_2\right), \tag{3.9}$$

where we define the compliance $C \equiv 1/\kappa$.

In addition to the boundary conditions given by Eqns. (3.5) and (3.7), boundary conditions at $x = 0$ and l are

$$p_{0-} = p_{0+}\,, \tag{3.10}$$

$$u_{0-} = u_{0+}\,, \tag{3.11}$$

$$p_{l-} = p_{l+}\,, \tag{3.12}$$

$$u_{l-} = u_{l+}\,, \tag{3.13}$$

where the notation follows Eqn. (3.4), and $x\pm \equiv x \pm \delta/2$. From these six boundary conditions, the amplitudes P_r and P_t may be expressed in terms of A_1, B_1, A_2, and B_2. The latter four amplitudes are related by the matrix system

$$\begin{pmatrix} 1+\frac{g_{s1}}{g_f} & 1-\frac{g_{s1}}{g_f} & 0 & 0 \\ (1-\frac{g_{s1}}{j\omega C})e^{-jk_{s1}d} & (1+\frac{g_{s1}}{j\omega C})e^{jk_{s1}d} & \frac{g_{s2}}{j\omega C} & -\frac{g_{s2}}{j\omega C} \\ e^{-jk_{s1}d} & e^{jk_{s1}d} & -1 & -1 \\ 0 & 0 & (1-\frac{g_{s2}}{g_f})e^{-jk_{s2}h} & (1+\frac{g_{s2}}{g_f})e^{jk_{s2}h} \end{pmatrix} \begin{pmatrix} A_1 \\ B_1 \\ A_2 \\ B_2 \end{pmatrix} = \begin{pmatrix} 2P_i \\ 0 \\ 0 \\ 0 \end{pmatrix}. \tag{3.14}$$

The reflection coefficient

$$V \equiv P_r/P_i \tag{3.15}$$

is thus determined to be

$$\begin{aligned} V = \frac{1}{g_f g_{s1} g_{s2}\Delta}\Big\{ & \Big[j\omega C(g_{s1}g_{s2} - g_f^2) + g_f(g_{s1}^2 - g_{s2}^2)\Big]\, j\cos(k_{s1}d + k_{s2}h) \\ + & \Big[j\omega C g_f(g_{s2} - g_{s1}) + (g_f^2 - g_{s1}g_{s2})(g_{s1} + g_{s2})\Big] \sin(k_{s1}d + k_{s2}h) \\ + & \Big[j\omega C(g_f^2 + g_{s1}g_{s2}) + g_f(g_{s2}^2 - g_{s1}^2)\Big]\, j\cos(k_{s1}d - k_{s2}h) \\ + & \Big[j\omega C g_f(g_{s1} + g_{s2}) + (g_{s2} - g_{s1})(g_f^2 + g_{s1}g_{s2})\Big] \sin(k_{s1}d - k_{s2}h)\Big\}, \end{aligned} \tag{3.16}$$

and the transmission coefficient

$$W \equiv P_t/P_i \tag{3.17}$$

is determined to be

$$W = -\frac{4j}{\Delta}, \tag{3.18}$$

where

$$\begin{aligned} \Delta = \frac{1}{g_f g_{s1} g_{s2}}\Big\{ & -\Big[j\omega C(g_f^2 + g_{s1}g_{s2}) + g_f(g_{s1} + g_{s2})^2\Big]\, j\cos(k_{s1}d + k_{s2}h) \\ & + \Big[j\omega C g_f + (g_f^2 + g_{s1}g_{s2})\Big]\,(g_{s1} + g_{s2}) \sin(k_{s1}d + k_{s2}h) \\ & + \Big[j\omega C(g_f^2 - g_{s1}g_{s2}) + g_f(g_{s1} - g_{s2})^2\Big]\, j\cos(k_{s1}d - k_{s2}h) \\ & + \Big[j\omega C g_f + (g_f^2 - g_{s1}g_{s2})\Big]\,(g_{s2} - g_{s1}) \sin(k_{s1}d - k_{s2}h)\Big\}. \end{aligned} \tag{3.19}$$

We investigate the properties of Eqns. (3.16) and (3.18) in the following sections.

3.1.2 Natural frequencies of joined plates

It is helpful for developing an intuitive feel for the system response to examine the eigenvalues of the matrix on the left side of Eqn. (3.14). Its eigenvalues correspond to the natural frequencies of the joined plates. Taking the determinant of the matrix on the left side of Eqn. (3.14) and setting it equal to zero gives

$$\begin{aligned} &\left[1+\frac{g_{s1}g_{s2}}{g_f^2}+\frac{(g_{s1}+g_{s2})^2}{j\omega C g_f}\right]\cos(k_{s1}d+k_{s2}h) \\ &+j\left[\frac{g_{s1}+g_{s2}}{g_f}+\left(1+\frac{g_{s1}g_{s2}}{g_f^2}\right)\frac{g_{s1}+g_{s2}}{j\omega C}\right]\sin(k_{s1}d+k_{s2}h) \\ &-\left[1-\frac{g_{s1}g_{s2}}{g_f^2}+\frac{(g_{s1}-g_{s2})^2}{j\omega C g_f}\right]\cos(k_{s1}d-k_{s2}h) \\ &-j\left[\frac{g_{s1}-g_{s2}}{g_f}+\left(1-\frac{g_{s1}g_{s2}}{g_f^2}\right)\frac{g_{s1}-g_{s2}}{j\omega C}\right]\sin(k_{s1}d-k_{s2}h)=0\,. \end{aligned} \tag{3.20}$$

For plates in vacuum, $g_f \to \infty$ and Eqn. (3.20) reduces to

$$\sin k_{s1}d\sin k_{s2}h-\frac{g_{s1}}{\omega C}\cos k_{s1}d\sin k_{s2}h-\frac{g_{s2}}{\omega C}\sin k_{s1}d\cos k_{s2}h=0\,. \tag{3.21}$$

Now consider plates of the same material and thickness, $g_{s1}=g_{s2}$, $k_{s1}=k_{s2}$, and $d=h$, such that Eqn. (3.21) reduces to

$$\sin k_{s1}d=0, \frac{2g_{s1}}{\omega C}\cos k_{s1}d\,. \tag{3.22}$$

The first set of roots ($k_{s1}d = n\pi$, corresponding to $\sin k_{s1}d = 0$) correspond to natural frequencies for which the pressure is zero at $x = d$. As a result, the springs are not deformed and these resonances are independent of C. The second set of roots correspond to natural frequencies for which the pressure is large at $x = d$, and thus they depend strongly on C. Here we examine this set of roots further.

It is convenient to rewrite Eqn. (3.22) for the second set of roots as

$$\cot k_{s1}d=\frac{1}{S}k_{s1}d\,, \tag{3.23}$$

where

$$S = \frac{\kappa l}{\rho_{s1} c_{s1}^2} = \frac{\kappa l}{K + \frac{4}{3}\mu} \tag{3.24}$$

is the stiffness of the junction relative to that of the material, with $l = 2d$ the total thickness, and K and μ the bulk and shear moduli for the material, respectively.

We plot the right- and left-hand sides of Eqn. (3.23) in Fig. 3.3. Parameters are chosen for two 1/16 in. aluminum plates joined with a bond with $\kappa = 10^{14}$ Pa/m ($S = 2.86$) and $\kappa = 10^{15}$ Pa/m ($S = 28.6$). Intersections between the curves, indicated by dots, correspond to natural frequencies of the plates. Squares indicate eigenvalues $k_{s1}d = n\pi$. As the boundary becomes more compliant, the odd (first, third, fifth, etc.) natural frequencies (dots) decrease while the even (second, fourth, sixth, etc.) natural frequencies (squares) do not change. An explanation for this behavior is that, as the plates decouple, the resonance behavior of the system changes from that of a single plate of thickness $2d$ to that of two plates of thickness d.

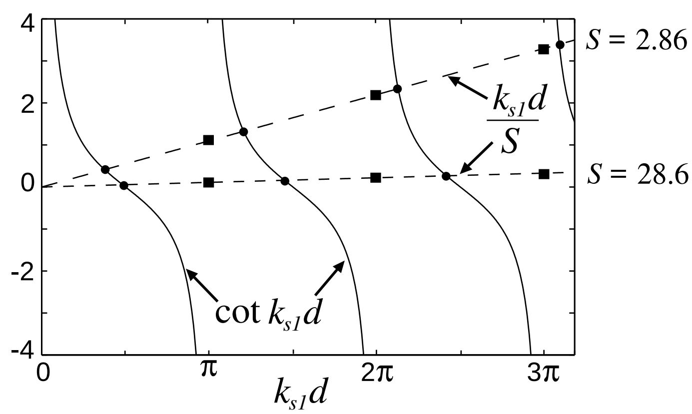

Figure 3.3: Eigenvalues for 1/16 in. aluminum plates in vacuum, $\kappa = 10^{14}$ Pa/m ($S = 2.86$) and $\kappa = 10^{15}$ Pa/m ($S = 28.6$).

Now we consider a different limit. If the two plates are of different materials and have different thicknesses, but they are in vacuum and the compliance

$C \rightarrow 0$, then Eqn. (3.21) reduces to

$$g_{s2} \tan k_{s1} d + g_{s1} \tan k_{s2} h = 0\,. \tag{3.25}$$

Equation (3.25) agrees with the result given by Graff[72] for the frequency response of compressional waves in two joined, thin rods (illustrated in Fig. 3.4). Graff's

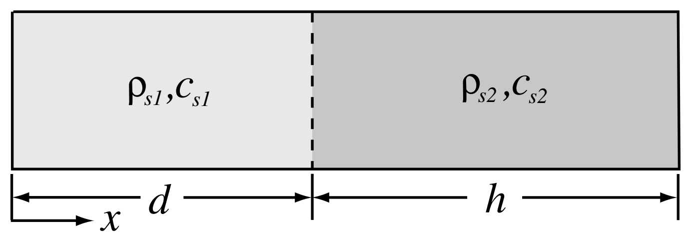

Figure 3.4: Two joined rods with different materials and lengths.

analysis was performed in terms of stress and displacement, whereas Eqn. (3.25) was determined using an analysis performed in terms of pressure and particle velocity.

3.1.3 Reflection and transmission coefficients for plates with equal thicknesses and impedances

In Sec. 3.1.2, we determined the natural frequencies of two bonded plates in vacuum and examined the behavior of the system under special conditions, for which Eqn. (3.20) for the natural frequencies was simplified. In this section we examine the behavior of the reflection and transmission coefficients for plates in a fluid, also under special conditions in which Eqns. (3.16) and (3.18) are simplified. This is done because Eqns. (3.16) and (3.18) do not lend themselves easily to physical interpretation. We consider the special case in which the two plates are made of the same material, and have the same thickness. The symmetry results in simplified equations for which the effect of the compliant boundary on the transmission and reflection of the plates is made more clear.

We set $\rho_{s1} = \rho_{s2}$, $c_{s1} = c_{s2}$, and $d = h = l/2$. As a consequence, $g_{s1} = g_{s2}$ and $k_{s1} = k_{s2}$. Equations (3.16) and (3.18) then reduce to

$$W = \frac{1}{\Delta}\,, \tag{3.26}$$

and

$$V = \frac{1}{\Delta}\left\{\frac{j\omega C}{4g_{s1}}\left[\left(\frac{g_f}{g_{s1}} - \frac{g_{s1}}{g_f}\right)\cos k_{s1}l - \left(\frac{g_f}{g_{s1}} + \frac{g_{s1}}{g_f}\right)\right] + \frac{j}{2}\left(\frac{g_f}{g_{s1}} - \frac{g_{s1}}{g_f}\right)\sin k_{s1}l\right\}, \tag{3.27}$$

where

$$\begin{aligned}\Delta = {} & \frac{j\omega C}{2g_{s1}}\left[\frac{1}{2}\left(\frac{g_f}{g_{s1}} + \frac{g_{s1}}{g_f}\right)\cos k_{s1}l + j\sin k_{s1}l + \frac{1}{2}\left(\frac{g_{s1}}{g_f} - \frac{g_f}{g_{s1}}\right)\right] \\ & + \cos k_{s1}l + \frac{j}{2}\left(\frac{g_f}{g_{s1}} + \frac{g_{s1}}{g_f}\right)\sin k_{s1}l\,. \end{aligned} \tag{3.28}$$

From Eqn. (3.28) we see that for $\omega C/2g_{s1} \ll 1$ the reflection and transmission coefficients are nearly the same as those for a single plate of thickness l [recall Eqn. (2.5)]. For $\omega C/2g_{s1} \sim 1$, however, the effects of the compliant interface at $x = l/2$ comes into play.

We may compare Eqns. (3.26) and (3.27) with some expected limiting behavior. As the interface at $x = d$ becomes infinitely stiff, the two plates are rigidly connected and we expect to recover the expressions for the reflection and transmission coefficients for a single plate of thickness l. Setting $C = 0$ in Eqns. (3.26)–(3.28) gives

$$W = \frac{1}{\cos k_{s1}l + \frac{j}{2}\left(\frac{g_f}{g_{s1}} + \frac{g_{s1}}{g_f}\right)\sin k_{s1}l}\,, \tag{3.29}$$

$$V = \frac{\frac{j}{2}\left(\frac{g_f}{g_{s1}} - \frac{g_{s1}}{g_f}\right)\sin k_{s1}l}{\cos k_{s1}l + \frac{j}{2}\left(\frac{g_f}{g_{s1}} + \frac{g_{s1}}{g_f}\right)\sin k_{s1}l}\,, \tag{3.30}$$

which are equivalent to Eqns. (2.5) and (2.6). For $C \to \infty$ we have $W \to 0$ because the interface between the plates becomes a free boundary. The reflection coefficient approaches

$$V = \frac{jg_f \sin k_{s1}d - g_{s1}\cos k_{s1}d}{jg_f \sin k_{s1}d + g_{s1}\cos k_{s1}d}\,, \quad \kappa = 0\,. \tag{3.31}$$

Equation (3.31) is the same as the plane-wave reflection coefficient for a wave normally incident upon a plate of thickness $d = l/2$ in front of a stress-free half space. (This result may be verified easily by following the analysis in Sec. 2.1, but setting $p = 0$ at $x = l/2$.) The magnitude of the reflection coefficient in Eqn. (3.31) is always unity, as we would expect: since $W = 0$, all incident energy is reflected back towards the source.

3.1.4 Theoretical predictions of transmission and reflection

The magnitude of the transmission coefficient $|W|$ for two aluminum plates, $d = h = 1/16$ in., and $\kappa = 10^{14}$ Pa/m, is shown in Fig. 3.5. The material properties for aluminum are given in Sec. 2.1. The transmission coefficient is plotted over a wide range of frequencies to show how the characteristics of the transmission change as frequency increases. At frequencies for which $\omega C/2g_{s1} \sim 1$ ($f \sim 2$ MHz), shifting of the pass-band frequencies occurs. This effect corresponds to the shifting of natural frequencies described in Sec. 3.1.2. As the excitation frequency increases so that $\omega C/2g_{s1} \gg 1$ ($f \gg 2$ MHz), the interface approaches a free boundary and transmission decreases, even at the pass bands.

The magnitude of the transmission coefficient $|W|$, and the corresponding reflection coefficient $|V|$, are shown in Fig. 3.6 for two aluminum plates with equal thicknesses, $d = h = 1/16$ in. Plots are shown for different stiffnesses at the boundary between the plates. For $\kappa = 10^{16}$ Pa/m (top row), $\omega C/2g_{s1} \approx 0.005$ at $f = 1$ MHz. At all frequencies shown, $|W|$ and $|V|$ are indistinguishable from those of a single 1/8 in. aluminum plate. As κ decreases, the system changes from responding as one 1/8 in. plate to responding as two 1/16 in. plates. Pass bands characteristic of a 1/8 in. plate gradually shift in frequency towards the pass bands for a 1/16 in. plate, as shown in the plots for which $\kappa = 10^{15}$ Pa/m (second row) and $\kappa = 10^{14}$ Pa/m (third row). This process first affects pass bands at high frequencies. As the pass bands merge, transmission at the stop bands between merging pass bands increases. An example of this can be seen at $f \approx 6.3$ MHz in the plot for which $\kappa = 10^{15}$ Pa/m (second row). Conversely, the magnitude of the transmission of stop bands between diverging pass bands decreases. For $\kappa = 10^{13}$ Pa/m (bottom row), $\omega C/2g_{s1} \approx 5$ at $f = 1$ MHz and the transmission coefficient approaches zero as frequency increases.

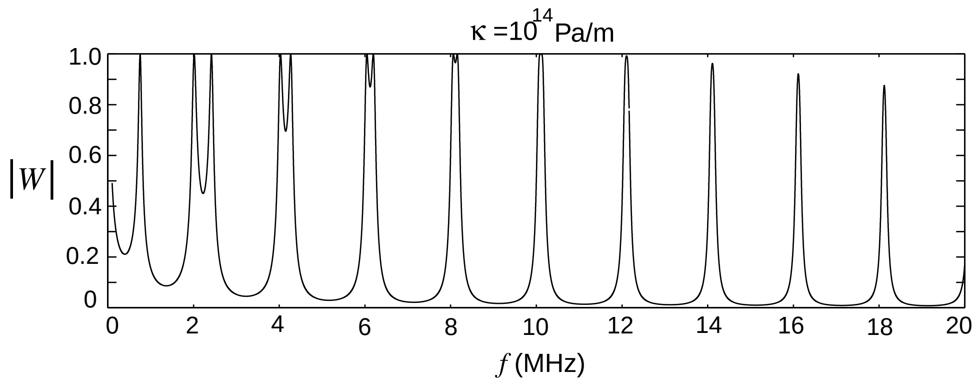

Figure 3.5: Magnitude of linear transmission coefficient for two bonded 1/16 in. aluminum plates with $\kappa = 10^{14}$ Pa/m.

The pressure and particle velocity in the plates may be determined if A_1, B_1, A_2, and B_2 are known, according to Eqns. (3.1) and (3.2). Examination of the pressure (negative stress) and particle velocity in the plates provides insight to the resonant behavior of the system. Pressure and particle velocity fields in two 1/16 in. aluminum plates are shown in Sec. 3.1.5.

The magnitude of the transmission coefficient given by Eqn. (3.18) and the reflection coefficient predicted by Eqn. (3.16) are plotted in Fig. 3.7 for two bonded aluminum plates with ratio 1:3 (left to right) in length, $d = 1/32$ in. and $h = 3/32$ in. As κ decreases, most of the transmission maxima diminish. However, the pass bands that are characteristic of a 1/32 in. plate remain until $\omega C/2g_{s1}$ becomes very large and the interface approaches a free boundary. There is some shifting of the frequencies of the pass bands, but not as much as in the case of two plates of the same thickness (recall Fig. 3.6). Although the system does not exhibit the symmetry seen in Fig. 3.6, the onset of effects due to the compliant interface still occurs for $\omega C/2g_{s1} \sim 1$. Reversing the plates so that $d = 3/32$ in. and $h = 1/32$ in. (thicker plate on the left) does not affect $|W|$ and $|V|$.

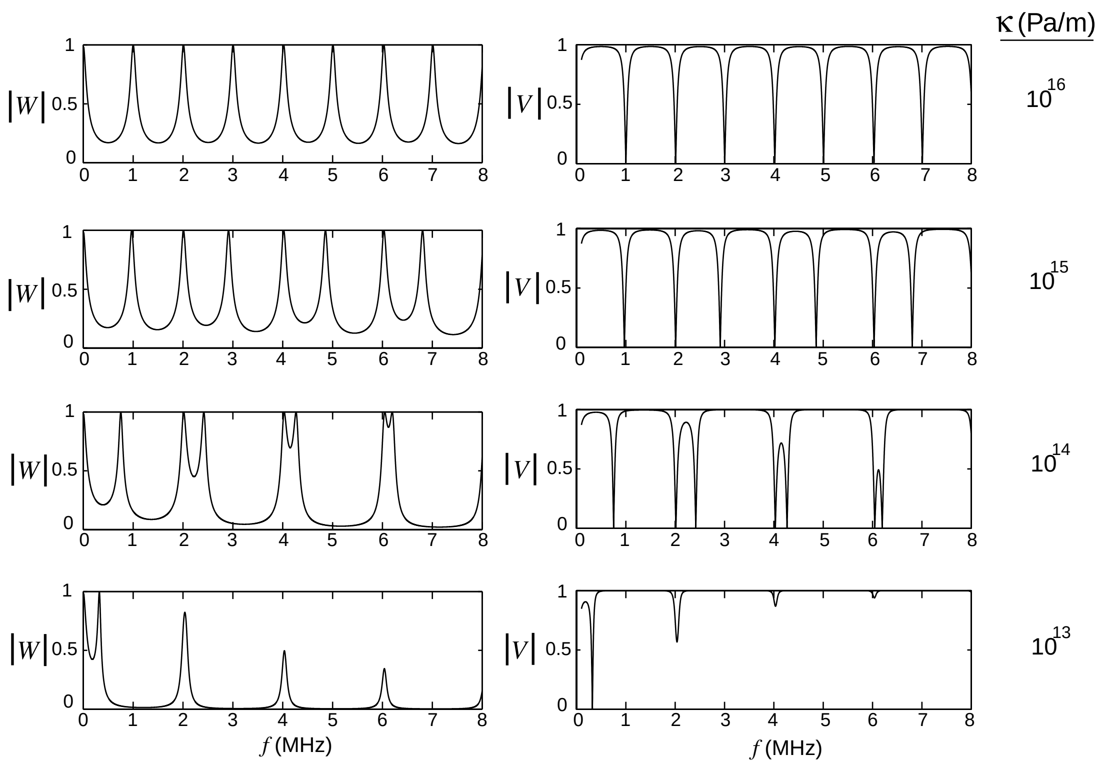

Figure 3.6: Magnitude of linear transmission and reflection coefficients for two bonded 1/16 in. aluminum plates.

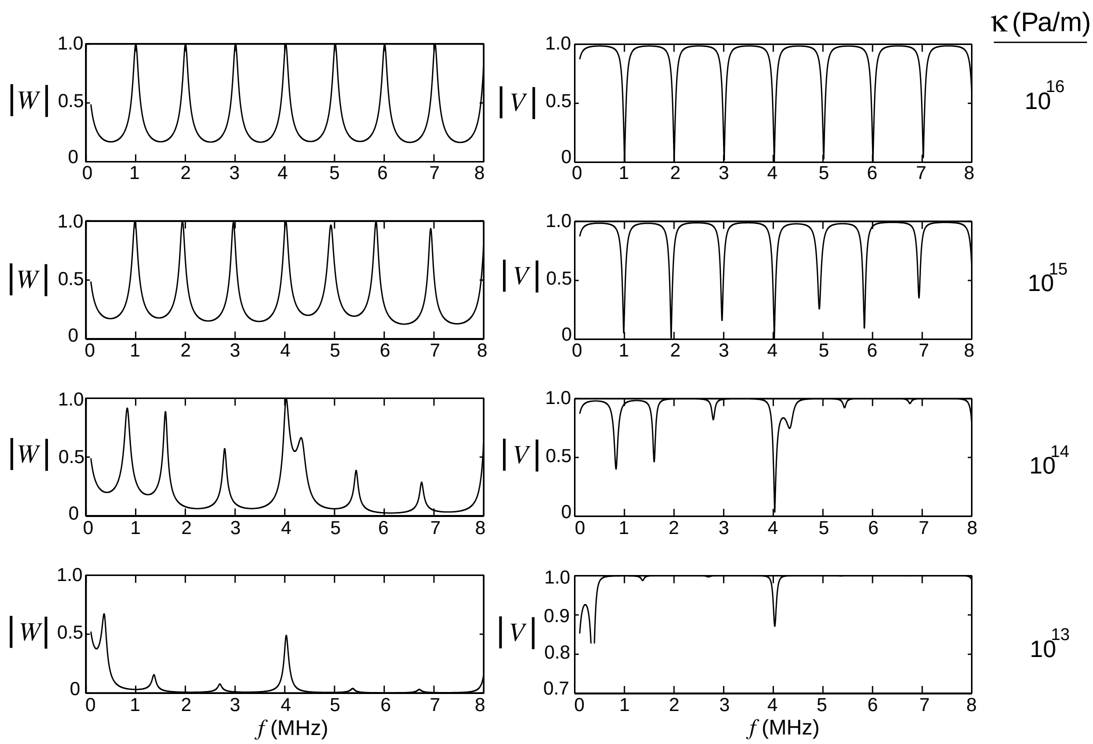

Figure 3.7: Magnitude of linear transmission and reflection coefficients for two bonded aluminum plates of different thicknesses, $d = 1/32$ in. and $h = 3/32$ in.

Transmission $|W|$ for the case of two bonded 1/16 in. plates, one aluminum and the other steel, and the corresponding reflection $|V|$ through the plates predicted by Eqn. (3.16), are plotted in Fig. 3.8. (The aluminum plate is closer to the source.) Material constants for steel are given in Table A.1. For $\kappa \to \infty$, odd transmission maxima have a magnitude of approximately 0.6, while even maxima have a magnitude of 1.0. Pass bands are at nearly the same frequencies as those for two aluminum plates, but this is not surprising because the sound speed in steel is approximately equal to the sound speed in aluminum and, from Eqn. (2.10), pass band frequencies are proportional to the speed of sound in a plate.

Shifting of the smaller transmission maxima is evident as κ decreases from 10^{16} to 10^{15} Pa/m. Because the two plates are different materials, we replace $\omega C/2g_{s1}$ with $\omega C/(g_{s1} + g_{s2})$ as the parameter that indicates the strength of the effects of the compliant interface on transmission and reflection. For steel and aluminum, $\omega C/2(g_{s1} + g_{s2}) \approx 0.5$ for $f = 7$ MHz and $\kappa = 10^{15}$ Pa/m. Correspondingly, the effects of the compliant interface are detectable as a shifting of the pass band. For example, the pass-band frequency shift near $f = 7$ MHz for $\kappa = 10^{15}$ Pa/m in Fig. 3.8 is significantly larger than the corresponding shift near $f = 7$ MHz seen in Fig. 3.6 at $\kappa = 10^{15}$ Pa/m. Reversing the order of the plates does not affect $|W|$ and $|V|$.

Magnitudes of transmission and reflection coefficients for two bonded 1/16 in. plates in water, one aluminum and the other acrylic, are shown in Fig. 3.9. Material properties for acrylic are given in Table A.1. There is more structure in Fig. 3.9 than in the previous figures because there are more resonances in the acrylic plate than in the metal plates. The sound speed in acrylic is lower than the sound speed in aluminum or steel, so the wavelength is shorter in acrylic, and thus the resonances are more closely spaced in frequency. Moreover, resonances corresponding to the acrylic plate are weaker than resonances corresponding to the aluminum plate. Resonances are visible that correspond to the individual 1/16 in. acrylic and aluminum plates, and as the bond stiffness decreases, resonances that correspond to the aluminum plate dominate. This is particularly

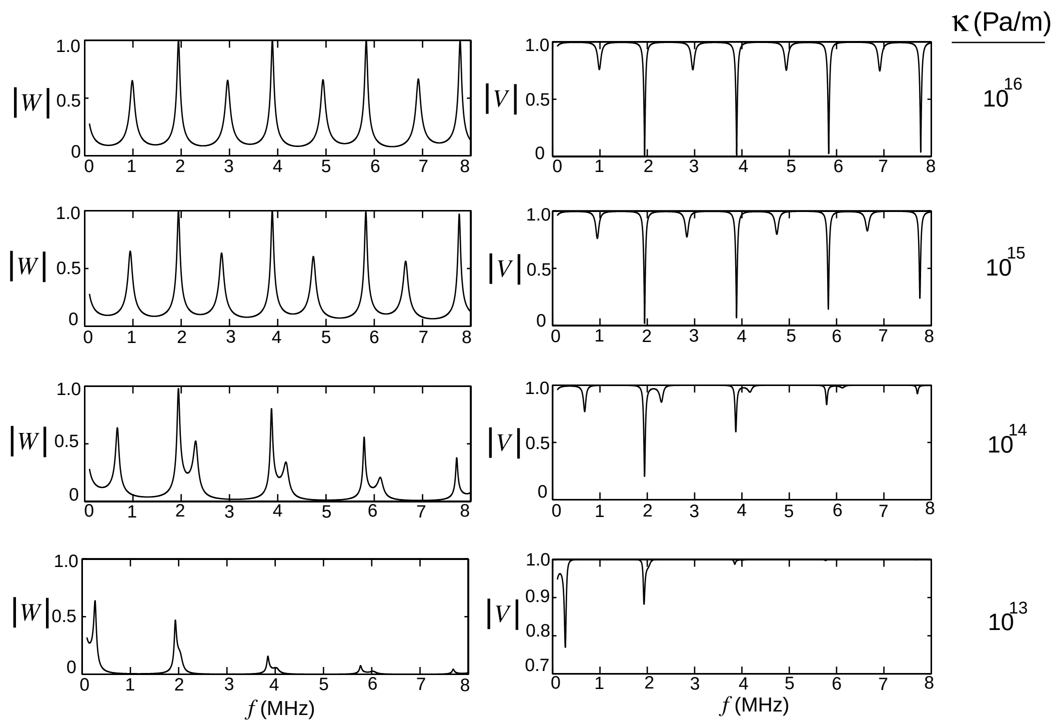

Figure 3.8: Magnitude of linear transmission and reflection coefficients for two bonded 1/16 in. plates of aluminum and steel. Aluminum plate is closer to the source. Material constants are given in Table A.1.

noticeable for $\kappa = 10^{13}$ Pa/m (bottom row). Reversing the order of the plates does not affect $|W|$ and $|V|$.

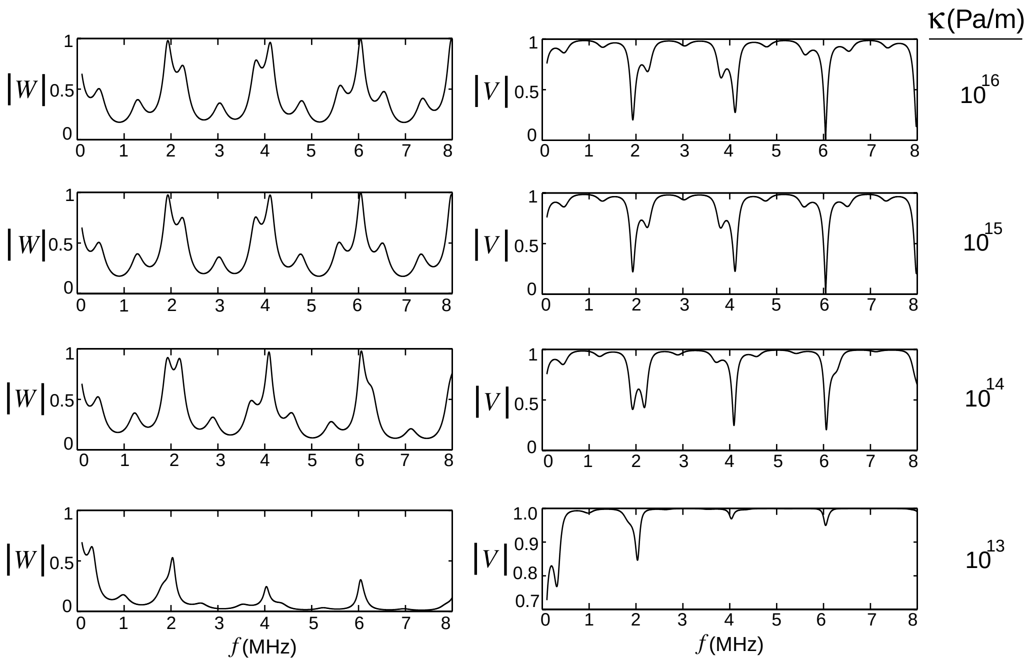

Figure 3.9: Magnitude of linear transmission and reflection coefficients for bonded 1/16 in. plates of aluminum and acrylic. Aluminum plate is closer to the source. Material constants are given in Table A.1.

Predictions for transmission and reflection through two bonded 2.36 mm acrylic plates are shown in Fig. 3.10. The characteristics of pass-band frequency shifting and reduction of transmission maxima at high frequencies are similar to Fig. 3.6. However, as discussed in Fig. 3.9, the pass bands are much weaker and more closely spaced in frequency for acrylic than for aluminum. Because acrylic has a lower specific acoustic impedance than aluminum or steel, reflection and transmission effects approach the limit of behaving like a single plate of thickness l at smaller values of κ. For example, for $f = 8$ MHz and $\kappa = 10^{15}$ Pa/m one obtains $\omega C/2g_{s1} \approx 0.08$, so the effect of the interface between the plates is small. The corresponding value of $\omega C/2g_{s1}$ for aluminum for $f = 8$ MHz and $\kappa = 10^{15}$ Pa/m is ≈ 0.4, so the effect of the compliant interface on the transmission and reflection is more pronounced.

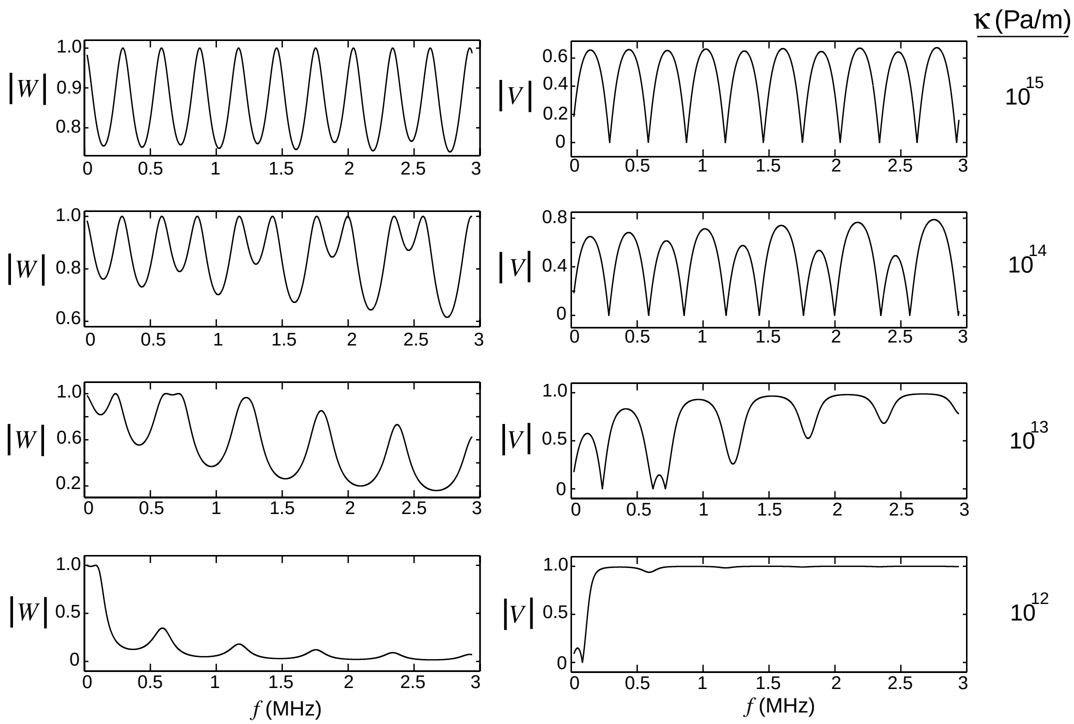

Figure 3.10: Magnitude of linear transmission and reflection coefficients for two bonded 2.36 mm acrylic plates. Material parameters for acrylic are given in Table A.1.

3.1.5 Field structure in bonded plates

In this section we consider the pressure (negative stress) and particle velocity in two 1/16 in. bonded aluminum plates which are immersed in water and insonified by a plane wave with amplitude P_i incident from the left. Examination of these quantities in the plate provides a better understanding of resonant behavior for the plates, and of stresses and strains at the bond. This perspective is relevant, for example, in experiments performed to determine when a bond is near failure.

Pressure and velocity amplitudes are determined by solving Eqn. (3.14) for A_1, B_1, A_2, and B_2, and substituting these expressions into Eqns. (3.1) and (3.2). The (normalized) pressure in the first plate is

$$\begin{aligned}\frac{P_1}{P_i} = \frac{2}{g_f g_{s1} g_{s2} \Delta}\Big\{ &- \left[j\omega C g_f^2 + g_f (g_{s2}^2 + g_{s1} g_{s2}) \right] j \cos(k_{s1}\gamma + k_{s2}h) \\ &+ \left[j\omega C g_f g_{s2} + g_f^2 (g_{s1} + g_{s2}) \right] \sin(k_{s1}\gamma + k_{s2}h) \\ &+ \left[j\omega C g_f^2 + g_f (g_{s2}^2 - g_{s1} g_{s2}) \right] j \cos(k_{s1}\gamma - k_{s2}h) \\ &+ \left[j\omega C g_f g_{s2} + g_f^2 (g_{s2} - g_{s1}) \right] \sin(k_{s1}\gamma - k_{s2}h) \Big\}, \end{aligned} \tag{3.32}$$

where $\gamma = d - x$, and Δ is given by Eqn. (3.19). The pressure in the second plate is

$$\frac{P_2}{P_i} = \frac{-4j}{\Delta} \left(j \frac{g_f}{g_{s2}} \sin k_{s2}\zeta + \cos k_{s2}\zeta \right), \tag{3.33}$$

where $\zeta = l - x$. The (normalized) particle velocity in the first plate is

$$\begin{aligned}\frac{U_1}{g_{s1} P_i} = \frac{2}{g_{s1} g_{s2} \Delta}\Big\{ &- [j\omega C g_{s2} + g_f (g_{s1} + g_{s2})] j \cos(k_{s1}\gamma + k_{s2}h) \\ &+ [j\omega C g_f + g_{s2} (g_{s1} + g_{s2})] \sin(k_{s1}\gamma + k_{s2}h) \\ &- [j\omega C g_{s2} + g_f (g_{s2} - g_{s1})] j \cos(k_{s1}\gamma - k_{s2}h) \\ &- [j\omega C g_f + g_{s2} (g_{s2} - g_{s1})] \sin(k_{s1}\gamma - k_{s2}h) \Big\}, \end{aligned} \tag{3.34}$$

and the particle velocity in the second plate is

$$\frac{U_2}{g_{s2} P_i} = \frac{-j}{\Delta} \left(\frac{g_f}{g_{s2}} \cos k_{s2}\zeta + j \sin k_{s2}\zeta \right). \tag{3.35}$$

We first examine the pressure amplitude at the compliant interface for varying stiffness and frequency. Pressure at the interface ($x = d$), normalized by the magnitude of the incident pressure, is shown in Fig. 3.11. The displacement discontinuity at $x = d$ is related to the pressure by the first-order relation $p(d, t)/\kappa = \xi_{d-} - \xi_{d+}$, Eqn. (3.6). Comparison of Fig. 3.11 with Fig. 3.6 shows that pressure at $x = d$ is a maximum at odd pass bands, and a minimum at even pass bands. Shifting of frequencies of pressure maxima occur as the stiffness at the interface decreases, corresponding to the resonance frequency shifts shown in Fig. 3.6. For $\kappa = 10^{15}$ Pa/m and $\kappa = 10^{14}$ Pa/m, we observe a decrease in pressure maxima as frequency is increased.

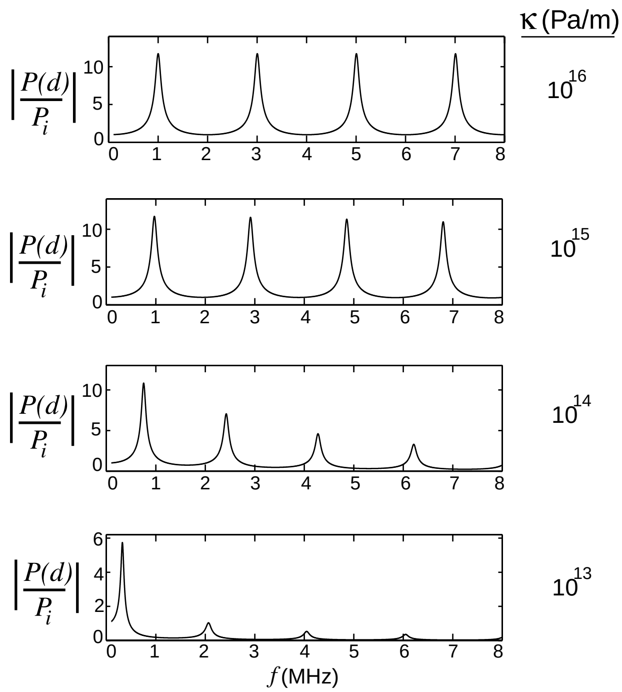

Figure 3.11: Normalized magnitudes of pressure amplitude at $x = d$ in two bonded 1/16 in. aluminum plates.

The magnitudes of the pressure and particle velocity amplitudes in two 1/16 in. aluminum plates are shown in Fig. 3.12. The magnitude of the pressure amplitude in the plate, $|P_{\rm pl}|$, is normalized by the magnitude of the incident pressure amplitude, $|P_i|$. Also, the magnitude of the particle velocity amplitude in the plate, $|U_{\rm pl}|$, is normalized by $|g_{s1}P_i|$. As the stiffness κ of the contact boundary decreases, the particle velocity discontinuity across the boundary increases. This particle velocity discontinuity is accompanied by a discontinuity in $\partial p/\partial x$ across the boundary, as dictated by the first-order momentum relation, Eqn. (2.3). The wave reflected from the contact boundary changes the pressure and particle velocity fields in the first layer, which in turn alters the resonance characteristics of the system.

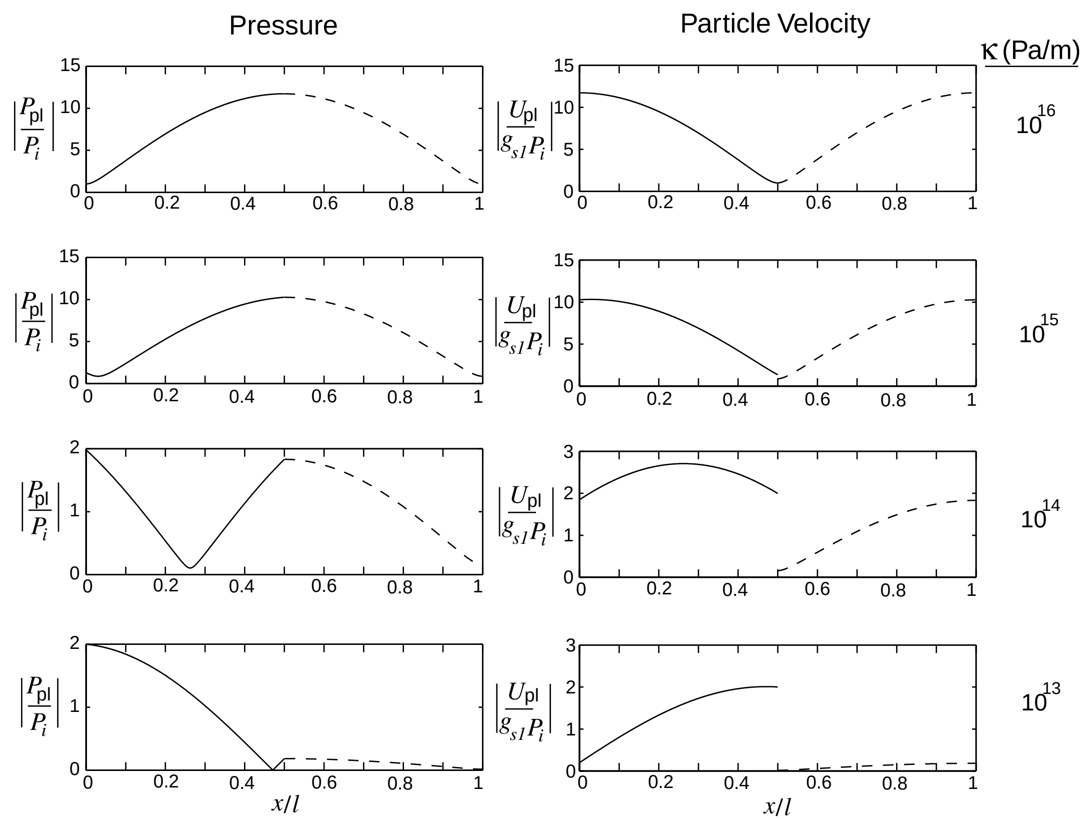

Figure 3.12: Normalized magnitudes of pressure and particle velocity amplitudes in two bonded 1/16 in. aluminum plates, $f = 1$ MHz.

Pressure and particle velocity in the plates are shown for five frequencies in Fig. 3.13. The stiffness of the bond is $\kappa = 10^{14}$ Pa/m. As shown in Fig. 3.6, transmission maxima occur near $f = 0.75, 2.0$, and 2.4 MHz, and transmission is small for $f = 1.3$ MHz. As shown in Fig. 3.11, the magnitude of $P(d)$ is near a minimum at $f = 1.7$ MHz. At transmission maxima, pressure and velocity are nearly symmetric about the interface at $x = d$. In contrast, when transmission is small the pressure and velocity are asymmetric about the interface. At $f =$ 2 MHz the magnitude of the pressure is small at $x = d$, so the displacement discontinuity across the interface is small and the pressure in the plate is almost the same as the pressure in a plate of thickness $2d$ with no compliant boundary (as seen in Fig. 2.4 for $\lambda_2 = l$, where λ_2 is the wavelength at the second pass band).

A few notable characteristics of pressure and velocity in the bonded plates are shown in this section. First, the bond is only excited significantly at every other transmission maximum (corresponding to $\lambda_n = 4d/n$, $n = 1, 3, 5, \ldots$, for $\kappa \to \infty$). Moreover, as the bond stiffness decreases, the displacement (and particle velocity) discontinuity across the bond increases, but the maximum pressure that can be applied to the bond decreases. This occurs because, as the bond stiffness decreases, the interface approahes a free boundary and the incident wave is partially reflected. This partial reflection in turn affects the resonant behavior of the plates.

3.2 Nonlinear Theory

In this section we determine the expressions for the second harmonic radiated into the fluid due to the presence of a planar nonlinear interface at $x = d$. In Chap. 2, second harmonic was generated cumulatively within a homogeneous plate. In this section, all the second harmonic is assumed to be produced at the nonlinear spring interface. In our analysis we first determine the pressure amplitude of the second harmonic at the planar nonlinear interface. Then we determine the amplitude of the second harmonic radiated into the fluid.

3.2.1 Planar nonlinear interface

We model the planar nonlinear interface as a homogeneous distribution of nonlinear springs at $x = d$, described to second order by[30]

$$p(d) = \kappa[\xi(d_-) - \xi(d_+)] + \frac{\mu}{2}[\xi(d_-) - \xi(d_+)]^2 \,, \tag{3.36}$$

where $\xi(d_-)$ and $\xi(d_+)$ are particle displacements on either side of the interface, κ is a linear spring constant, and μ is a parameter of nonlinearity for the spring.

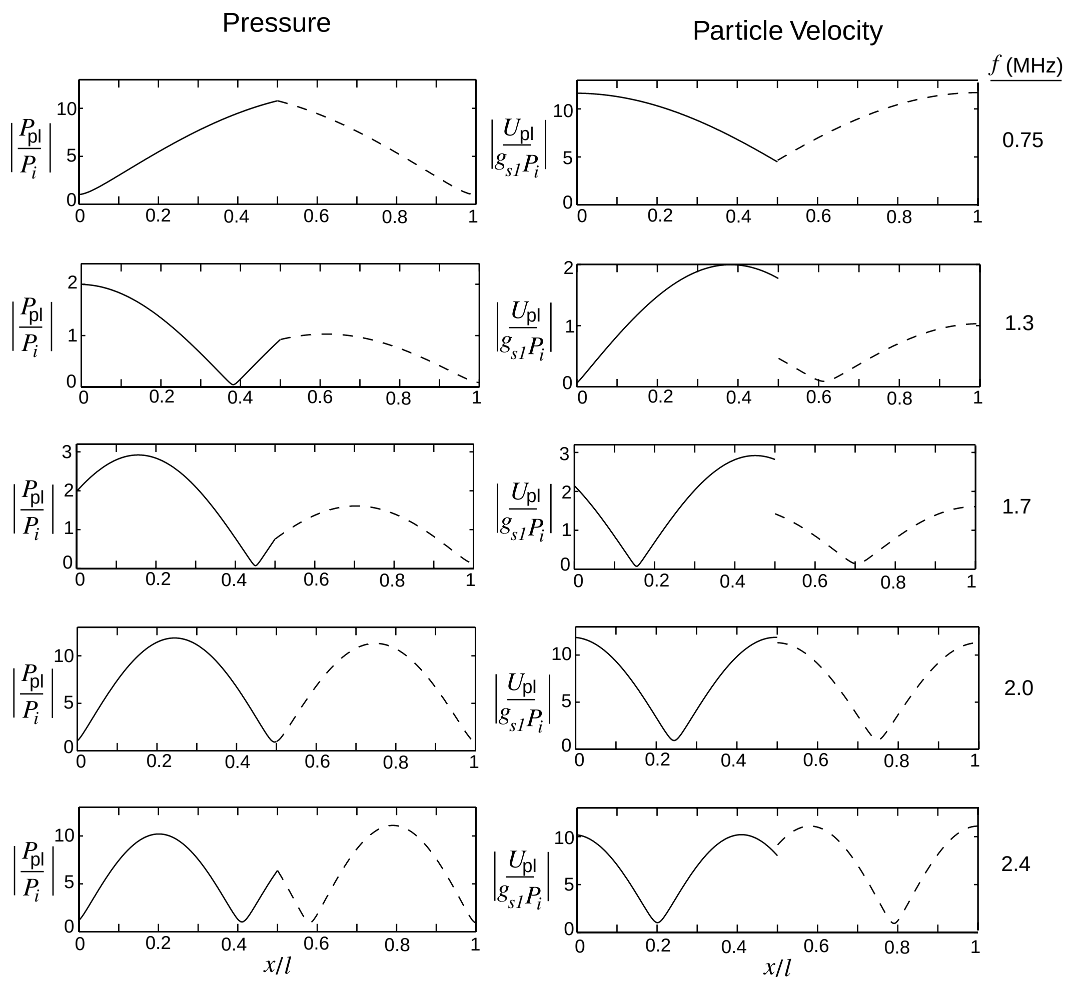

Figure 3.13: Normalized magnitudes of pressure and particle velocity amplitudes in two 1/16 in. aluminum plates, $\kappa = 10^{14}$ Pa/m.

In their investigation, Rudenko and Vu[30] used this equation to describe a planar contact interface populated by infinitesimal springs with a random distribution of spring lengths. By averaging over this population of springs, the authors obtained an equation in the form of Eqn. (3.36). In general, Eqn. (3.36) models any interface that behaves like a spring with quadratic nonlinearity, such as the bonded interface explored by Achenbach, et al.[35] (Note that classical models of nonlinearity in springs focus on cubic, rather than quadratic, nonlinearity to account for the hardening behavior associated with a single spring. However, the ensemble average over many springs of different lengths yields quadratic nonlinearity at leading order.)

To first order, we may substitute Eqn. (3.6) into the second term on the right-hand side of Eqn. (3.36) and still be correct to second order. With this substitution made, by differentiating Eqn. (3.36) with respect to time we recast Eqn. (3.36) into the form

$$\left.\frac{\partial p}{\partial t}\right|_{x=d} = \kappa[u(d_-) - u(d_+)] + \frac{\mu}{2\kappa^2}\left.\frac{\partial p^2}{\partial t}\right|_{x=d} . \tag{3.37}$$

It is easier in our analysis to work with Eqn. (3.37) than Eqn. (3.36), because Eqn. (3.37) is written in terms of pressure and particle velocity.

3.2.2 General expression for second harmonic radiated into the fluid

As in Chap. 2, we begin our analysis of the second harmonic generated at the interface between the plates by applying the method of successive approximations to the expressions for pressure and particle velocity. We expand the acoustic pressure p and particle velocity u as first-order quantities plus small second-order perturbations,

$$p = p^{(1)} + p^{(2)} , \quad u = u^{(1)} + u^{(2)} , \tag{3.38}$$

where $|p^{(2)}| \ll |p^{(1)}|$ and $|u^{(2)}| \ll |u^{(1)}|$. We apply Eqn. (3.38) to Eqn. (3.37) to obtain

$$\left.\frac{\partial p^{(1)}}{\partial t}\right|_{x=d} - \kappa[u^{(1)}(d_-) - u^{(1)}(d_+)] = 0, \tag{3.39}$$

$$\left.\frac{\partial p^{(2)}}{\partial t}\right|_{x=d} - \kappa[u^{(2)}(d_-) - u^{(2)}(d_+)] = \left.\frac{\mu}{2\kappa^2}\frac{\partial (p^{(1)})^2}{\partial t}\right|_{x=d} . \tag{3.40}$$

Equation (3.40) is equivalent to Eqn. (3.7), and all first-order phenomena associated with this term are described in Sec. 3.1. In Eqn. (3.40), the right-hand side represents a driving term related to $p^{(1)}$, which generates the second-order pressure $p^{(2)}$ at $x = d$.

It is convenient to work with pressure amplitudes, assuming first-order pressures have frequency ω and second-order pressures have frequency 2ω. All pressure amplitudes corresponding to frequency 2ω have the subscript s, denoting that it is a second-harmonic amplitude. We define the first-order pressure amplitude at $x = d$, $P(d)$, as

$$p(d, t) = \frac{P(d)}{2} e^{j\omega t} + \text{c.c.} , \tag{3.41}$$

where

$$P(d) = A_1 e^{-jk_{s1}d} + B_1 e^{jk_{s1}d} = A_2 + B_2 , \tag{3.42}$$

and A_2 and B_2 are the first-order pressure amplitudes in the second plate [see Eqn. (3.1)]. The amplitudes A_2 and B_2 may be determined by solving Eqn. (3.14). Substituting the resulting expressions A_2 and B_2 into Eqn. (3.42) gives

$$P(d) = \frac{4P_i}{\Delta}\left(\frac{g_f}{g_{s2}} \sin k_{s2}h - j \cos k_{s2}h\right) , \tag{3.43}$$

where Δ is expressed in Eqn. (3.19). Substituting Eqn. (3.41) into Eqn. (3.40) yields

$$\frac{\partial p^{(2)}}{\partial t} = \kappa[u^{(2)}(d_-) - u^{(2)}(d_+)] + \frac{j\omega\mu P^2(d)}{4\kappa^2} e^{(j2\omega t)} + \text{c.c.} , \tag{3.44}$$

where $P(d)$ is the first-order pressure amplitude at $x = d$. [Although the square of Eqn. (3.41) also contains d.c. terms, in our analysis we consider only terms that contribute to the generation of second harmonic.]

Figure 3.14 shows the pressure amplitudes and directions of the plane waves with frequency 2ω in, and radiated from, the plates. We wish to determine the

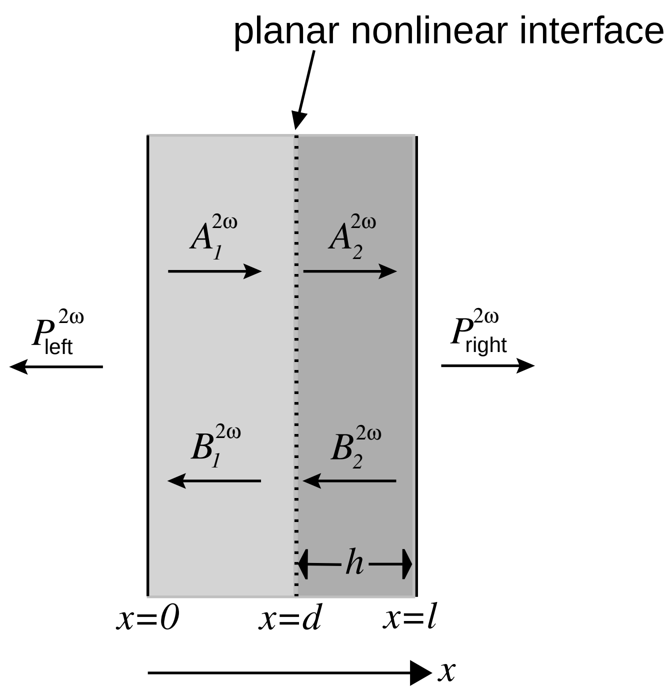

Figure 3.14: Plane waves in the plates at the second harmonic.

amplitudes of the pressure at the second harmonic radiated into the fluid in either direction, $P^{2\omega}_{\text{left}}$ and $P^{2\omega}_{\text{right}}$. We express the second-order pressure field shown in Fig. 3.14 as

$$p^{(2)} = \frac{1}{2}\begin{cases} P^{2\omega}_{\text{left}} e^{j2(\omega t + k_f x)} + \text{c.c.}\,, & x < 0\,, \\ A^{2\omega}_1 e^{j2(\omega t - k_{s1} x)} + B^{2\omega}_1 e^{j2(\omega t + k_{s1} x)} + \text{c.c.}\,, & 0 \le x \le d\,, \\ A^{2\omega}_2 e^{j2[\omega t - k_{s2}(x-d)]} + B^{2\omega}_2 e^{j2[\omega t + k_{s2}(x-d)]} + \text{c.c.}\,, & d \le x \le l\,, \\ P^{2\omega}_{\text{right}} e^{j2[\omega t - k_f (x-l)]} + \text{c.c.}\,, & x > l\,, \end{cases} \tag{3.45}$$

where the superscript 2ω denotes a wave amplitude of a second-harmonic component. The corresponding particle velocity, determined by applying the linearized one-dimensional momentum equation to Eqn. (3.45), is

$$u^{(2)} = \frac{1}{2}\begin{cases} -g_f P^{2\omega}_{\text{left}} e^{j2(\omega t + k_f x)} + \text{c.c.}\,, & x < 0\,, \\ g_{s1}\left(A^{2\omega}_1 e^{j2(\omega t - k_{s1} x)} - B^{2\omega}_1 e^{j2(\omega t + k_{s1} x)}\right) + \text{c.c.}\,, & 0 \le x \le d\,, \\ g_2\left(A^{2\omega}_2 e^{j2[\omega t - k_{s2}(x-d)]} - B^{2\omega}_2 e^{j2[\omega t + k_{s2}(x-d)]}\right) + \text{c.c.}\,, & d \le x \le l\,, \\ g_f P^{2\omega}_{\text{right}} e^{j2[\omega t - k_f (x-l)]} + \text{c.c.}\,, & x > l\,. \end{cases} \tag{3.46}$$

By equating pressure and particle velocity in Eqns. (3.45) and (3.46) across boundaries at $x = 0$ and $x = l$, we have four equations for $P^{2\omega}_{\text{left}}, P^{2\omega}_{\text{right}}, A^{2\omega}_{1,2}$, and $B^{2\omega}_{1,2}$. Boundary conditions at $x = d$ provide us with two additional equations,

$$A^{2\omega}_1 e^{-j2k_{s1}d} + B^{2\omega}_1 e^{j2k_{s1}d} = A^{2\omega}_2 + B^{2\omega}_2\,, \tag{3.47}$$

$$\begin{aligned} j4\omega C(A^{2\omega}_2 + B^{2\omega}_2) &= 2g_{s1}(A^{2\omega}_1 e^{-j2k_{s1}d} - B^{2\omega}_1 e^{j2k_{s1}d}) \\ &\quad - 2g_{s2}(A^{2\omega}_2 - B^{2\omega}_2) + j\omega\mu C^3 P^2(d)\,. \end{aligned} \tag{3.48}$$

These six equations reduce to the following form after elimination of $P^{2\omega}_{\text{left}}$ and $P^{2\omega}_{\text{right}}$:

$$\begin{pmatrix} 1+\frac{g_{s1}}{g_f} & 1-\frac{g_{s1}}{g_f} & 0 & 0 \\ e^{-jk_{s1}d} & e^{jk_{s1}d} & -1 & -1 \\ -\frac{g_{s1}}{g_f}e^{-jk_{s1}d} & \frac{g_{s1}}{g_f}e^{jk_{s1}d} & \frac{2j\omega C+g_{s2}}{g_f} & \frac{2j\omega C-g_{s2}}{g_f} \\ 0 & 0 & (1-\frac{g_{s2}}{g_f})e^{-jk_{s2}h} & (1+\frac{g_{s2}}{g_f})e^{jk_{s2}h} \end{pmatrix} \begin{pmatrix} A^{2\omega}_1 \\ B^{2\omega}_1 \\ A^{2\omega}_2 \\ B^{2\omega}_2 \end{pmatrix} = \begin{pmatrix} 0 \\ 0 \\ P^{2\omega}_{\text{spring}} \\ 0 \end{pmatrix}, \tag{3.49}$$

with which we determine $A_1^{2\omega}$, $B_1^{2\omega}$, $A_2^{2\omega}$, and $B_2^{2\omega}$. In Eqn. (3.49) we define

$$P_{\text{spring}}^{2\omega} \equiv \frac{j\omega\mu C^3 P_i^2}{2g_f} \,. \tag{3.50}$$

The amplitudes $P_{\text{left}}^{2\omega}$ and $P_{\text{right}}^{2\omega}$ may be expressed in terms of $A_1^{2\omega}$, $B_1^{2\omega}$, $A_2^{2\omega}$, and $B_2^{2\omega}$ by using Eqn. (3.45), and setting pressures equal across interfaces at $x = 0$ and $x = l$. The expressions for $P_{\text{left}}^{2\omega}$ and $P_{\text{right}}^{2\omega}$ are

$$P_{\text{left}}^{2\omega} = \frac{-2jP_{\text{spring}}^{2\omega}}{\Delta^{2\omega}} \left(\cos 2k_{s2}h + j\frac{g_f}{g_{s2}} \sin 2k_{s2}h \right) \,, \tag{3.51}$$

and

$$P_{\text{right}}^{2\omega} = \frac{-2jP_{\text{spring}}^{2\omega}}{\Delta^{2\omega}} \left(\cos 2k_{s1}d + j\frac{g_f}{g_{s1}} \sin 2k_{s1}d \right) \,, \tag{3.52}$$

where

$$\begin{aligned} \Delta^{2\omega} = \frac{1}{g_f g_{s1} g_{s2}} \Big\{ & \Big[2j\omega C g_f + (g_f^2 + g_{s1}g_{s2}) \Big] (g_{s1} + g_{s2}) \sin(2k_{s1}d + 2k_{s2}h) \\ & - \Big[2j\omega C (g_f^2 + g_{s1}g_{s2}) + g_f (g_{s1} + g_{s2})^2 \Big] j \cos(2k_{s1}d + 2k_{s2}h) \\ & + \Big[2j\omega C g_f + (g_f^2 - g_{s1}g_{s2}) \Big] (g_{s2} - g_{s1}) \sin(2k_{s1}d - 2k_{s2}h) \\ & + \Big[2j\omega C (g_f^2 - g_{s1}g_{s2}) + g_f (g_{s1} - g_{s2})^2 \Big] j \cos(2k_{s1}d - 2k_{s2}h) \Big\} \,. \end{aligned} \tag{3.53}$$

3.2.3 Simplified expression for equal plate thicknesses and impedances

As in Sec. 3.1.3, we seek simplified expressions for $P_{\text{left}}^{2\omega}$ and $P_{\text{right}}^{2\omega}$ in the case where the two plates are of the same material and thickness. We again set $\rho_{s1} = \rho_{s2}$, $c_{s1} = c_{s2}$, and $d = h = l/2$, so $k_{s1} = k_{s2}$ and $g_{s1} = g_{s2}$. Equations (3.43), (3.52), and (3.53) reduce to

$$P(d) = \frac{P_i}{\Delta} \left(\cos k_{s1}d + j\frac{g_f}{g_{s1}} \sin k_{s1}d \right) \,, \tag{3.54}$$

and

$$P_{\text{right}}^{2\omega} = \omega\mu \frac{C^3 P^2(d)}{g_f \Delta^{2\omega}} \left(\cos 2k_{s1}d + j\frac{g_f}{g_{s1}} \sin 2k_{s1}d \right) \,, \tag{3.55}$$

where

$$\Delta^{2\omega} = \frac{-4j\omega C}{g_{s1}}\left[\frac{j}{2}\left(\frac{g_f}{g_{s1}} + \frac{g_{s1}}{g_f}\right)\cos 4k_{s1}d - \sin 4k_{s1}d + \frac{j}{2}\left(\frac{g_{s1}}{g_f} - \frac{g_f}{g_{s1}}\right)\right]$$
$$- 4j\cos 4k_{s1}d + 2\left(\frac{g_f}{g_{s1}} + \frac{g_{s1}}{g_f}\right)\sin 4k_{s1}d\,. \tag{3.56}$$

The function Δ in Eqn. (3.54) is the expression given by Eqn. (3.28) because it corresponds to the pressure at the fundamental frequency. On the other hand, $\Delta^{2\omega}$ in Eqns. (3.55) and (3.56) corresponds to the second harmonic. Because the two plates are of the same material and thickness, $P_{\text{left}}^{2\omega} = P_{\text{right}}^{2\omega}$ for this case.

3.2.4 Theoretical predictions for radiated second harmonic

Figure 3.15 shows the predicted second harmonic radiation from two bonded 1/16 in. aluminum plates as a function of source frequency f. The plates are immersed in water. From Eqn. (3.55) we choose to normalize the second-order pressure amplitudes $P_{\text{left}}^{2\omega}$ and $P_{\text{right}}^{2\omega}$ by P_{norm}, which we define as

$$P_{\text{norm}} \equiv \frac{\omega\mu P_i^2}{\kappa^3 g_f}\,. \tag{3.57}$$

Although only $P_{\text{left}}^{2\omega}$ is shown, the radiation to the left (negative direction) is the same as the radiation to the right (positive direction). The system is an effective radiator of second harmonic only over narrow frequency bands corresponding to every other pass band at the fundamental. The reason that second harmonic generation is strong only at every other pass band is because there is a pressure node at $x = l/2$ for pass-band frequencies where $\lambda_n^{\text{pass}} = 2l/n$ where n is an even integer, and a pressure maximum for pass-band frequencies where $\lambda_n^{\text{pass}} = 2l/n$ where n is an odd integer, as shown in Fig. 2.4. [The pressure amplitude $P(d)$ is shown in Fig. 3.12.] Equation (3.55) shows that the second harmonic generated is proportional to $P^2(d)$, where in this instance $d = l/2$, so there will be relatively little second harmonic generation if $|P(d)|$ is small.

For $\kappa \to 10^{14}$ Pa/m the normalized radiation begins to decrease, starting at higher frequencies. This behavior occurs because, for small values of κ, the interface approaches a free surface, at which the pressure must vanish. According to Eqn. (3.55), as the first-order pressure at the interface vanishes, so does the radiated pressure at the second harmonic. The frequencies at which second harmonic is strongly radiated shift as κ decreases, corresponding to the shifting of transmission maxima in Fig. 3.6. However, the magnitude of the radiated second harmonic drops as the pass bands merge together.

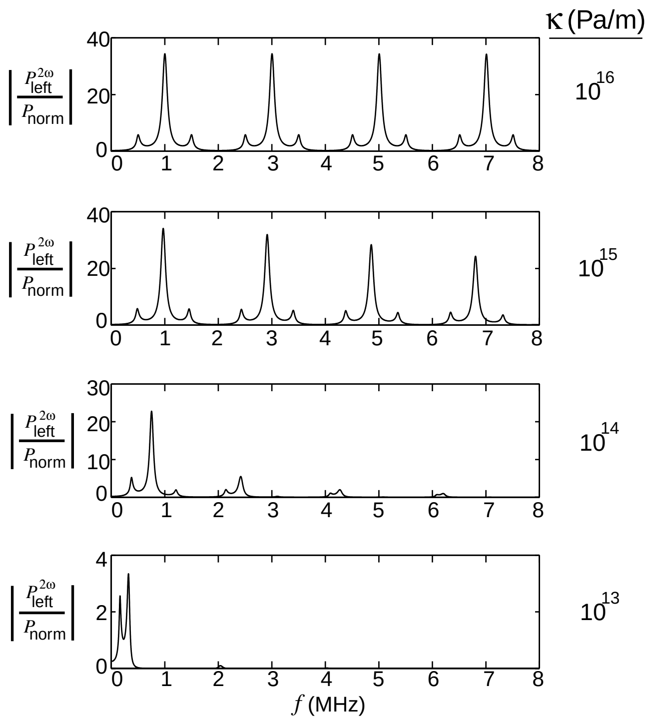

Figure 3.15: Theory for radiated second harmonic from two bonded 1/16 in. aluminum plates as a function of the fundamental frequency f. Radiation is the same to the left and to the right.

Figure 3.16 shows the radiation of second harmonic to the left and right, given by Eqns. (3.51) and (3.52), for two aluminum plates with different thicknesses, $d = 1/32$ in. and $h = 3/32$ in. The 1/32 in. thick plate is closer to the source. Although the defect is located one quarter of the way through the plate, the

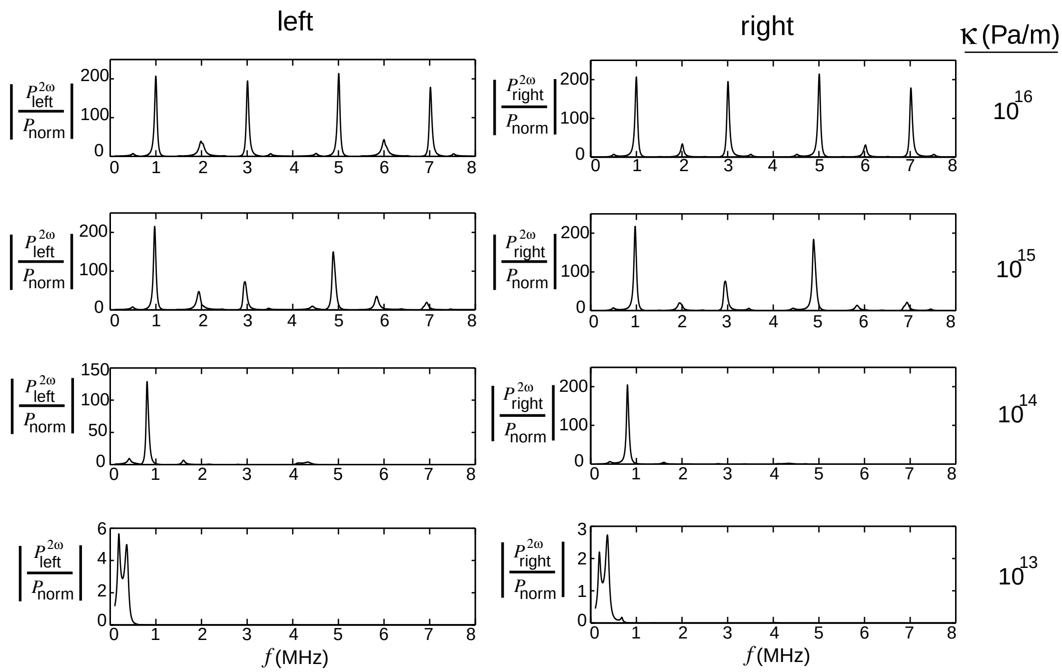

Figure 3.16: Second harmonic radiated to the left and to the right for bonded aluminum plates, $d = 1/32$ in. and $h = 3/32$ in. as a function of the fundamental frequency f.

frequencies at which the second harmonic is radiated (1, 3, 5, and 7 MHz) are the same as in Fig. 3.15. The second harmonic radiation is stronger for large interface stiffnesses than for the case in which $d = h = 1/16$ in. shown in Fig. 3.15. In contrast to Fig. 3.15, there is also some harmonic radiated at 2 and 6 MHz. However, no second harmonic is radiated at 4 MHz, because the first-order pressure at $x = 1/32$ in. for the resonance near $f = 4$ MHz is zero. As κ decreases, the radiation at higher frequencies diminishes. Comparison between plots on the left and right in Fig. 3.16 reveals that the radiation in the negative and positive directions is nearly identical for $\kappa = 10^{16}$ Pa/m, but differs substantially as κ decreases. For $\kappa = 10^{14}$ Pa/m the radiation in the positive direction is stronger, but for $\kappa = 10^{13}$ Pa/m the radiation in the negative direction is stronger.

In Fig. 3.17 the plates are reversed, so $d = 3/32$ in. and $h = 1/32$ in. (thicker plate now on the left). In contrast to the linear reflection and transmission coefficients, whose magnitudes are unchanged when the plates are reversed, the radiated second harmonic depends on the relative positions of the plates. Differences between Figs. 3.16 and 3.17 are most prominent for $\kappa = 10^{13}$ Pa/m and $\kappa = 10^{14}$ Pa/m, for which the harmonic radiated is much stronger when the 1/32 in. plate is closer to the source than the 3/32 in. plate.

The reason why the second harmonic radiated from the plate depends on the orientation of the plates, while the linear reflection and transmission coefficients are unchanged, is as follows. The second harmonic radiated from the plate depends on the pressure at $x = d$. While the linear reflection and transmission coefficients are unchanged when the orientation of the plates is reversed, the pressure and particle velocity field in the plates themselves is affected by the reversal. Hence $p(d)$, and thus the radiated second harmonic, also depends on the orientation of the plates.

Figure 3.18 shows results for a 1/16 in. aluminum plate in contact with a 1/16 in. steel plate. The aluminum plate faces the source. For $\kappa = 10^{16}$ Pa/m, strong second harmonic generation to the left and right occurs near $1, 3, 5, \ldots$ MHz, which corresponds to the small ($|W| \approx 0.6$) pass bands in Fig. 3.8. For $\kappa = 10^{15}$ Pa/m the radiation becomes irregular, and below $\kappa = 10^{15}$ Pa/m it drops

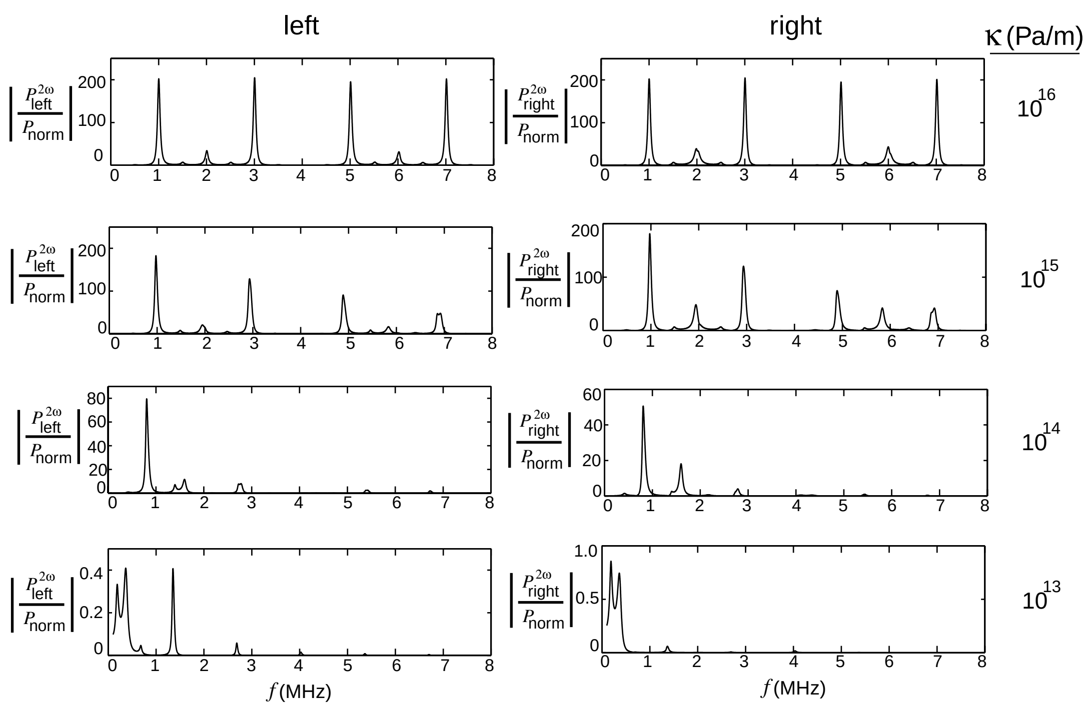

Figure 3.17: Second harmonic radiated to the left and to the right for bonded aluminum plates, for $d = 3/32$ in. and $h = 1/32$ in., as a function of the fundamental frequency f.

quickly.

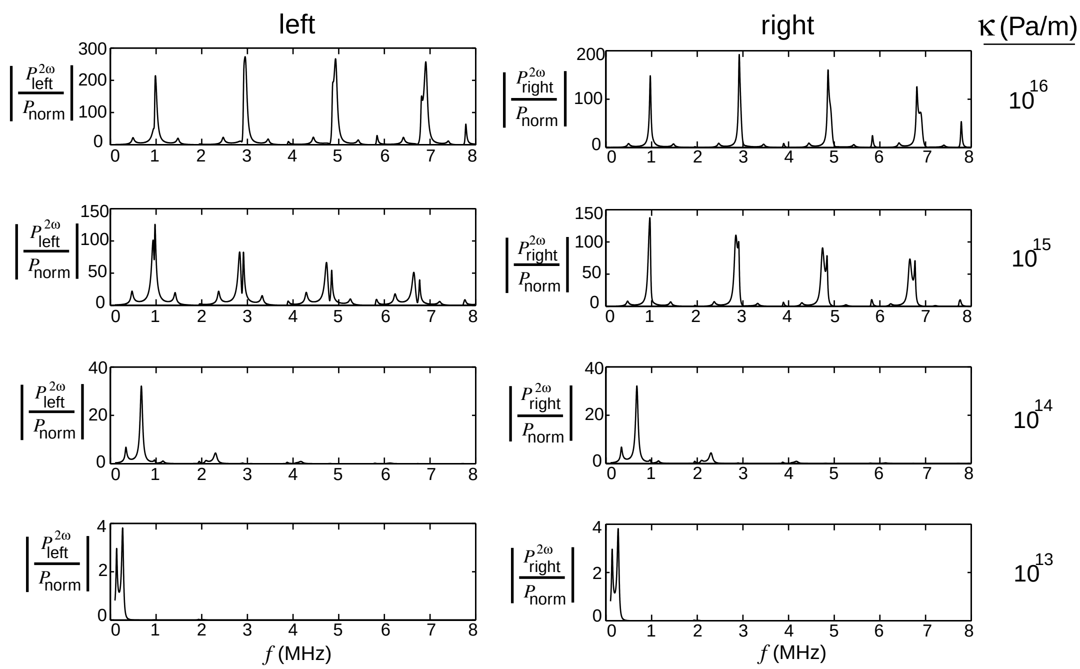

Figure 3.18: Second harmonic radiated to the left and to the right from two bonded plates, one of aluminum and the other of steel, as a function of the fundamental frequency f. Both plates are 1/16 in. thick, and the aluminum plate is closer to the source.

The reverse situation, in which the steel plate is closer to the source, is shown in Fig. 3.19. The second harmonic radiated from the plate is much smaller when the steel plate faces the source than when the aluminum plate faces the source.

Figure 3.20 shows the second harmonic radiated from a 1/16 in. aluminum plate in contact with a 1/16 in. acrylic plate. The aluminum plate is closer to the source. The strongest second harmonic radiation to the left occurs at 2 and 4 MHz, which correspond to resonances in the aluminum plate. Radiation to the right is more irregular than radiation to the left, although the strongest radiation

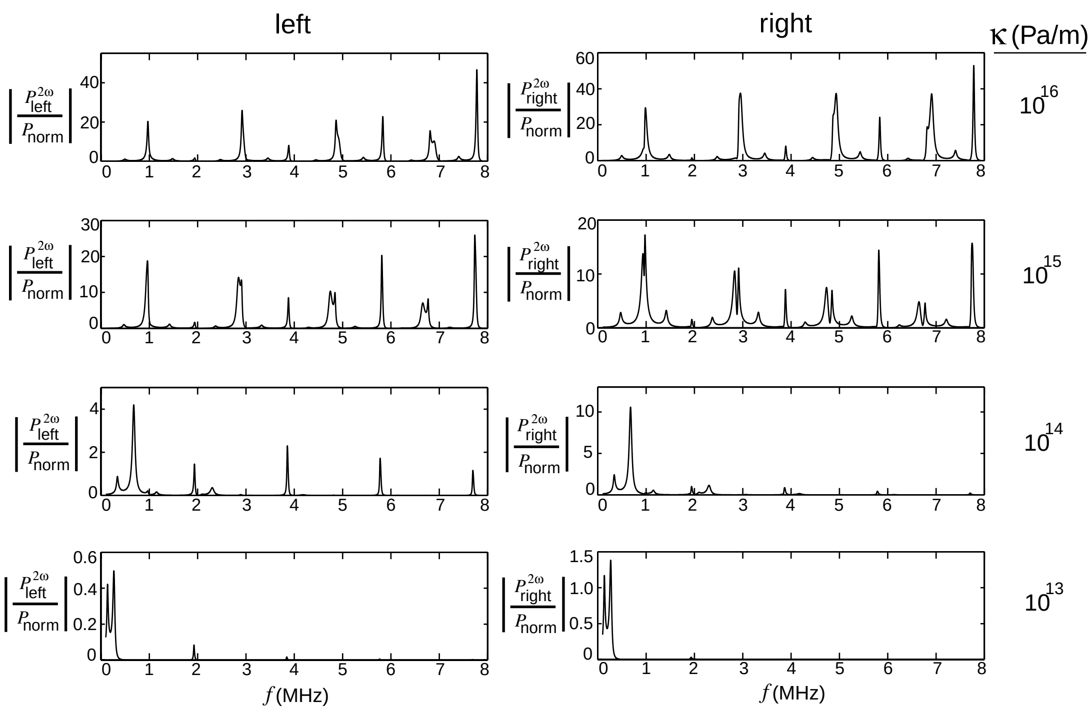

Figure 3.19: Second harmonic radiated to the left and right from bonded 1/16 in. steel and aluminum plates as a function of the fundamental frequency f. The steel plate is closer to the source.

still occurs near 2 and 4 MHz. The reverse situation, in which the acrylic plate is closer to the source, is shown in Fig. 3.21. Radiation is stronger both to the left and right than in Fig. 3.20. Although frequencies of strong radiation are not evenly spaced, there are many more than in Fig. 3.20. This corresponds to the resonances of a 1/16 in. acrylic plate.

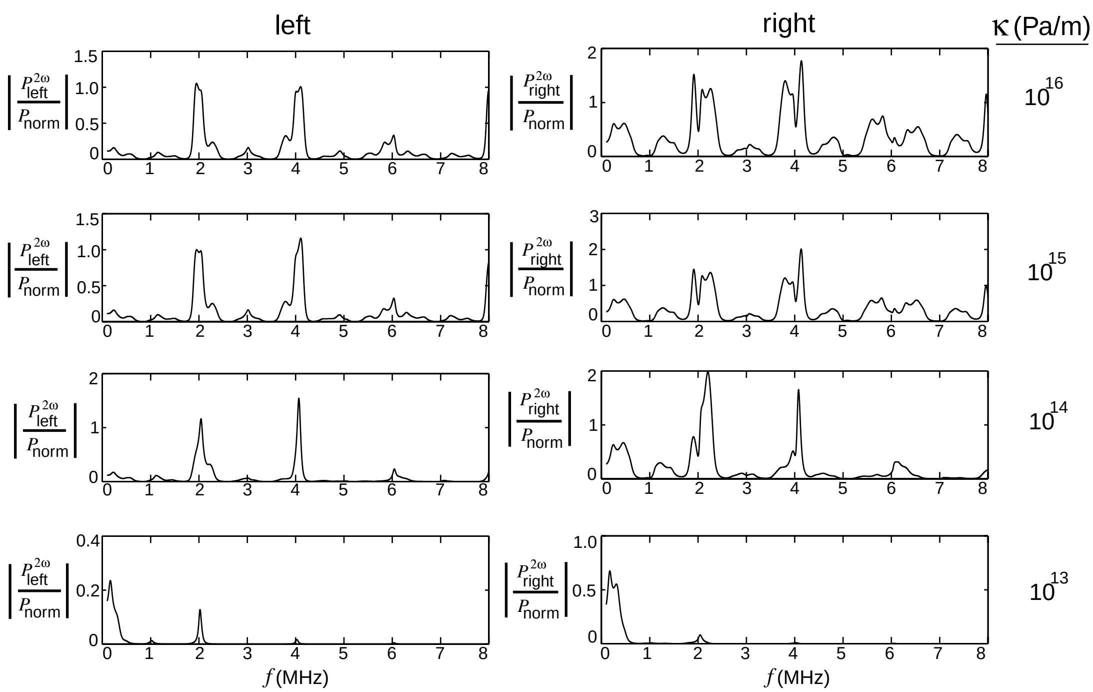

Figure 3.20: Second harmonic radiated to the left and to the right from two bonded plates, one of aluminum and the the other of acrylic, as a function of the fundamental frequency f. Both plates are 1/16 in. thick, and the aluminum plate is closer to the source.

Figure 3.22 shows the predicted second harmonic radiated from two 2.36 mm acrylic plates. Although $P_{\mathrm{left}}^{2\omega}$ is shown, the radiation is the same propagating in the negative and positive directions. Because the quality factor of resonance phenomena in acrylic plates is lower than in aluminum plates (compare Fig. 3.10 with Fig. 3.6), the magnitude of the second harmonic is much lower than for

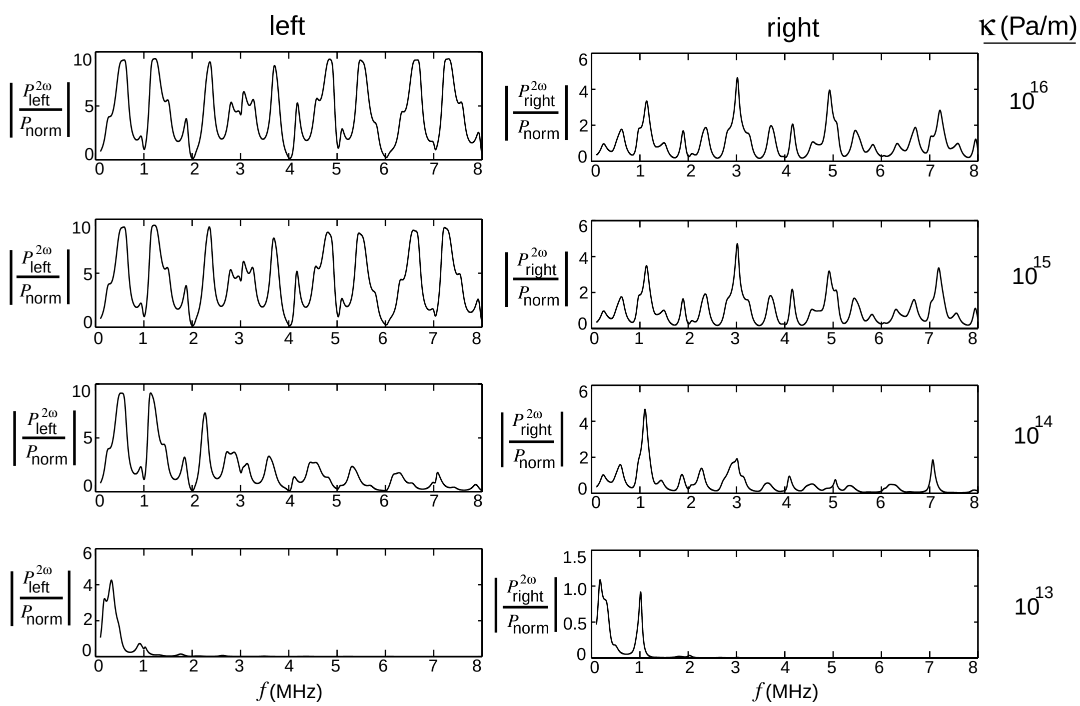

Figure 3.21: Second harmonic radiated to the left and right from bonded 1/16 in. acrylic and aluminum plates as a function of the fundamental frequency f. The acrylic plate is closer to the source.

aluminum, and it is radiated over much broader frequency bands. Also for this reason, there are no sharp peaks in the magnitude of the radiated second harmonic, as there are for aluminum (Fig. 3.15). However, radiation maxima still occur at every other pass-band frequency.

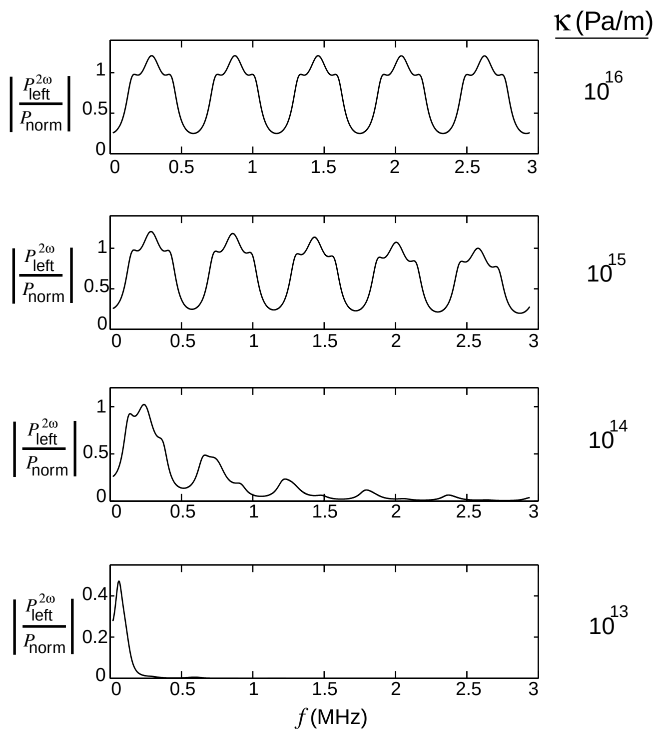

Figure 3.22: Second harmonic radiated from two bonded 2.36 mm acrylic plates as a function of the fundamental frequency f. Radiation is the same to the left and to the right.

3.3 Experimental Results

In this section we present the results of reflection and transmission experiments that correspond to the theory developed in Secs. 3.1 and 3.2. Plates of acrylic and aluminum were used. Epoxy was used to bond the plates together, and the bond was prepared so that its quality varied predictably from one side of the plate to the other. The impedance ratio between acrylic and water is approximately 2 so, as evidenced by Fig. 3.10, we do not expect strong resonances. However, acrylic is transparent, and the bond can be observed directly. (Glass has a larger impedance than acrylic, but because it is brittle it is impractical to use when preparing a sample with a broken bond.) The impedance ratio between aluminum and water is approximately 12, and therefore the resonance effects are pronounced.

Although the theory presented in the previous two sections is for plane waves, in our experiments we used sound beams, which exhibit diffraction. As discussed in Chap. 4, the diffracting sound beams can be represented as a continuum of plane waves propagating in different directions. The experimental conditions therefore do not correspond to a plane wave incident upon a plate at normal incidence, but rather a continuum of plane waves that are incident upon a plate at different angles of incidence. One consequence of this interpretation is that one can easily identify Lamb modes excited in the plate. Another consequence is that resonances in the transmission and reflection coefficients, which are sensitive to angle of incidence, are weaker than predicted by the theory in Secs. 3.1 and 3.2.

Another effect of diffraction in a real sound beam is that the pressure amplitude along the beam axis changes as a function of distance from the source. An example is shown in Fig. 3.23. Axial distance x is normalized by the Rayleigh distance $x_0 = ka^2/2$. For this example, the source is a 1 in. diameter plane piston (radius $a = 0.5$ in.) with an effective source pressure p_0 and frequency 2 MHz. However, the normalized axial pressure is not significantly different for $x/x_0 \gtrsim 1/3$ for different source frequencies and source radii, as long as $a/\lambda \gg 1$. Rapid spatial variations occur in the nearfield of the sound beam ($x/x_0 \lesssim 1/3$). The advantage of taking measurements using this part of the sound beam is that the cumulative generation of harmonics in the fluid is not significant. The disadvantage is that the rapid oscillations make it more difficult to accurately compare measurements made at these distances with theory. For ($x/x_0 \gtrsim 1/3$) changes in the sound beam are not as rapid. However, the harmonics generated in the sound beam are stronger.

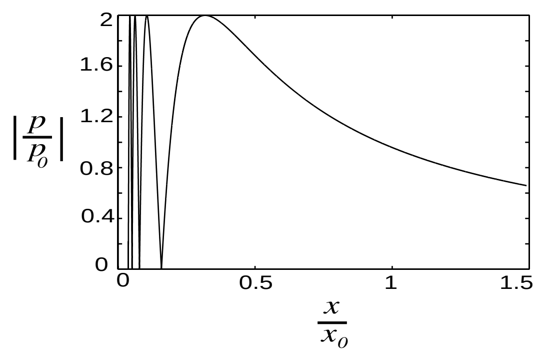

Figure 3.23: Pressure on the axis of a sound beam generated by a 1 in. diameter, 2 MHz plane piston.

3.3.1 Experimental arrangement

The configuration for the reflection experiments is shown in Fig. 3.24. A sound beam is normally incident upon the sample, with the membrane hydrophone positioned between the source and the sample. The distance between the source and the hydrophone is x_s. The distance between the plate and hydrophone is x_r.

The samples are prepared as follows: two plates are joined using a commonly available, quick-setting epoxy. After letting the bond set for approximately 15 minutes, the plates are pulled apart on one side and then pressed back together. The result is illustrated in Fig. 3.25. On one side of the plate the bond is good, and on the other side the bond is broken. In the middle of the plate the bond is weakened. By translating the source and receiver from one side of the plate to the other, portions of the sample with different bond qualities can be investigated.

3.3.2 Two bonded acrylic plates

Figure 3.26 shows measurements of the reflection from two acrylic plates, with $x_s = 4$ cm and $x_r = 1.5$ cm. The source is a 1 in. diameter, 1 MHz piezoelectric plane piston transducer. Received pressures in the graphs are normalized by the source pressure, $p_0 = 230$ kPa. Magnitudes of the pressure amplitudes at the fundamental, second, and third harmonic frequencies are displayed. Pressure is

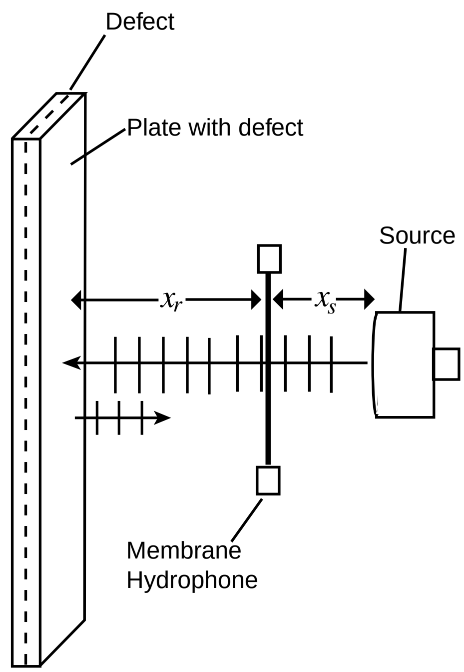

Figure 3.24: Geometry for the reflection experiment.

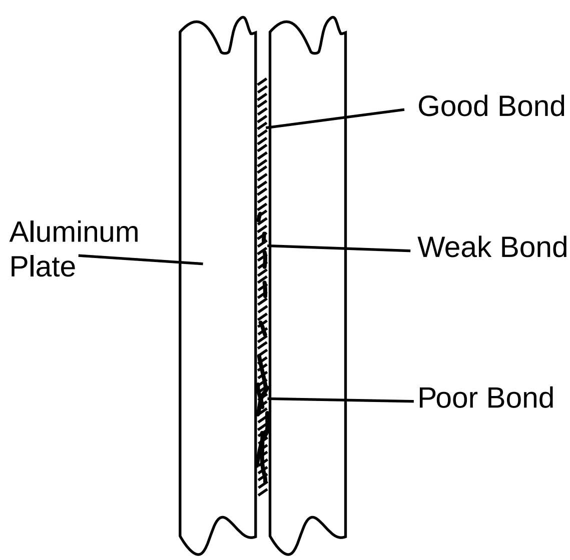

Figure 3.25: Two plates joined with bond of varying quality.

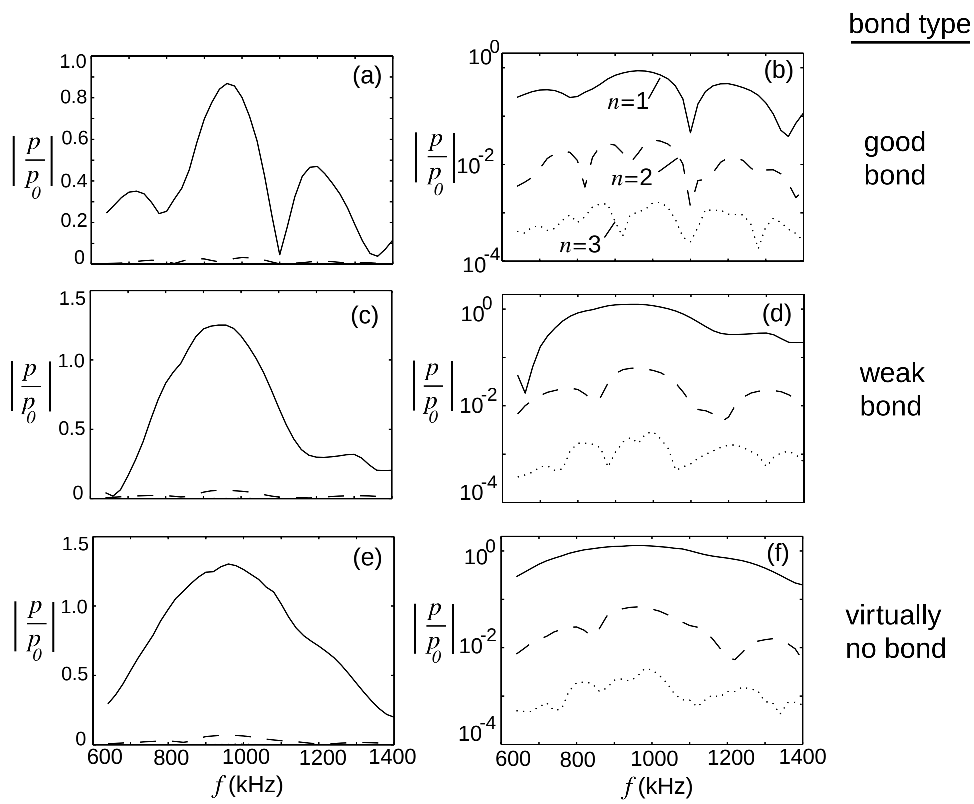

Figure 3.26: Normalized reflection from bonded acrylic plates, x_s = 4 cm and x_r= 1.5 cm. (a) and (b), good bond. (c) and (d), weak bond. (e) and (f), nearly split plates. Integer n indicates harmonic number.

shown on linear (left column) and logarithmic (right column) scales in order to see the structure of both the fundamental and the higher harmonics in detail. Each plate is 2.36 mm thick. The total propagation distance $x = 2x_r + x_s = 7$ cm is much smaller than the Rayleigh distance for the source used ($x/x_0 \approx 0.2$ at 1 MHz). As a result, these measurements are subject to rapid nearfield diffraction effects (as illustrated in Fig 3.23). Figure 3.26(a) and (b) (top row) shows measurements over an area where the plates are joined with a strong bond. In Fig. 3.26(c) and (d) (middle row) the insonified part of the plates is weakly bonded. The reflection maximum near 900 kHz is stronger, and reflection minima are less pronounced, than in the portion of the plates with a good bond. Some shifting of the resonance frequency is apparent at 650 kHz and 1.25 MHz. Minima and maxima in the measured second and third harmonic occur because the reflected second harmonic can be phase shifted with respect to the second harmonic generated in the reflected primary beam, resulting in interference in the second harmonic at the receiver.

In Fig. 3.26(e) and (f) (bottom row) the plates are nearly split. The first three harmonics are shown. Reflection of the sound beam from the plates is stronger in this region than in the strongly or weakly bonded regions. Because the path of the sound beam is short, harmonic generation in the fluid is kept to a minimum. If the generation of second or third harmonics at the interface $x = d$ is strong, we expect to measure anomalously large harmonic amplitudes in the vicinity of every other pass-band frequency. We do not observe such behavior in either the second or third harmonic.

Reflection measurements for the case in which $x_s = 4$ cm and $x_r = 15$ cm are shown in Fig. 3.27. The total propagation distance $2x_r + x_s = 34$ cm is approximately equal to the Rayleigh distance at 1 MHz, so the spatial variation is much less rapid than in the measurements for $x_r = 1.5$ cm (Fig. 3.23). However, because the propagation distance is larger there is much more cumulative harmonic generation in the fluid, which further obscures any second or third harmonics generated by contact nonlinearity.

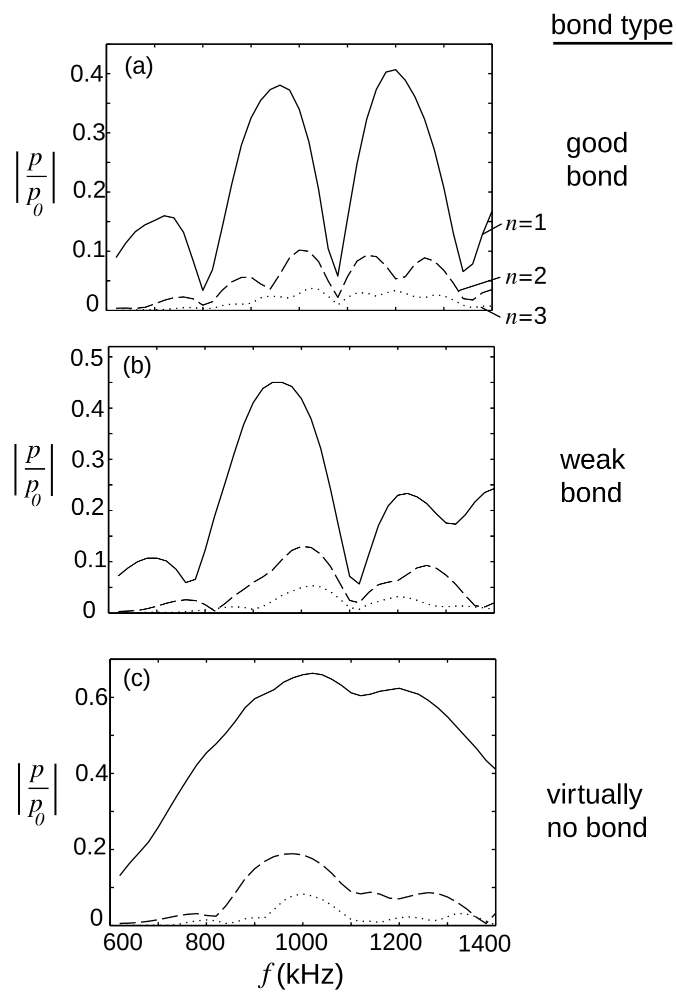

Figure 3.27: Harmonic amplitudes measured in beams reflected from bonded acrylic plates, $x_s = 4$ cm and $x_r = 15$ cm. (a) good bond, (b) weak bond, (c) nearly split plates. Integer n indicates harmonic number.

Transmission experiments were also performed on the acrylic plates. The experimental configuration for the transmission experiments is shown in Fig. 3.28. The distance between the source and the plate is x_i, and the distance between the plate and the hydrophone is x_t. Transmission through the acrylic plates is shown in Fig. 3.29. The source-plate separation x_i is 15 cm, and the plate-hydrophone separation x_t is 1.5 cm. The source pressure is $p_0 = 230$ kPa. The distance between the source and plate is large enough that nearfield oscillations do not interfere with the measurements. Moreover, because the source-to-plate distance is much larger than the plate-to-hydrophone distance, almost all the harmonics generated in the fluid are generated before the wave strikes the plate. In Fig. 3.29(a) the bond between the plates is good. The insonified part of the bond is weak in Fig. 3.29(b), and in Fig. 3.29(c) the plates are nearly separated. As the bond weakens, the resonance at the pass-band frequency becomes more pronounced. The ratio between the harmonics and the fundamental does not increase significantly from Fig. 3.29(a) to Fig. 3.29(c), and nowhere is the harmonic level as strong a function of frequency as predicted by the theory in Sec. 3.2 (see Fig. 3.22). Any harmonic generation at the adhesive bond is obscured by the harmonics generated in the primary beam. In Fig. 3.29(c) the second harmonic at 850 kHz is only about 6 dB below the fundamental, which may be the result of contact nonlinearity. However, because the measured field is erratic at all frequencies, we cannot be confident that the harmonic generation is from contact nonlinearity rather than nonlinearity of the fluid.

3.3.3 Two bonded aluminum plates

Transmission through two bonded 1/16 in. thick aluminum plates is shown in Fig. 3.30. Material constants for aluminum are given in Table A.1. Because the aluminum plates are opaque, the bond quality could not be monitored visually. Source-plate separation x_i was 150 mm and the source pressure was $p_0 = 230$ kPa. Because there is a much larger impedance ratio for aluminum/water than acrylic/water, a few more cycles are required to reach a steady state. (This is because the quality factor is higher for resonances in the

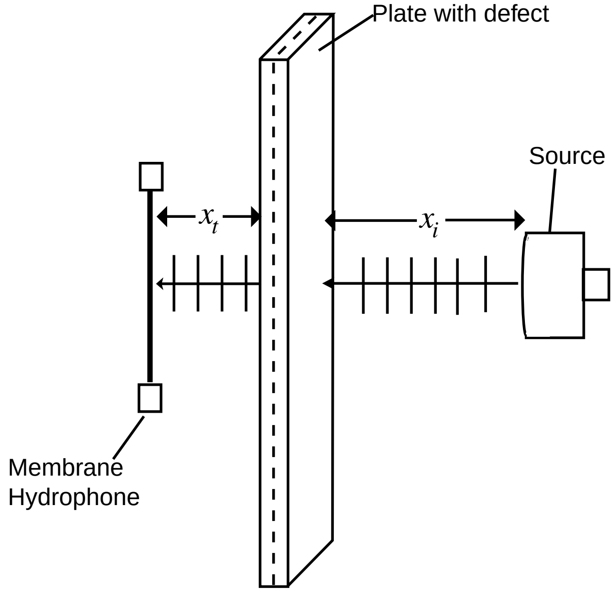

Figure 3.28: Geometry for the transmission experiments.

aluminum plates than it is for acrylic plates.) For this reason, we increase x_t to 2 cm.

Predictions are shown on the left side of Fig. 3.30 for the transmission of the fundamental, second, third, and fourth harmonic. We assume that all harmonic generation takes place in the fluid, and that the transmission is completely linear. Furthermore, the harmonics are assumed to interact with the plate independently of one another. Magnitudes of the harmonics generated in the primary beam are estimated using simple plane-wave theory.[70]

Figure 3.30(a) shows the transmission through one aluminum plate that is 3.048 mm (approximately 1/8 in.) thick. Pass bands are at regular frequency intervals. Harmonics propagate through the plate as if they were small-signal plane waves at their respective frequencies. The pass-band for the fundamental and the corresponding pass-band at the third harmonic have a notch corresponding to the excitement of a Lamb wave in the plate. This is not taken into account using our plane-wave theory because Lamb waves are excited by waves incident

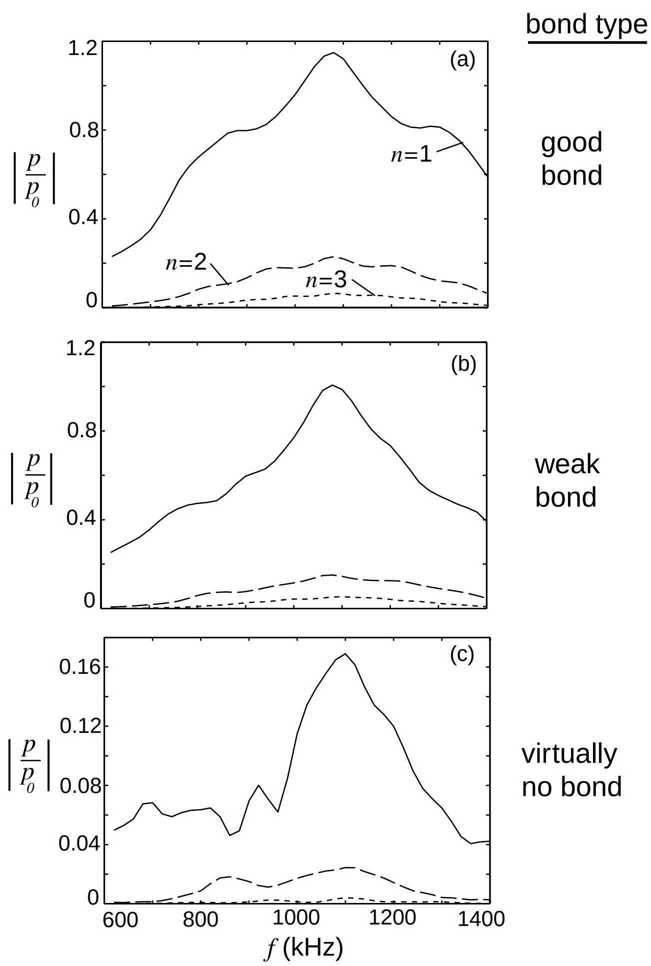

Figure 3.29: Harmonic amplitudes measured in beams transmitted through bonded acrylic plates, $x_i = 15$ cm, and $x_t = 1.5$ cm. (a) good bond, (b) weak bond, (c) nearly separated plates. Integer n indicates harmonic number.

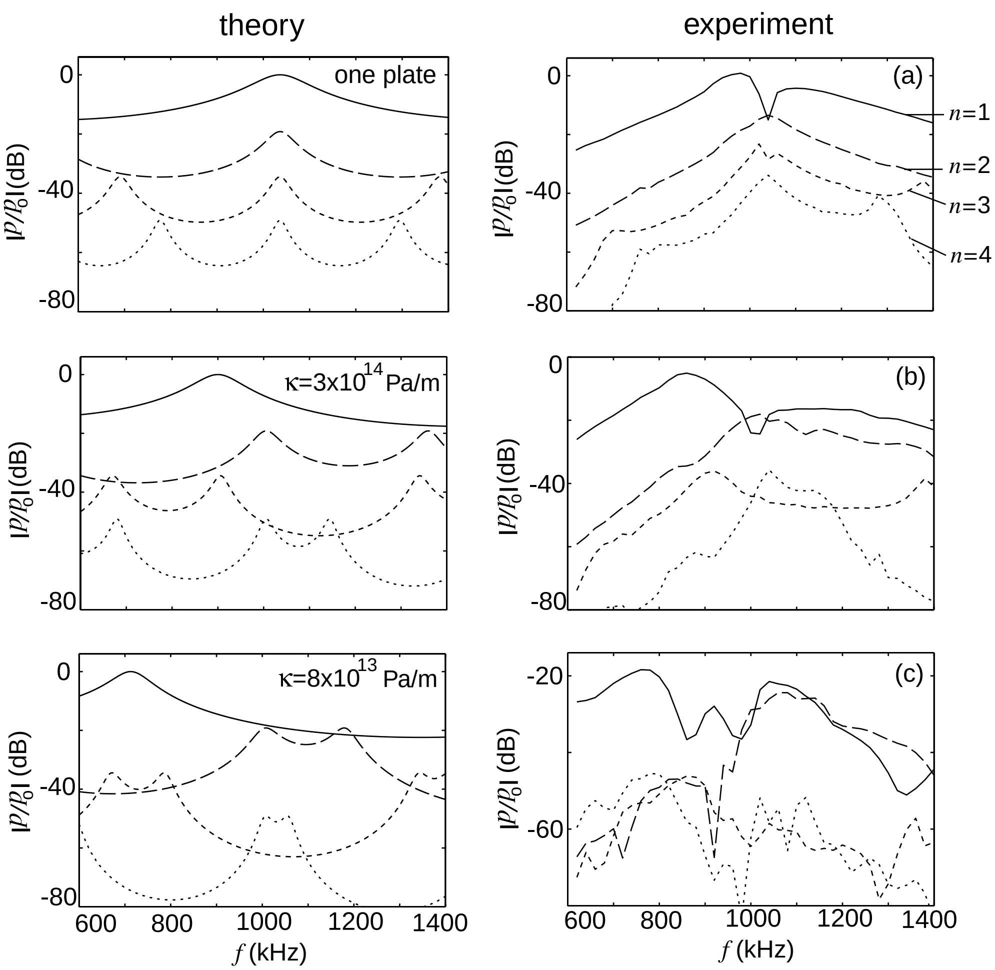

Figure 3.30: Harmonic amplitudes measured in beams transmitted through bonded aluminum plates, $x_i = 150$ mm, $x_t = 20$ mm. (a) one plate (approximately 1/8 in. thick), (b) two 1/16 in. plates with a good bond, (c) two 1/16 in. plates with a weak bond. Integer n indicates harmonic number.

obliquely upon the plate. A diffracting sound beam can excite Lamb waves even when it is normally incident upon a plate because, as mentioned earlier, it consists of plane-wave components propagating in off-axis directions.

In Fig. 3.30(b) is shown the transmission through two 1/16 in. aluminum plates with a good bond. There is qualitative agreement of experiment with linear theory for a spring constant $\kappa = 3 \times 10^{14}$ Pa/m. Some shifting of the resonance near 1 MHz is seen. Above 1 MHz transmission of the second harmonic is stronger than in Figure 3.30(a), which corresponds to the resonance shifting down in frequency at 2.7 MHz (1.35 MHz for the fundamental). The third harmonic is shifted down to 2.7 MHz, as well. The fourth harmonic, near 4.4 MHz, is stronger than the third harmonic, which agrees with the prediction.

Figure 3.30(c) shows measurements of transmission through the plates with a weak bond. Transmission of the fundamental is decreased by 20 dB, and the pass band is further shifted down in frequency. The second harmonic near 2.2 MHz is stronger than the fundamental near 1.1 MHz. The measured maximum of the third harmonic near 2.4 MHz is in agreement with the prediction. Also, the fourth harmonic near 4 MHz is stronger than the third harmonic near 3 MHz.

Transmission measurements were also made using a focused source. The focused source allows us to insonify the plate at a higher sound pressure than would be possible with a plane piston, with the hope of enhancing contact acoustic nonlinearity. The source we used had a focal length of 16.2 cm, a source radius of 1.8 cm, and a resonance frequency of 2.2 MHz. The source pressure was $p_0 = 72$ kPa.

The gain of the transducer (sound pressure at the focus relative to that at the source) equals $ka^2/2d$, where $k = \omega/c$; at the resonance frequency, the gain is 9.3. At the focus, the gain is proportional to the frequency. As shown in Fig. 3.31, the increasing gain as a function of frequency approximately offsets the decreasing source response at high frequencies. Thus, a wide frequency band can be investigated even if the source radiates efficiently over only a narrow range of frequencies.

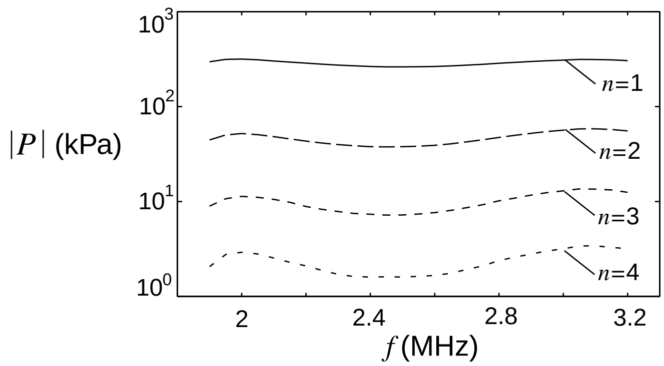

Figure 3.31: Measurement of sound pressure at first four harmonics from focused source, for which source-hydrophone separation is 150 mm, and $p_0 = 36$ kPa. Integer n indicates harmonic number.

A disadvantage of using a focused source is that the angular spectrum of the radiated field is much wider than the corresponding spectrum for the plane piston. Figure 3.32 shows a comparison between angular spectra $D(\theta)$ for a 1 MHz, 1.27 cm radius plane piston with a 2.2 MHz, 18 mm radius focused piston with a focal distance of 162 mm. Because the angular spectrum of the focused source is wider than the angular spectrum of the plane piston source, we expect the excitation of Lamb waves to have a stronger impact on the transmitted pressure for the focused source. Also, resonances for a plane wave at normal incidence will have less of an effect on the transmitted pressure.

Results of the transmission experiment using the focused source are shown in Fig. 3.33. In Fig. 3.33(a) the transmission is through one 1/8 in. aluminum plate. The pass-band frequencies are spaced at regular intervals over the frequency band from 1.9 to 3.2 MHz. Figure 3.33(b) shows the transmisison through two 1/16 in. plates in a region where the bond is good. Every other pass band is missing, and the pass bands that remain are broadened. Near 2.8 MHz the third harmonic is higher in magnitude than the second harmonic. In Fig. 3.33(c) is shown the transmission through a region with a weak bond. The magnitude

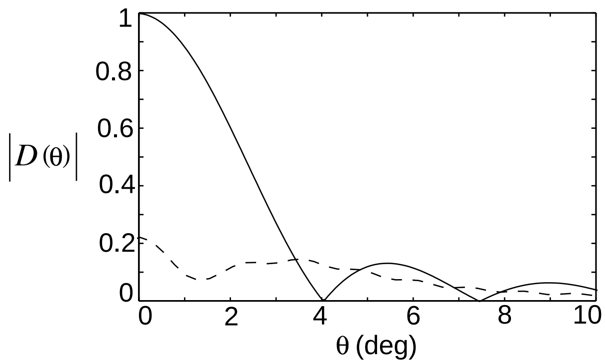

Figure 3.32: Comparison of directivity $|D(\theta)|$ for 1 MHz plane piston with $a =$ 1.27 cm (—) with directivity for 2.2 MHz, focused piston with $a = 18$ mm and focal distance $d = 162$ mm (- -).

of the fundamental is greatly attenuated compared with Fig. 3.33(a) and (b). The harmonics are increased in magnitude with respect to the fundamental, especially in the case of the fourth harmonic, which is higher in amplitude than the third harmonic over much of the frequency band investigated. The magnitude of the transmitted sound pressure at the fundamental and second harmonic decreases by an order of magnitude from 2 to 3.2 MHz. At 3.1 MHz the third harmonic is stronger than the fundamental, which may be attributable to contact nonlinearity.

3.3.4 Attempts to enhance contact nonlinearity

In addition to measurements made with bonded plates, we wished to examine the behavior of an interface at which two plates are pressed together. A device, shown in Fig. 3.34, was built to press the plates together. The device was made of stainless steel so it could be immersed in water without rusting. Care was taken to make sure the slot through which the sound beam passes was wide

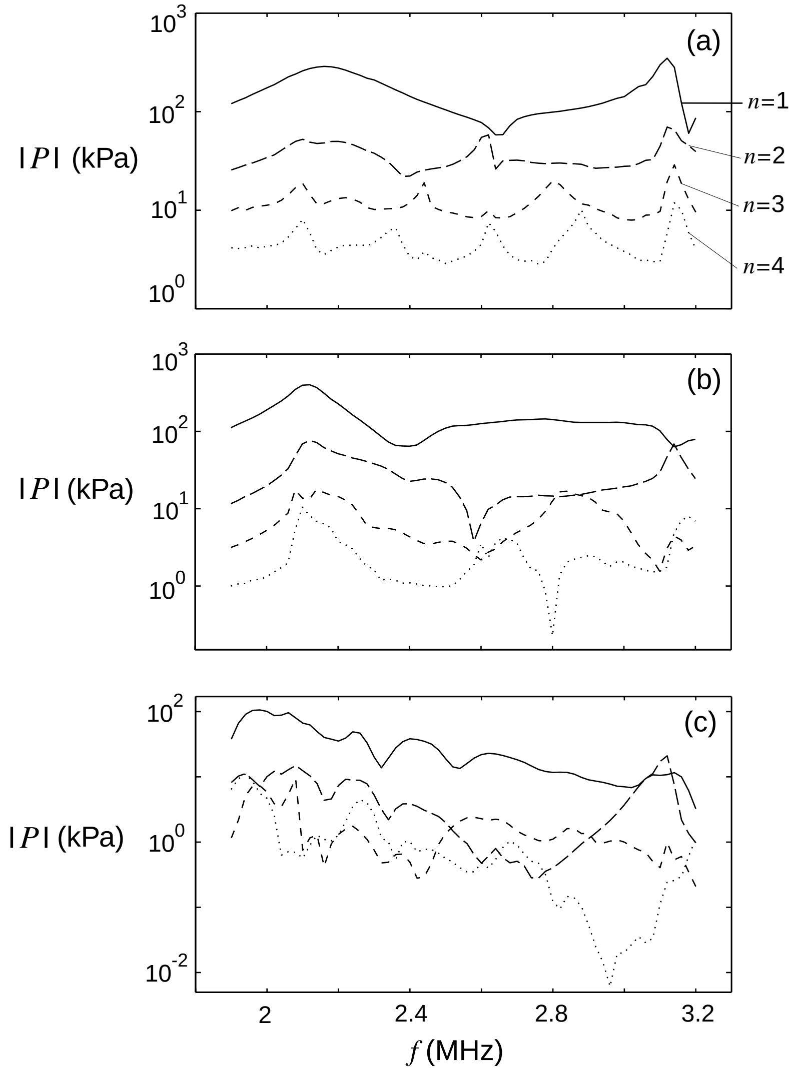

Figure 3.33: Harmonic amplitudes measured in focused beam transmitted through aluminum plates, $x_i = 150$ mm and $x_t = 20$ mm. Integer n indicates harmonic number. (a) one plate (approximately 1/8 in. thick), (b) two 1/16 in. plates with a good bond, (c) two 1/16 in. plates with a weak bond.

enough that the sound field was not disturbed. Although the plates were pressed together with the maximum force we could attain, the transmission through the plates was approximately zero.

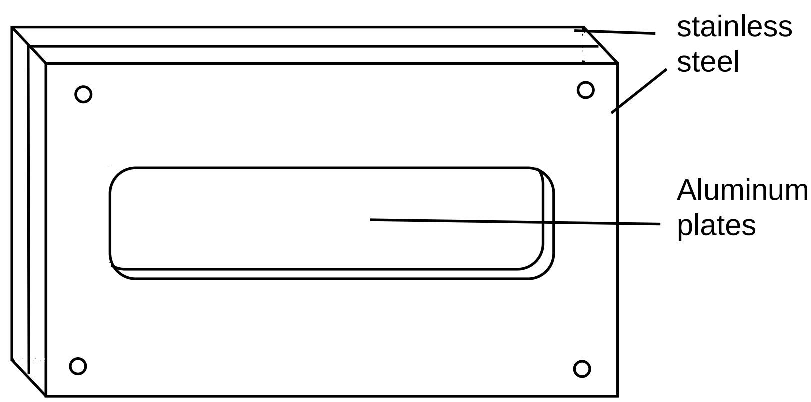

Figure 3.34: Stainless steel device to push plates together.

A simple estimate of the particle displacement in the plates sheds light on our problem. In order for transmission to occur between the plates, a significant portion of the plates must be in contact at a distance scale on the order of the particle displacement. For a progressive plane, time-harmonic wave, $|p| = |\rho c u| = |\rho c \omega \xi|$. Assuming an acoustic pressure magnitude of 1 MPa, for aluminum at 1 MHz the magnitude of the particle displacement is $\sim$ 10 nm. We were unable to achieve such intimate contact. Some experimenters[26,32] optically polished their samples to make the contact between the plates as intimate as possible. However, this technique is impractical for a large sample. Another potential solution is to place the sample in a machine to exert a large load.[29] This technique is impractical for our experiment because we are interested in resonance phenomena in plates, and a loading frame would disturb the acoustic field in a plate.

We attempted to enhance contact nonlinearity by introducing particles that are known to have a nonlinear stress-strain relationship to the interface. As illustrated in Fig. 3.35, small glass spheres, from 0.1 mm to approximately 1 mm in diameter, were sprinkled liberally between the plates. As mentioned earlier, spheres in contact exhibit Hertzian nonlinearity.[34] However, when the interface was sealed so that it was watertight, the transmission of the sound beam was very small in magnitude. We were unable to achieve an intimate enough contact between the plates and the spheres to achieve significant transmisison. When water was allowed to enter the space with the spheres, a reasonable transmission was attained, and it appeared that we saw anomalous harmonic generation. However, upon closer inspection we found that the peak was due to a (linear) resonance of the water column at the second harmonic frequency. The second harmonic generated in the fluid was at the resonance frequency of the water column, and so its transmission through the plates was large.

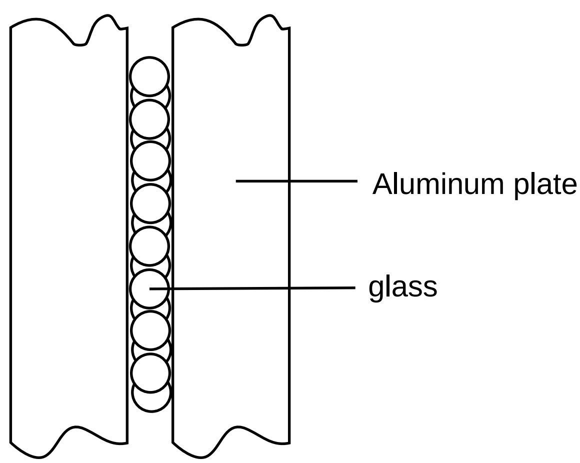

Figure 3.35: Glass spheres at interface to enhance contact nonlinearity.

3.4 Determination of transmission coefficient using a broadband pulse excitation

Measurements reported in Sec. 3.3 indicate that linear effects dominate the response of our bonded samples. Rather than using a sinusoidal excitation, we can excite the sample with a broadband pulse to quickly obtain the linear response of the sample over a large range of frequencies. The primary advantage of this method over a swept-frequency method is that it may be performed very rapidly.

If the response of the plate to an incident sound wave is linear, the transmitted pressure $p_t(t)$, given an incident pressure $p_i(t)$, is given by

$$p_t(t) = \int w(t-t')p_i(t')dt' \,. \tag{3.58}$$

Here, $w(t)$ is the impulse response; i.e., the transmitted signal for an incident impulse. Applying a Fourier transform to both sides of Eqn. (3.58) gives

$$\widehat{P}_t(\omega) = W(\omega)\widehat{P}_i(\omega) \,, \tag{3.59}$$

where $W(\omega)$, which is the Fourier transform of $w(t)$, is the frequency-dependent reflection or transmission coefficient, e.g., Eqn. (3.26), and $\widehat{P}_i(\omega)$ and $\widehat{P}_t(\omega)$ are the Fourier transforms of p_i and p_t, respectively. In the next section, we obtain $W(\omega)$ from measurements of $\widehat{P}_t(\omega)$ and $\widehat{P}_i(\omega)$.

3.4.1 Experimental results

An immersion transducer with a focal length $d = 162$ mm, radius $a = 18$ mm, and resonance frequency of 2.2 MHz was used to perform the experiment. The signal from the function generator was one cycle of a square wave having a fundamental frequency of 10 MHz. The focused source was chosen because the increase in gain with frequency approximately offsets the transducer's high-frequency rolloff characteristics. For this reason, at the focus the effective bandwidth far exceeds the resonance bandwidth of the transducer.

Figure 3.36 shows the measured waveforms of the incident wave $p_i(t)$ in a free field (top), the frequency spectrum of the incident wave $|\widehat{P}_i(\omega)|$ (middle), and the wave $p_t(t)$ transmitted through an aluminum plate (bottom). (Units are volts; an advantage of this technique is that source and receiver calibrations are unneccessary.) Material constants for the plate are given in Table A.1. The excitation $p_i(t)$ is measured along the beam axis using the PVDF membrane

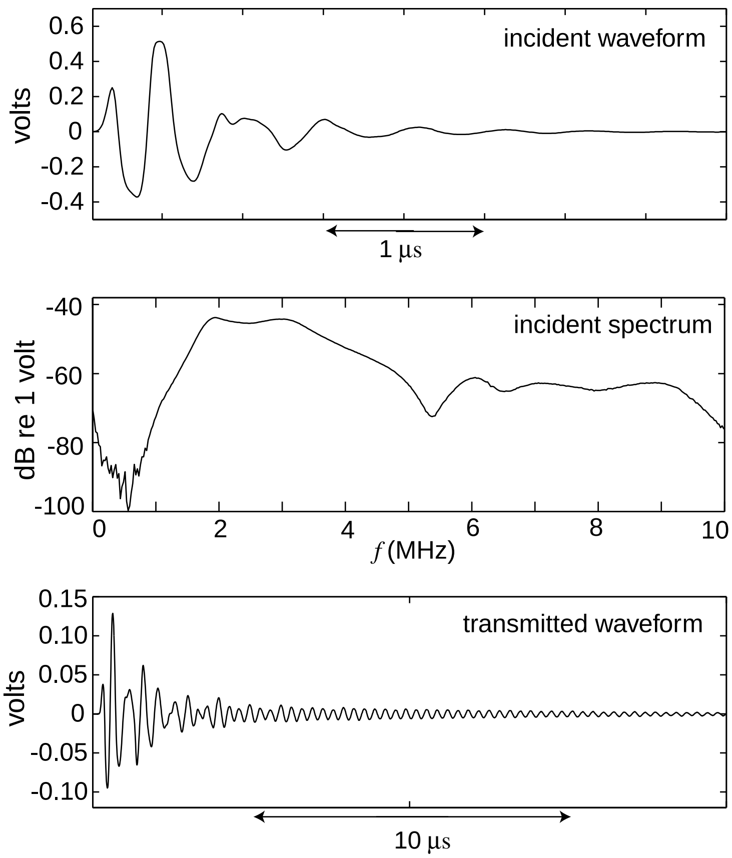

Figure 3.36: Incident (top) waveform, with magnitude of spectrum (middle), and transmitted waveform (bottom). A focused source is used, with focal length $d = 162$ mm and source radius $a = 18$ mm. Incident waveform measured at 170 mm from source, with no plate in between. Transmitted waveform measured at 170 mm from source, with 1/8 in. aluminum plate 150 mm from source.

hydrophone at 170 mm from the source. The response $p_t(t)$ is measured along the beam axis at $x_i = 150$ mm and $x_t = 20$ mm. The plot of $|\widehat{P}_i(t)|$ (middle) indicates that the frequency response of the plate can be measured using the incident waveform (top) from approximately 1 to 9 MHz. In Fig. 3.37 we present results for the transmission of an impulse through a plate. In Fig. 3.37(a), measurements for transmission through a single 1/8 in. plate (solid line) are in good agreement with theory (dashed line) up to approximately 5 MHz. For this plot, $|P_t|$ is the magnitude of the Fourier transform of the response waveform $p_t(t)$ shown in Fig. 3.36. The theoretical model used includes effects of diffraction, and will be discussed in Chap. 4. Parameters used for the plate for the theory are given in Table A.1.

Some qualitative features predicted in Sec. 3.1.4 can be seen in the measurements in Fig. 3.37. For a single 1/8 in. plate, pass-bands are regularly spaced in frequency. Pass bands near 1, 3, 5.. MHz are different than what is predicted by one-dimensional theory, because of diffraction effects and the excitation of guided modes in the plate. For two 1/16 in. plates joined with a good bond, two differences from the transmission through a single plate are evident. First, some pass-band frequency shifting is observed. In particular, the pass band at 3 MHz is shifted downward in frequency. Also, the transmission at 3, 5, 7.. MHz is reduced significantly. The transmission through two 1/16 in. plates joined with a weak bond shows that significant transmission only occurs at 2, 4, 6.. MHz, and the overall transmission is reduced more at higher frequencies. Also, the first pass band is lowered in frequency from near 1 MHz to near 0.7 MHz.

3.5 Discussion

Attempts to observe contact nonlinearity were unsuccessful. Any harmonic generation at the contact boundary was masked by harmonic generation in the fluid. Even when the source was placed close to the plates, all observed harmonic generation could be attributed to the cumulative harmonic growth in the surrounding fluid rather than contact nonlinearity at the interface. In addition, placing the

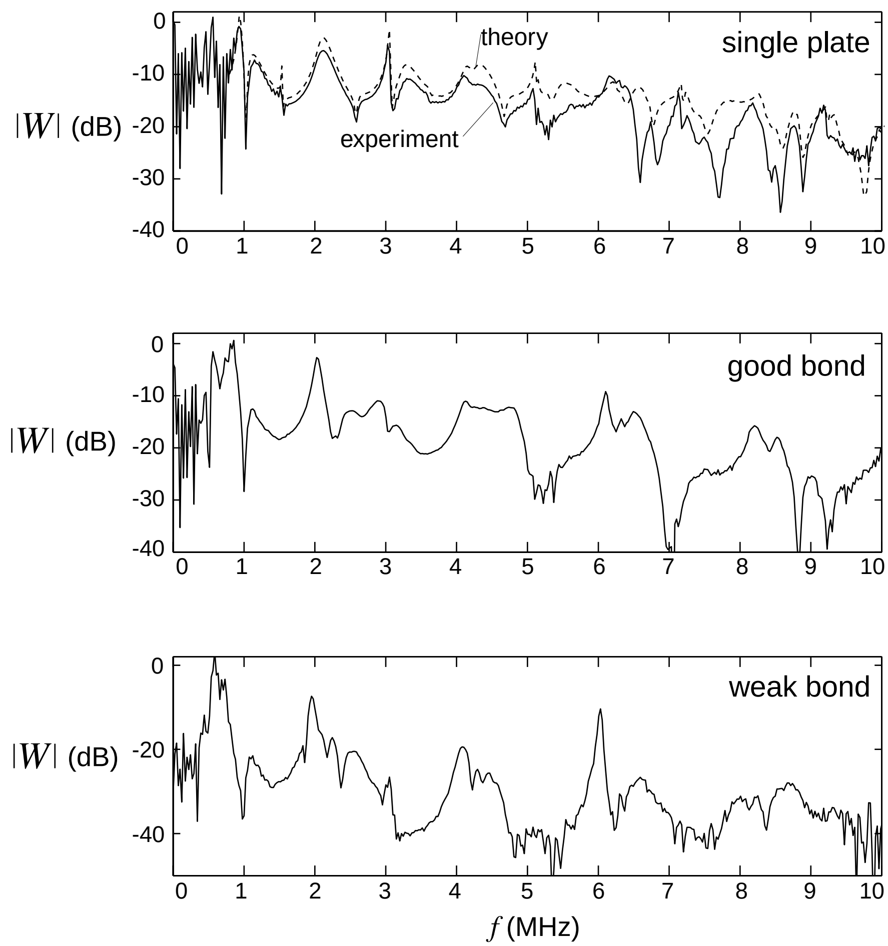

Figure 3.37: Magnitude of transmission coefficient $|W|$ using the impulse response method. Theory (- -) is compared with measurement (—) for transmission through a 1/8 in. aluminum plate (top). Measured transmission is shown through two 1/16 in. aluminum plates joined with a strong epoxy bond (middle), and two 1/16 in. aluminum plates joined with a weak epoxy bond (bottom).

source close to the plates makes accurate comparison of measurements with theory difficult because of spatially rapid nearfield diffraction effects.

The introduction of a spring-like boundary changed the linear, frequency-dependent transmission and reflection coefficients in the plates. As the spring softened, the first effect was a shifting of certain pass-band frequencies. If the incident sound beam contains a significant harmonic content, the shifting of these pass-band frequencies can result in a disproportionate transmission of the higher harmonics, giving the illusion that contact nonlinearity is indeed occurring. This effect, combined with the cumulative generation of harmonics in the sound beam as it propagates in the fluid, makes it difficult to identify the anomalous generation of harmonics at the nonlinear interface. It is possible, however, that the linear resonance frequency shifting may be exploited to measure the spring constant at a bonded interface. As shown in Sec. 3.4, an impulse response method may be an effective and rapid method to evaluate the bond quality of adhered plates.

We expected the generation of higher harmonics due to contact nonlinearity to be strongly frequency dependent. However, in practice, we contended with linear frequency filtering effects, which at certain frequencies could disproportionately pass the harmonics present in the incident sound beam with respect to the fundamental. It is important to recognize that these effects may occur, because a naïve interpretation of results may lead an experimenter to attribute this strong transmission or reflection of harmonics to contact nonlinear mechanisms, where in fact such mechanisms may not exist.

Although the measurement of contact nonlinearity has been reported in the literature, most experiments performed had important differences with our experiment. Most other experiments used contact transducers to excite shear waves, which were reflected from the contact boundary. Also, the solids used in other experiments to measure contact nonlinearity were typically thick, so that they could be pressed together without disturbing the acoutic field in the samples. The experiment closest to ours that we could find in the literature was performed by Rothenfusser *et al.*,[37] discussed in the introduction to this chapter. In this paper, the authors reported the generation of second harmonic in an adhesive layer with varying thickness between two thin plates. However, in contrast to our work, the authors apparently used contact transducers, which would reduce the second harmonic generated in the primary beam before interaction with the sample. Also, there are aspects of this paper that raise some questions. First, the magnitude of the second harmonic generated in a control experiment with no sample is not reported. Also, resonance effects are considered in the adhesive bond, but not in the bonded plates themselves. Because the plates are 1 mm thick pieces of fused silica, and the frequency of the excitation is 2 MHz, resonance effects are expected at both the fundamental and second harmonic. An adhesive bond with a variation of thickness on the order of 10% of the thickness of the plates could potentially have a strong effect on the resonance properties of the sample. It is possible that the second harmonic reported by Rothenfusser *et al.* was generated outside of the sample, and the sample with varying thickness acted as a filter, rather than a source, of second harmonic.

Chapter 4

IRRADIATION OF A PLATE BY A FINITE-AMPLITUDE SOUND BEAM AT OBLIQUE INCIDENCE

In Chaps. 2 and 3 we investigated the interaction of plane waves with plates at normal incidence. The analysis was kept as simple as possible in order to explore more easily the feasibility of using the techniques proposed there in a practical arrangement for materials characterization and nondestructive testing. In the cases we considered, we found that the nonlinear effects that occur within the plates are small compared with the nonlinear effects that occur in the surrounding fluid.

In this chapter we extend our investigation to include diffracting sound beams at oblique angles of incidence. At certain angles of incidence, the sound beam excites Lamb waves that propagate within a plate along the plane of the plate. As discussed in Sec. 1.1.2, if a plate is surrounded by a fluid, the energy in the Lamb wave radiates (or "leaks") into the fluid as it propagates. For a sound beam incident upon a plate, the leaky wave interferes with the specularly reflected and transmitted fields, causing nonspecular effects. The observation of nonspecular phenomena can be used for nondestructive evaluation. By measuring the angles at which nonspecular effects occur, indicating that Lamb waves are excited in the plate, one can determine the linear elastic constants of the sample.

If the sound beam used for the NDE is nonlinear, nonspecular phenomena must be included in order to model the nonlinear effects correctly. Also, the second harmonic generated by a sound beam has lower sidelobes and a smaller beamwidth than the fundamental, so use of the second harmonic to measure angles at which nonspecular effects occur may offer some advantages over the use of the fundamental. In addition, use of the second harmonic can potentially increase the effective bandwidth of a source. The tradeoff is the added complexity of calculating the reflected or transmitted second harmonic field.

In this chapter we investigate the behavior of a diffracting sound beam that is obliquely incident upon a homogeneous, isotropic, elastic plate, including non-specular effects. The objective of the work is to develop a model of the interaction involving both the fundamental and second harmonic, and to compare it quantitatively with measurement. Second harmonic generated in the fluid is taken into account, but it is assumed that no second harmonic is generated in the plate. We make this assumption based upon the results of Chap. 2, which indicated that harmonic generation in the fluid is much larger than harmonic generation in a homogeneous aluminum plate. The theory presented here follows closely the article by Landsberger and Hamilton for a thick solid.[64]

4.1 Linear theory

In this section we present theory describing the interaction of a linear, diffracting sound beam at angular frequency ω with an isotropic, elastic plate. The configuration is shown in Fig. 4.1. The sound beam is obliquely incident upon a plate at angle θ_0. The distance from the plate to the source is d_i, and the distance from the plate to the hydrophone is d_r. The coordinate system is set up such that x and y are in planes parallel to the interfaces. The y coordinate, not shown in Fig. 4.1, points out of the page in accordance with the right-hand convention. Figure 4.2 shows the configuration for the transmission experiments. Coordinates are defined as in the reflection geometry, except that we define d_t, rather than d_r, to be the distance beween the plate and the hydrophone.

4.1.1 The spatial Fourier transform

We account for diffraction by using an angular spectrum method to represent the sound field. A two-dimensional Fourier transform is applied to the spatial pressure distribution in a plane parallel to the plane of the plate. The resulting

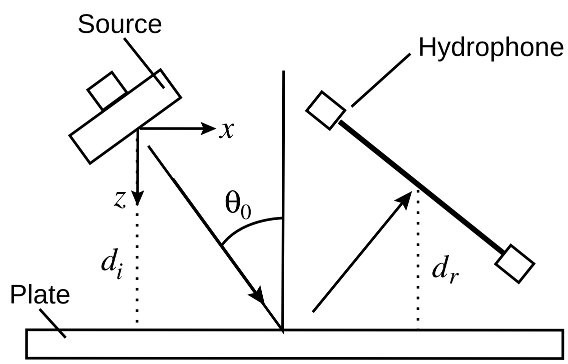

Figure 4.1: Experimental setup for reflection experiments.

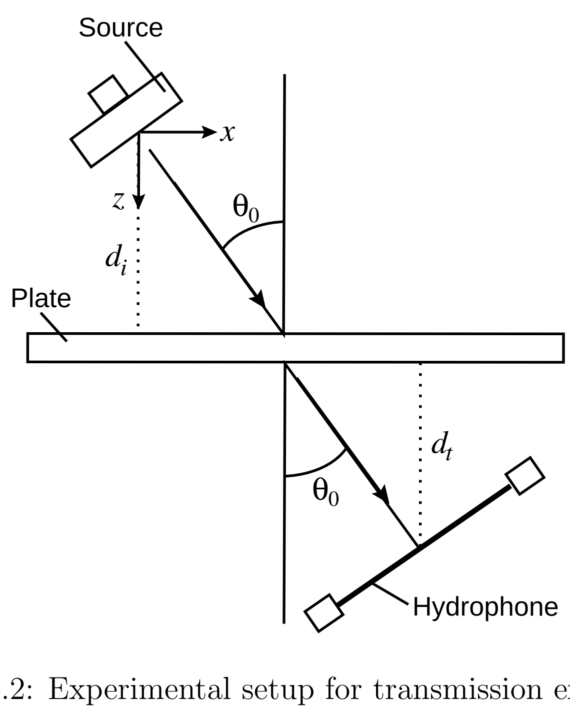

Figure 4.2: Experimental setup for transmission experiments.

angular spectrum describes the distribution of the pressure field in that plane with respect to propagation direction.

Besides being a standard technique, the two-dimensional Fourier decomposition approach has three primary advantages for our work: first, by not restricting ourselves to axisymmetric pressure fields we may consider sound beams at oblique angles of incidence to the plate. Also, it is convenient to represent the pressure field in terms of plane wave components propagating in different directions when dealing with the angle-dependent plane-wave transmission and reflection coefficients of a plate. The third advantage is that the Fourier integrals may be computed efficiently using a standard Fast Fourier transform algorithm.

When modeling a diffracting sound beam, it is common to employ a parabolic approximation, in which it is assumed that changes in the sound beam in the transverse direction occur much more rapidly than changes along the propagation direction. The parabolic approximation is valid only where small interaction angles are involved. The Fourier spectrum method used here does not employ a parabolic approximation. By avoiding the restrictions imposed by making the parabolic approximation, we can model sound beams propagating at all angles with respect to the plate normal. This becomes important when modeling sound beams at large angles of incidence upon the plate.

The Fourier transform employed in this chapter converts a spatial distribution of acoustic pressure to a distribution in wave vector space. The wave vector $\mathbf{k}$ has magnitude $|\mathbf{k}| = k = \omega/c_0$ and propagation unit vector given by $\mathbf{k}/k$. We decompose the wave vector into components in the (x, y) plane, given by $\boldsymbol{\kappa} = (k_x, k_y)$, and along the z axis, given by $K = k_z = \sqrt{k^2 - |\boldsymbol{\kappa}|^2}$. The components are illustrated in Fig. 4.3. For a plane wave propagating at angle θ with respect to the z axis, one can see from Fig. 4.3 that $\sin\theta = |\boldsymbol{\kappa}|/k$.

For some spatially-dependent function $f(\mathbf{x})$, where $\mathbf{x} = (x, y)$, we define the following two-dimensional spatial Fourier transform pair:

$$\widehat{f}(\boldsymbol{\kappa}) = \mathcal{F}\{f(\mathbf{x})\} = \int f(\mathbf{x}) e^{-j\boldsymbol{\kappa}\cdot\mathbf{x}}\, d\mathbf{x}\,, \tag{4.1}$$

$$f(\mathbf{x}) = \mathcal{F}^{-1}\{\widehat{f}(\boldsymbol{\kappa})\} = \int \widehat{f}(\boldsymbol{\kappa}) e^{j\boldsymbol{\kappa}\cdot\mathbf{x}}\, \frac{d\boldsymbol{\kappa}}{(2\pi)^2}\,. \tag{4.2}$$

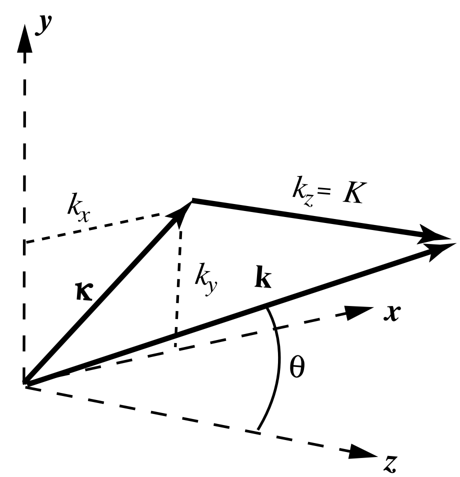

Figure 4.3: Components of wave vector **k**.

An alternative to Eqns. (4.1) and (4.2) that is convenient for an axisymmetric pressure field is the zeroth-order Hankel transform pair

$$\widehat{f}(k_r) = \mathcal{F}\{f(r)\} = \int f(r) J_0(k_r r)\, r dr\,, \tag{4.3}$$

$$f(r) = \mathcal{F}^{-1}\{\widehat{f}(k_r)\} = \int \widehat{f}(k_r) J_0(k_r r)\, k_r dk_r\,, \tag{4.4}$$

where k_r is the wavenumber in the r direction.

In our analysis we apply Eqns. (4.1) and (4.2) to an acoustic pressure field $p(\mathbf{x}, z, t)$ that satisfies the linear wave equation

$$\left(\nabla^2 - \frac{1}{c^2}\frac{\partial^2}{\partial t^2}\right) p(\mathbf{x}, z, t) = 0\,. \tag{4.5}$$

Assuming a monofrequency excitation, we represent p as

$$p(\mathbf{x}, z, t) = \tfrac{1}{2} P(\mathbf{x}, z) e^{j\omega t} + \text{c.c.}\,, \tag{4.6}$$

where $P(\mathbf{x}, z)$ is the pressure amplitude. Substitution of Eqn. (4.6) into Eqn. (4.5) gives

$$\left(\nabla^2 + k^2\right) P(\mathbf{x}, z) = 0\,. \tag{4.7}$$

Applying the Fourier transform given in Eqn. (4.1) to Eqn. (4.7) yields

$$\left(\frac{d^2}{dz^2} + K^2\right) \widehat{P}(\boldsymbol{\kappa}, z) = 0\,. \tag{4.8}$$

For propagation in the positive z direction, the solution to Eqn. (4.8) is

$$\widehat{P}(\boldsymbol{\kappa}, z) = \widehat{P}(\boldsymbol{\kappa}, z_0)e^{-jK\Delta z}\,, \tag{4.9}$$

where $\Delta z = z - z_0$. From Eqn. (4.2), the pressure field at z is given by

$$P(\mathbf{x}, z) = \mathcal{F}^{-1}\{\widehat{P}(\boldsymbol{\kappa}, z_0)e^{-jK\Delta z}\}\,. \tag{4.10}$$

Equation (4.10) shows that the Fourier transform pair provides a convenient means of modeling the propagation of an acoustic field.[73]

We wish to use Eqn. (4.10) to model the propagation of a sound beam. The two-dimensional Fourier transform is applied to the pressure distribution at the source plane, $P(\mathbf{x}, 0)$, over $\mathbf{x}$ to determine the source spectrum $\widehat{P}(\boldsymbol{\kappa}, 0)$. Here x and y are the coordinates in the plane of the fluid-solid interface. The source and receiver are aligned at $y = 0$, and the receiver is placed at positive z with respect to the source (see Figs. 4.1 and 4.2).

The source spectrum is determined by applying Eqn. (4.1) to the pressure field in the source plane, $P(\mathbf{x}, 0)$:

$$\widehat{P}(\boldsymbol{\kappa}, 0) = \mathcal{F}\left\{P(\mathbf{x}, 0)\right\}\,. \tag{4.11}$$

For a circular, plane piston source of radius a, whose axis is normal to the (x, y)-plane, we use the source condition*

$$P(\mathbf{x}, 0) = \begin{cases} p_0, & r \le a \\ 0, & r > a \end{cases}\,, \tag{4.12}$$

where $r = (x^2 + y^2)^{1/2}$ is the distance in the source plane from the axis. Applying Eqn. (4.11) to Eqn. (4.12), and using Eqn. (4.3) to evaluate the Fourier transform,

*The source condition for a true piston is given in terms of particle velocity rather than pressure; however, for a sound beam we make the plane-wave approximation $p_0 = \rho_0 c_0 u_0$. This approximation is valid for distances $d \sim a(ka)^{1/3}$ from the source and beyond.

gives the source spectrum

$$\widehat{P}(\boldsymbol{\kappa}, 0) = p_0 \pi a^2 \frac{2J_1\left(a\sqrt{k_x^2 + k_y^2}\right)}{a\sqrt{k_x^2 + k_y^2}} = p_0 \pi a^2 \frac{2J_1\left(a|\boldsymbol{\kappa}|\right)}{a|\boldsymbol{\kappa}|} \, . \tag{4.13}$$

From Eqn. (4.9) the pressure field at distance z from the source is given by

$$P(\mathbf{x}, z) = \mathcal{F}^{-1}\left\{\widehat{P}(\boldsymbol{\kappa}, 0)e^{-jKz}\right\} \, . \tag{4.14}$$

To our knowledge, there is no corresponding simple analytic expression for the source spectrum of a focused piston source, which has a source pressure distribution given approximately by

$$P(\mathbf{x}, 0) = \begin{cases} p_0 \exp\left(jkr^2/2d\right), & r \leq a \\ 0, & r > a \end{cases} \, , \tag{4.15}$$

where d is the focal distance for the source. In this case, the source spectrum must be determined numerically.

The angular spectrum for a 1 MHz, 1 in. diameter plane piston source is shown in Fig. 2.7. Most of the energy is within a few degrees of the beam axis. Consequently, a sound beam interacting with a plate will be affected by features in the plane-wave reflection and transmission coefficients over a range of about $\pm 2^\circ$.

4.1.2 Source rotation

We wish to accommodate sound beams incident upon the target with angle θ_0, as shown in Fig. 4.4. To do so we employ an angular spectrum rotation method, in which the source spectrum, e.g. Eqn. (4.13), is altered to produce the same source spectrum as an equivalent source rotated by θ_0.[64] We begin with the rotation matrix

$$\begin{pmatrix} \xi' \\ \zeta' \end{pmatrix} = \begin{pmatrix} \cos\theta_0 & -\sin\theta_0 \\ \sin\theta_0 & \cos\theta_0 \end{pmatrix} \begin{pmatrix} \xi \\ \zeta \end{pmatrix} \, . \tag{4.16}$$

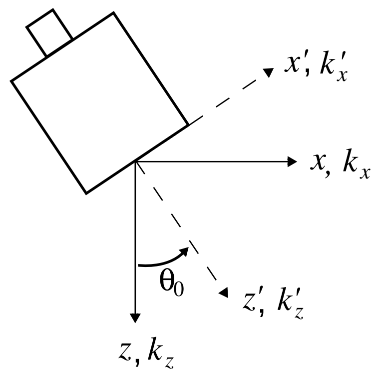

Figure 4.4: Source rotation.

For a coordinate transformation we set $(\xi, \zeta) = (x, z)$, and for a wavenumber transformation we set $(\xi, \zeta) = (k_x, k_z)$. The rotation is performed about the y axis, so $y = y'$ and $k_y = k_y'$. Upon substitution of the coordinate transformations into the Fourier integrals, the rotated source spectrum is

$$\widehat{f}(\boldsymbol{\kappa}, z = 0) = \frac{|k_z'|}{|k_z|} \widehat{f}(\boldsymbol{\kappa}', z' = 0) \,. \tag{4.17}$$

4.1.3 Lamb waves in a free plate

We begin the discussion of interaction of a sound beam with a plate by reviewing briefly the topic of Lamb waves in a free plate. The topic of Lamb waves is discussed in detail elsewhere,[72] and will be reviewed only very briefly here. As mentioned earlier, a solid plate supports both compressional and shear waves. The transverse and compressional waves that are excited by an incident plane wave and propagate in a plate are shown in Fig. 4.5. Although the incident wave is compressional, a shear wave is excited in the plate by mode conversion.

The equation that predicts the angles and frequencies for which Lamb waves propagate in a free plate is obtained by applying the following conditions to

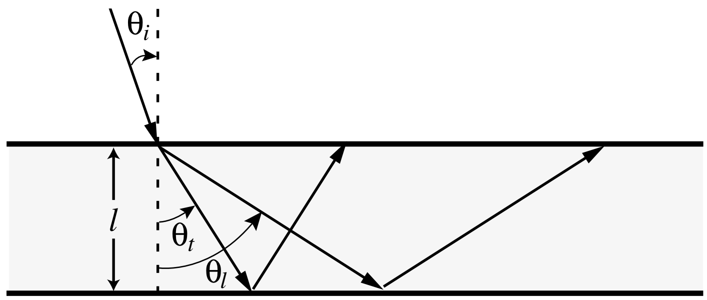

Figure 4.5: Angles of waves in a plate of thickness l.

wave equations for the compressional and shear waves in the plate. First, phase velocities of the components of the waves propagating along the direction of the plate are set equal to each other. Also, stress is set equal to zero at both faces of the plate. In principle, there are an infinite number of Lamb modes with different pressure distributions in the plate as frequency approaches infinity. However, in practice the first few modes are usually explored.

In Fig. 4.6 are shown the dispersion curves for Lamb waves in an aluminum plate in vacuum. Symmetric modes, designated with an s, are modes whose vibration is symmetric about the centerline of the plate, and antisymmetric modes, designated with an a, are modes whose vibration is antisymmetric about the centerline of the plate. Although the Lamb wave dispersion curve is typically displayed in terms of phase velocity along the vertical axis, it is more convenient for our purposes to present it in terms of the angle of the incident plane wave (in water). The angles θ_t and θ_l are related to the angle of incidence θ_i by Snell's law. Strictly speaking, representation of this dispersion curve in terms of incidence angle is incorrect because the Lamb dispersion relation shown is for a free plate, and the effect of loading on the plate by the surrounding fluid is not included. However, this representation is a good approximation as long as $\rho_f \ll \rho_s$,[43] which is satisfied for an aluminum plate in water ($\rho_s/\rho_f \approx 3$). At 1 MHz, Fig. 4.6 shows that four Lamb modes may be excited, two symmetric and two antisymmetric.

At 2 MHz seven modes may be excited, although the modes a_0 and s_0 join to form what is known as the 'pseudo-Rayleigh' mode, whose behavior is similar to the Rayleigh surface wave.

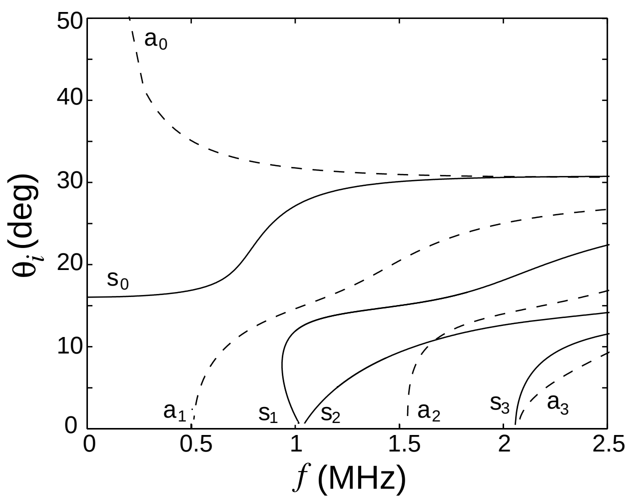

Figure 4.6: Lamb wave excitation angles for an aluminum plate in vacuum. Symmetric (—) and antisymmetric (- -) modes are shown. Properties for the plate are given in Table A.1.

4.1.4 Reflection and transmission for plane waves

In order to describe the interaction of a sound beam with a plate, we do not need to use a theory that tracks the propagation of compressional and shear waves through the plate. Rather, we describe the interactions using angle- and frequency-dependent complex reflection and transmission coefficients. These functions describe the complete interaction of a plane wave with a plate, including the excitation of Lamb waves. Because we assume that no second harmonic is generated within the plate, we do not need an expression for the pressure distribution there.

The reflection and transmission coefficients for a plane wave propagating in a fluid incident obliquely upon an elastic, isotropic, homogenous plate of thickness l

are given by Brekhovskikh.[74] These coefficients account for the presence of longitudinal and transverse waves in the plate. Although the coefficients were derived for lossless plates, absorption may be taken into account *ad hoc* by introducing complex wave speeds.[53] The pressure reflection coefficient is

$$V = j\frac{M^2 - N^2 + 1}{2M + j\left(M^2 - N^2 - 1\right)}\,, \tag{4.18}$$

and the corresponding transmission coefficient is

$$W = \frac{2N}{2M + j\left(M^2 - N^2 - 1\right)}\,, \tag{4.19}$$

where

$$N = \frac{\psi_l \cos^2 2\theta_t}{\psi_f \sin P} + \frac{\psi_t \sin^2 2\theta_t}{\psi_f \sin Q}\,, \tag{4.20}$$

$$M = \frac{\psi_l}{\psi_f}\cos^2 2\theta_t \cot P + \frac{\psi_t}{\psi_f}\sin^2 2\theta_t \cot Q\,, \tag{4.21}$$

$$P = k_l l \cos\theta_l, \quad Q = k_t l \cos\theta_t\,, \tag{4.22}$$

and

$$\psi_f = \rho_f c_f / \cos\theta_i, \quad \psi_l = \rho_s c_l / \cos\theta_l \quad \psi_t = \rho_s c_t / \cos\theta_t\,. \tag{4.23}$$

In Eqns. (4.20)–(4.23), ρ_f and c_f are the density and sound speed of the fluid medium, and θ_i is the angle of incidence of plane wave; ρ_s and c_l are the density and compressional sound speed of the plate, and θ_l is the angle at which the longitudinal wave propagates in the plate; c_t is the transverse sound speed in the plate, and θ_t is the angle at which the transverse wave propagates in the plate. Also, $k_l = \omega/c_l$ is the wave number of the longitudinal wave in the plate and $k_t = \omega/c_t$ is the wave number of the transverse wave in the plate. The angles θ_l and θ_t are related to θ_i through Snell's law, so V and W are determined completely by the frequency and angle of the incident wave, plus the physical parameters of the plate and surrounding fluid.

The transmission and reflection coefficients for a 1 MHz plane wave incident upon a plate of aluminum with thickness $l \approx 1/8$ in. (to be used in our experiments) are shown as a function of angle of incidence in Fig. 4.7. Parameters for the plate are given in Table A.1. Rapid changes in magnitude and phase of the transmission and reflection coefficients occur at $\theta_i \approx 0°, 12°, 15°, 27°$, and $31°$. We expect nonspecular phenomena in sound beams reflected from, and transmitted through, the plate to occur at angles of incidence near these critical angles. Comparison of Fig. 4.7 with Fig. 4.6 shows that these critical angles correspond to angles of excitation of Lamb waves. Each transmission maximum (and corresponding reflection minimum) is labeled according to its associated Lamb mode.

Figure 4.8 shows the transmission and reflection coefficients for a 2 MHz plane wave incident upon the aluminum plate. These figures show that second harmonic generated in a 1 MHz sound beam between the source and the plate will interact differently with the plate than will the sound beam at the fundamental frequency. This is not surprising, given the frequency dependence of the Lamb excitation angles shown in Fig. 4.6. Transmission is increased only slightly at $30°$ due to the presence of the pseudo-Rayleigh mode; however, there is a $360°$ phase change.

4.1.5 Linear reflection and transmission for diffracting sound beams

We calculate the reflected and transmitted fields by incorporating the appropriate function, Eqn. (4.18) or (4.19), into the angular spectrum, and propagate the resulting component plane waves to the receiver plane. Equations (4.18) and (4.19) are presented as functions of angle of incidence. In Sec. 4.1.1 we expressed propagation angle θ for a plane wave in terms of $\boldsymbol{\kappa}$, so we may also express the transmission and reflection coefficients as functions of $\boldsymbol{\kappa}$ using the relation $\sin\theta = |\boldsymbol{\kappa}|/k$. The reflected field at a distance $z = d_i + d_r$ of a sound beam with source spectrum $\widehat{P}(\boldsymbol{\kappa}, 0)$ is

$$P(\mathbf{x}, z) = \mathcal{F}^{-1}\left\{V(\boldsymbol{\kappa})\widehat{P}(\boldsymbol{\kappa}, 0)e^{-jKz}\right\}, \tag{4.24}$$

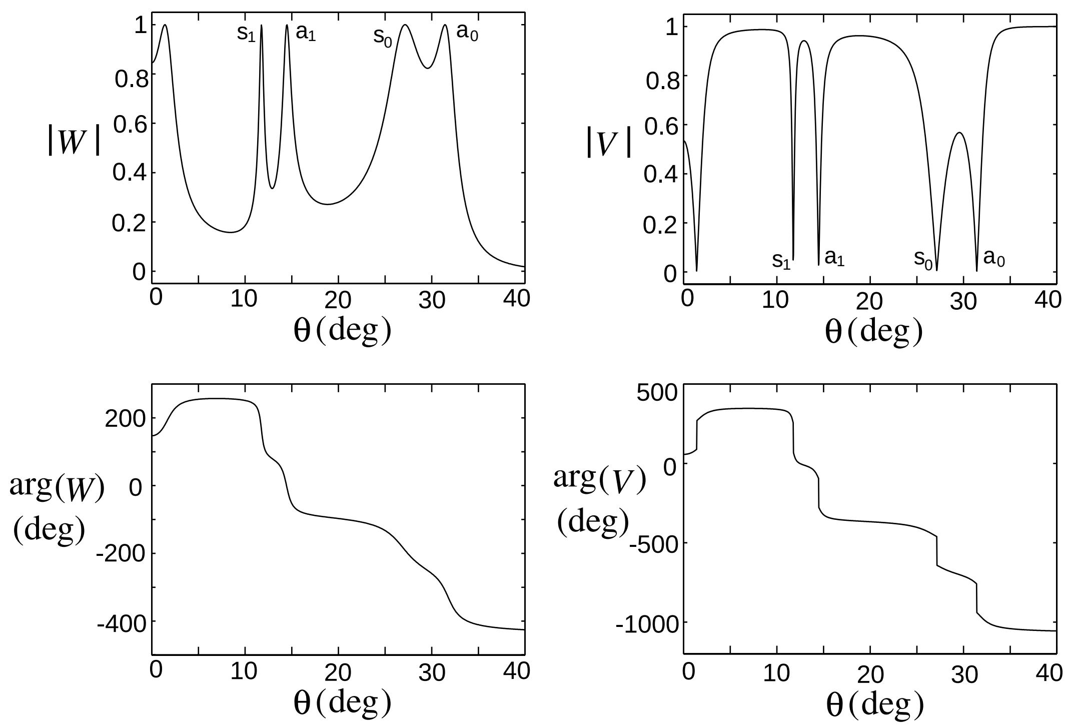

Figure 4.7: Plane-wave transmission and reflection coefficients for an aluminum plate at 1 MHz. Parameters for the plate are given in Table A.1.

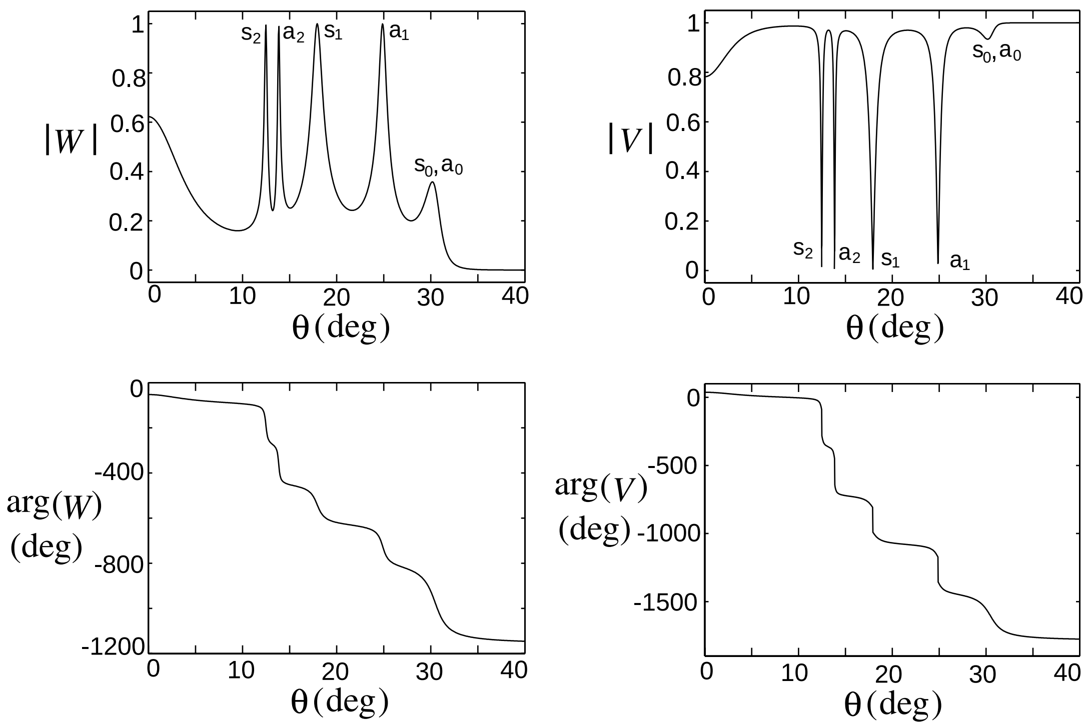

Figure 4.8: Plane-wave transmission and reflection coefficients for an aluminum plate at 2 MHz. Parameters for the plate are given in Table A.1.

and the transmitted field at $z = d_i + d_t$ is

$$P(\mathbf{x}, z) = \mathcal{F}^{-1}\left\{W(\boldsymbol{\kappa})\widehat{P}(\boldsymbol{\kappa}, 0)e^{-jKz}\right\} . \tag{4.25}$$

A characteristic of linear reflection and transmission is that the fields propagated to the receiver depend on the total source-receiver distance z, but not on d_i, d_r, or d_t individually. This can be seen from Eqns. (4.24). The physical interpretation of this result is that the distance between the source and the plate does not affect the received field, as long as the total path length from the source to the receiver is constant.

4.2 Nonlinear theory

In this section we reveiw the development by Landsberger and Hamilton[64] of equations describing the pressure field at angular frequency 2ω given the field at ω. This development assumes weakly nonlinear effects; strong effects such as shocks are not described by this model. Second harmonic is assumed to be generated only in the fluid, and interactions with the plate are assumed to occur independently for the pressure fields at the fundamental and second harmonic. For a pressure field at $z = z_0$, an expression is given that describes the field at the second harmonic at any plane $z > z_0$.

4.2.1 Wave interaction in the fluid

We model the wave interaction in the fluid using the lossless second-order wave equation for the fluid, Eqn. (2.15), generalized for wave motion in three dimensions.[64] Because we are modeling directional sound beams, the effects of the Lagrangian density are small so we set $\mathcal{L} = 0$. We apply the method of successive approximations to model the pressure at 2ω. Thus we set $p = p^{(1)} + p^{(2)}$, where $|p^{(1)}| \gg |p^{(2)}|$. Here, $p^{(1)}$ is the sound pressure at ω and $p^{(2)}$ is the sound pressure at 2ω. Doing so gives

$$\left(\nabla^2 - \frac{1}{c^2}\frac{\partial^2}{\partial t^2}\right)p^{(1)} = 0\,, \tag{4.26}$$

$$\left(\nabla^2 - \frac{1}{c^2}\frac{\partial^2}{\partial t^2}\right)p^{(2)} = -\frac{\beta}{\rho c^4}\frac{\partial^2 (p^{(1)})^2}{\partial t^2}\,. \tag{4.27}$$

We express $p^{(1)}$ and $p^{(2)}$ as

$$p^{(n)}(\mathbf{x}, z, t) = \tfrac{1}{2}P^{(n)}(\mathbf{x}, z)e^{jn\omega t} + \text{c.c.}\,, \qquad n = 1, 2\,. \tag{4.28}$$

The source condition at a plane $z = z_0$ is

$$p(\mathbf{x}, z_0, t) = \tfrac{1}{2}\left[P^{(1)}(\mathbf{x}, z_0)e^{j\omega t} + P^{(2)}(\mathbf{x}, z_0)e^{j2\omega t}\right] + \text{c.c.}\,. \tag{4.29}$$

Note that we do not set $P^{(2)}(\mathbf{x}, z_0) = 0$ in Eqn. (4.29). This way we may accommodate second-harmonic generation and propagation from planes other than the plane of the sound source.

The solution to Eqn. (4.27) for the source condition given in Eqn. (4.29) and Eqn. (4.14), is

$$P^{(1)}(\mathbf{x}, z) = \mathcal{F}^{-1}\left\{\widehat{P}^{(1)}(\boldsymbol{\kappa}, z_0)e^{-jK_1\Delta z}\right\} = \int \widehat{P}^{(1)}(\boldsymbol{\kappa}, z_0)e^{-j\mathbf{k}\cdot\mathbf{r}}\,\frac{d\boldsymbol{\kappa}}{(2\pi)^2}\,, \tag{4.30}$$

where

$$K_n = \sqrt{(nk)^2 - |\boldsymbol{\kappa}|^2}\,, \qquad n = 1, 2\,, \tag{4.31}$$

is the projection of k along the z axis; also, $\mathbf{k} = (k_x, k_y, k_z) = (\boldsymbol{\kappa}, K_1)$, $\mathbf{r} = (x, y, \Delta z) = (\mathbf{x}, \Delta z)$, and $\Delta z = z - z_0$. The homogeneous solution $P_h^{(2)}$ satisfies the Helmholtz equation $(\nabla^2 + 4k^2)P_h^{(2)} = 0$, the solution of which is, from Eqn. (4.14),

$$P_h^{(2)}(\mathbf{x}, z) = \mathcal{F}^{-1}\left\{\widehat{P}^{(2)}(\boldsymbol{\kappa}, z_0)e^{-jK_2\Delta z}\right\}\,. \tag{4.32}$$

We now find the particular solution $P_p^{(2)}$. Substituting Eqns. (4.29) and (4.30) into Eqn. (4.27) yields

$$(\nabla^2 + 4k^2)P_p^{(2)} = \frac{2\beta k^2}{\rho c^2}\iint e^{-j(\mathbf{k}'+\mathbf{k}'')\cdot\mathbf{r}}\,\widehat{P}_1(\boldsymbol{\kappa}', z_0)\widehat{P}_1(\boldsymbol{\kappa}'', z_0)\,\frac{d\boldsymbol{\kappa}'d\boldsymbol{\kappa}''}{(2\pi)^4}\,. \tag{4.33}$$

Applying Eqn. (4.1) to both sides of Eqn. (4.33), and then performing the integrals over $\mathbf{x}$ and $\boldsymbol{\kappa}''$, gives

$$\left(\frac{\partial^2}{\partial z^2} + K_2^2\right)\widehat{P}_p^{(2)} = \frac{2\beta k^2}{\rho c^2}\int e^{-j(K_a+K_b)\Delta z}\widehat{P}^{(1)}(\boldsymbol{\kappa}', z_0)\widehat{P}^{(1)}(\boldsymbol{\kappa}-\boldsymbol{\kappa}', z_0)\frac{d\boldsymbol{\kappa}'}{(2\pi)^2}\,, \quad (4.34)$$

where

$$K_a = \sqrt{k^2 - |\boldsymbol{\kappa}'|^2}\,, \qquad K_b = \sqrt{k^2 - |\boldsymbol{\kappa}-\boldsymbol{\kappa}'|^2}\,. \quad (4.35)$$

The solution of Eqn. (4.34) is

$$\widehat{P}_p^{(2)}(\boldsymbol{\kappa}, z) = \int Q_f(\boldsymbol{\kappa}, \boldsymbol{\kappa}', \Delta z)\widehat{P}^{(1)}(\boldsymbol{\kappa}', z_0)\widehat{P}^{(1)}(\boldsymbol{\kappa}-\boldsymbol{\kappa}', z_0)\frac{d\boldsymbol{\kappa}'}{(2\pi)^2}\,, \quad (4.36)$$

where

$$Q_f(\boldsymbol{\kappa}, \boldsymbol{\kappa}', \Delta z) = \frac{2\beta k^2}{\rho c^2}\left(\frac{e^{-j(K_a+K_b)\Delta z} - e^{-jK_2\Delta z}}{K_2^2 - (K_a+K_b)^2}\right)\,. \quad (4.37)$$

Equation (4.36) satisfies the condition that $P^(2)_p(\mathbf{x}, z_0) = 0$. The pressure at frequency 2ω is the sum of the homogeneous and particular solutions,

$$P^{(2)}(\mathbf{x}, z) = \mathcal{F}^{-1}\left\{\widehat{P}^{(2)}(\boldsymbol{\kappa}, z_0)e^{-jK_2\Delta z} + \widehat{P}_p^{(2)}(\boldsymbol{\kappa}, z)\right\}\,. \quad (4.38)$$

4.2.2 Reflection and transmission at second-harmonic frequency

We first consider the reflection of a sound beam from a plate. The condition at second order at the plane of the source, $z = 0$, is that $P^{(2)}(\mathbf{x}, 0) = 0$. The pressure field at the second harmonic at the receiver ($z = z_r$) is[64]

$$P_r^{(2)}(\mathbf{x}, z_r) = \mathcal{F}^{-1}\{\widehat{P}_{r,\mathrm{inc}}^{(2)}(\boldsymbol{\kappa}, z_r) + \widehat{P}_{r,\mathrm{refl}}^{(2)}(\boldsymbol{\kappa}, z_r)\}\,, \quad (4.39)$$

where

$$\widehat{P}_{r,\mathrm{inc}}^{(2)}(\boldsymbol{\kappa}, z_r) = V(\boldsymbol{\kappa})\widehat{P}_p^{(2)}(\boldsymbol{\kappa}, d_i)e^{-jK_2 d_r} \quad (4.40)$$

is the contribution to the second harmonic at z_r due to the second harmonic generated by the sound beam at the fundamental before reflection from the plate. The quantity $P_p^{(2)}(\boldsymbol{\kappa}, d_i)$ is defined in Eqn. (4.36), with $z_0 = 0$ and $\Delta z = d_i$. Also,

$$\widehat{P}_{r,\mathrm{refl}}^{(2)}(\boldsymbol{\kappa}, z_r) = \int Q(\boldsymbol{\kappa}, \boldsymbol{\kappa}', d_r)\widehat{P}_r^{(1)}(\boldsymbol{\kappa}', d_i)\widehat{P}_r^{(1)}(\boldsymbol{\kappa}-\boldsymbol{\kappa}', d_i)\frac{d\boldsymbol{\kappa}'}{(2\pi)^2} \quad (4.41)$$

is the contribution to the second harmonic at z_r generated by the sound beam at the fundamental after reflection from the plate.

It is straightforward to modify Eqns. (4.39)–(4.41) to model transmission through the plate. To do so we replace $V(\boldsymbol{\kappa})$ with $W(\boldsymbol{\kappa})$, and d_r with d_t.

4.2.3 Absorption

Thermoviscous attenuation is accounted for *ad hoc*. In the fluid, we render the wave number $K = k_z$ complex because the sound beam is propagated in the z coordinate. Hence we replace K with $\tilde{K}$, where

$$\tilde{K} = K - j\alpha_z \,. \tag{4.42}$$

As illustrated in Fig. 4.9, for a plane wave propagating at angle θ_z propagates a distance $\Delta z / \cos\theta_z$. Because the propagation operation acts along the z axis, the effective absorption coefficient is α_z, defined as

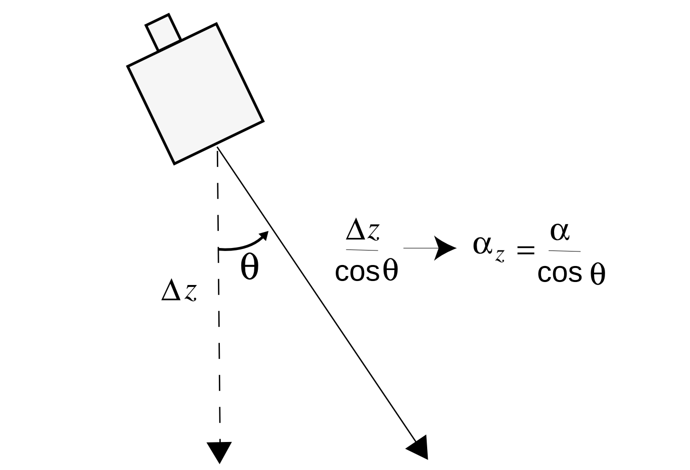

Figure 4.9: Absorption coefficient for a plane wave propagating with angle θ from normal incidence.

$$\alpha_z = \alpha / \cos\theta_z \,. \tag{4.43}$$

Values for α at 1 and 2 MHz are given in Table A.1.

Absorption in the plate may also be taken into account. However, because aluminum has a fairly low absorption coefficient at the frequencies of interest, and the plate is thin, the effects of absorption in the plate are small and are neglected in our model.

4.2.4 Numerical evaluation

Numerical evaluation of the equations that describe the pressure field at the receiver plane in wave vector space is performed by discretizing the variable $\boldsymbol{\kappa} = (k_x, k_y)$. Continuous integrals are approximated as summations over the discrete values of k_x and k_y such that, for the integral of some function F,

$$\int\int F(k_x, k_y) dk_x dk_y \rightarrow \sum_{i=i_{\min}}^{i_{\max}} \sum_{j=j_{\min}}^{j_{\max}} F(i\Delta k_x, j\Delta k_y) \Delta k_x \Delta k_y. \tag{4.44}$$

Transformations from (k_x, k_y) to (x, y) and vice-versa are accomplished using a two-dimensional Fast Fourier transform algorithm.

Approximation of the Fourier integrals as discrete sums results in the introduction of two parameters for each variable of integration. These parameters are the number of summation points and the spacing between points (Δx for the variable x). We choose values of Δx and Δy on the order of 1 mm, which is small enough that the fine structure of the reflected and transmitted fields is modeled accurately. Once Δx and Δy are chosen, the number of summation points must be large enough to avoid aliasing. This aliasing is a consequence of the approximation of the Fourier integrals by discrete sums, which causes the pressure field to be repeated periodically in (x, y) space. If too few summation points are used, the repeated pressure fields will overlap the desired pressure field, resulting in error. For most of our calculations, 512 points in each dimension was sufficient to model the pressure fields accurately.

Calculation of the angular spectrum for the second harmonic field involves discretizing Eqn. (4.36) in the manner described by Eqn. (4.44). This results in an equation of the form

$$\widehat{P}_p^{(2)}(m\Delta k_x, n\Delta k_y) = \sum_{i=i_{\min}}^{i_{\max}} \sum_{j=j_{\min}}^{j_{\max}} F(m\Delta k_x, n\Delta k_y, i\Delta k'_x, j\Delta k'_y)\Delta k'_x \Delta k'_y \,, \quad (4.45)$$

where m and n are integers. Determining the complete angular spectrum $\widehat{P}_p^{(2)}$ thus requires summation over the indices i, j, m, and n, which becomes prohibitively computationally intensive when enough points are used to model accurately the sound fields under investigation in this chapter. In practice, the sums over indices i and j for a given component $\widehat{P}_p^{(2)}(m\Delta k_x, n\Delta k_y)$ are limited to points within about 10° of the direction of $(m\Delta k_x, n\Delta k_y)$. The error that results from truncating these sums is small, because the nonlinear interaction of plane waves is weak at large angles. In addition to truncating the sums, the number of calculations needed to model the sound field is halved by exploiting symmetry about the y axis.

4.3 Experimental results

Reflection and transmission experiments were performed using a plane piston source, with source radius $a = 1.22$ cm, operating at 1 MHz, and with a source pressure $p_0 = 100$ kPa. The source, plate, and receiver were immersed in fresh, deionized water. Details of the apparatus are given in App. A. The goal of the experiments was to measure accurately the reflection and transmission of a sound beam incident obliquely upon a 1/8 in. aluminum plate. Pressure was measured at the fundamental and second harmonic frequencies.

We compare experimental results with predictions made using the model described in the previous sections. We have found that, although the material parameters that produce the best match between experiment and theory vary by a few percent from angle to angle (for which different portions of the plate are interrogated), the parameters that give the best match between theory and experiment over all angles are given in Table A.1.

Figures 4.10–4.14 show the transmitted pressure field along the x axis as the angle θ_0 of the beam axis with respect to normal is varied. Measurements in Figs. 4.10 and 4.11 were made using a PVDF needlepoint hydrophone, and all other measurements were made using a PVDF membrane hydrophone. The source and receiver were both positioned at $d_i = d_t = 150$ mm from the plate. Experimental results are compared with theoretical predictions. In these plots $x = 0$ cm corresponds to the location of the axis of the sound beam in the absence of the plate, predicted using ray theory. Measurements of the fundamental and second harmonic are in good qualitative and quantitative agreement with theory. At normal incidence the transmission coefficient is close to unity, as seen in Fig. 4.7. The magnitude of the transmission coefficient drops rapidly as θ increases from $0°$ to $9°$. Measurements over these angles are taken at approximately every $2°$ because the transmission is very small and W changes slowly through most of this range of angles. For angles from $11°$ to $32°$, W changes rapidly, so measurements are taken at every degree.

Because 1 MHz is nearly a pass band for a 1/8 in. aluminum plate, the magnitude of the transmitted pressure at the fundamental is large at normal incidence. One feature of note in the transmitted pressure at the fundamental at $\theta_0 = 0°$ is that the sidelobes are about 5 dB lower with respect to the main lobe than they are for a sound beam in the farfield with no plate. The magnitude of the second harmonic is large as well, because the second-harmonic frequency is also near a pass band for the plate. Discrepancies between theory and measurement are probably the result of small differences between the material parameters for the plate and the parameters in the model.

From normal incidence to $9°$ the transmitted pressure drops by an order of magnitude. Although the beam pattern for the transmitted pressure at $9°$ is heavily distorted, especially at the fundamental, theory is in agreement with measurement. A null in the transmitted field at the fundamental is observed at $12°$. This corresponds to the excitation of the s_1 mode. However, the excitation of the a_1 mode near $15°$ does not lead to strong nonspecular effects. Some of the strongest nonspecular transmission phenomena at the fundamental occur between $20°$ and $25°$. Figure 4.7 indicates that there is no Lamb excitation angle in this range. The magnitude of the transmitted sound beam increases steadily

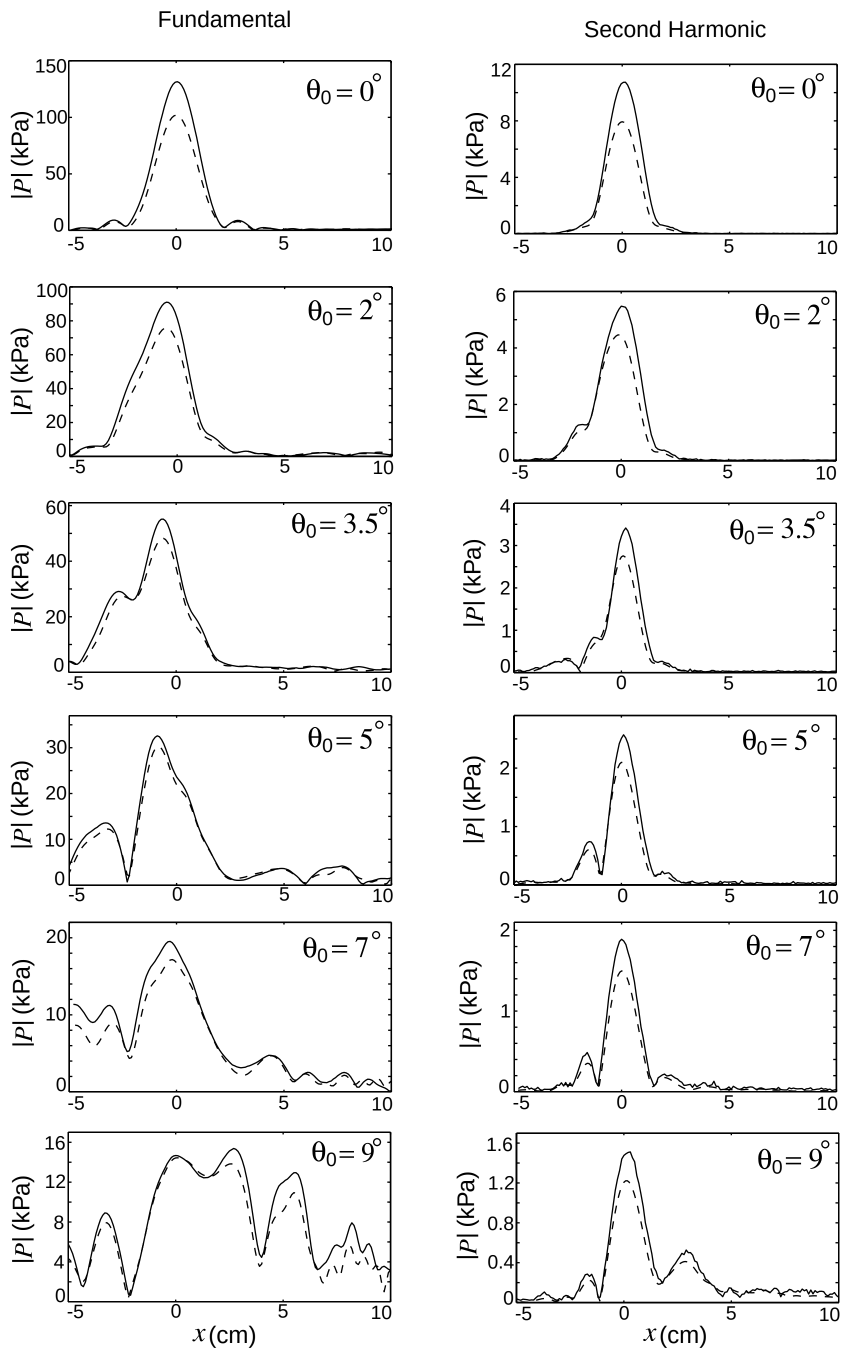

Figure 4.10: Transmission through 1/8 in. aluminum plate, $d_i = d_t = 150$ mm, from $\theta_0 = 0^\circ$ to $\theta_0 = 9^\circ$. Source used is a plane piston, $a = 1.22$ cm, $p_0 = 100$ kPa.

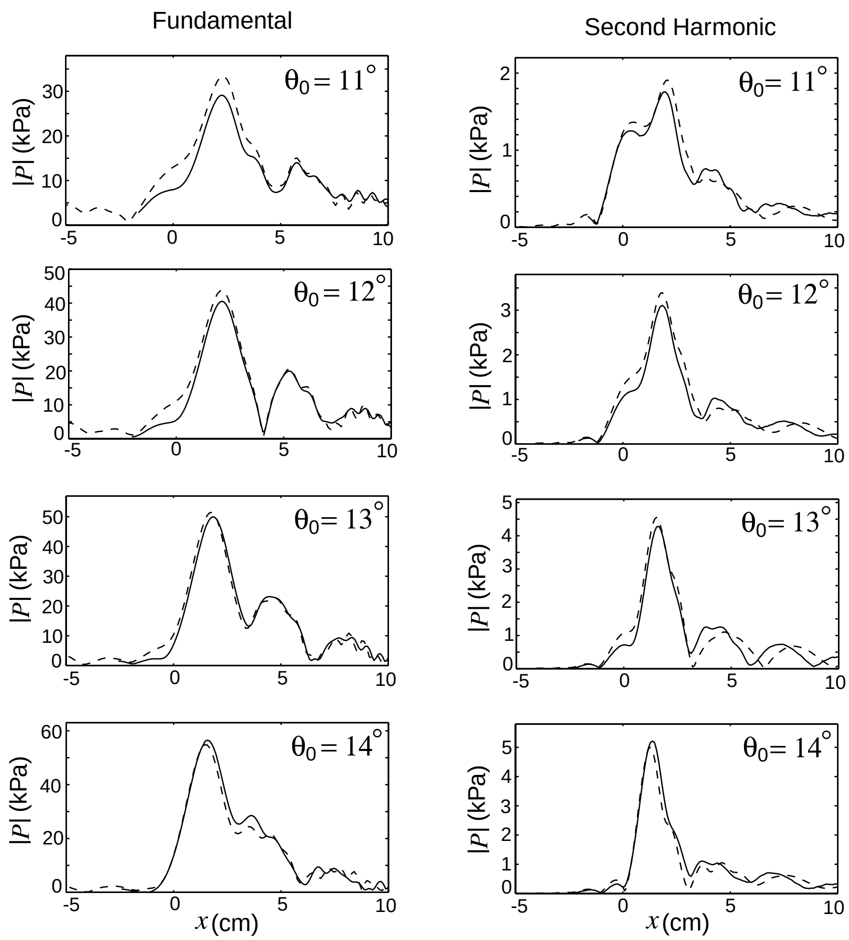

Figure 4.11: Transmission through 1/8 in. aluminum plate, $d_i = d_t = 150$ mm, from $\theta_0 = 11°$ to $\theta_0 = 14°$.

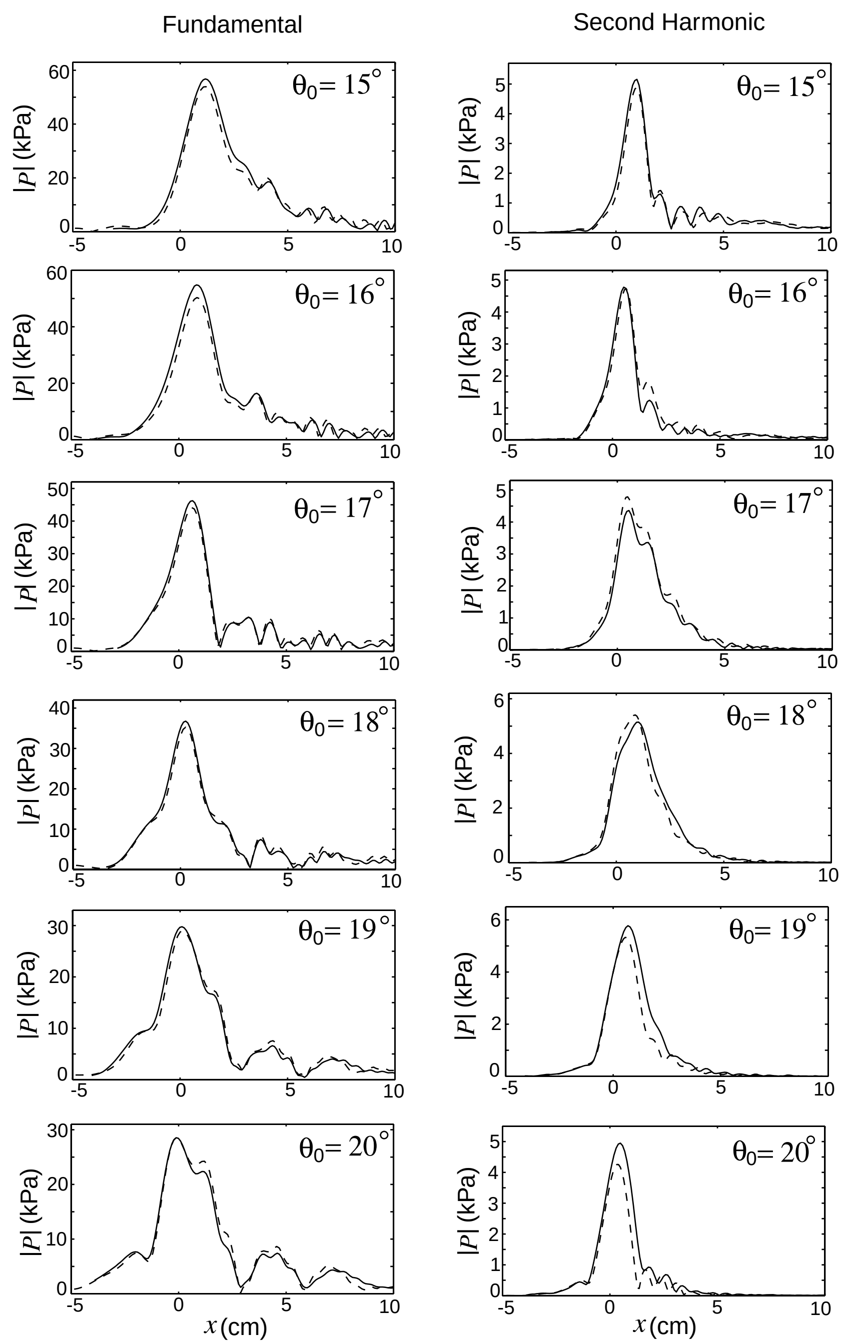

Figure 4.12: Transmission through 1/8 in. aluminum plate, $d_i = d_t = 150$ mm, from $\theta_0 = 15°$ to $\theta_0 = 20°$.

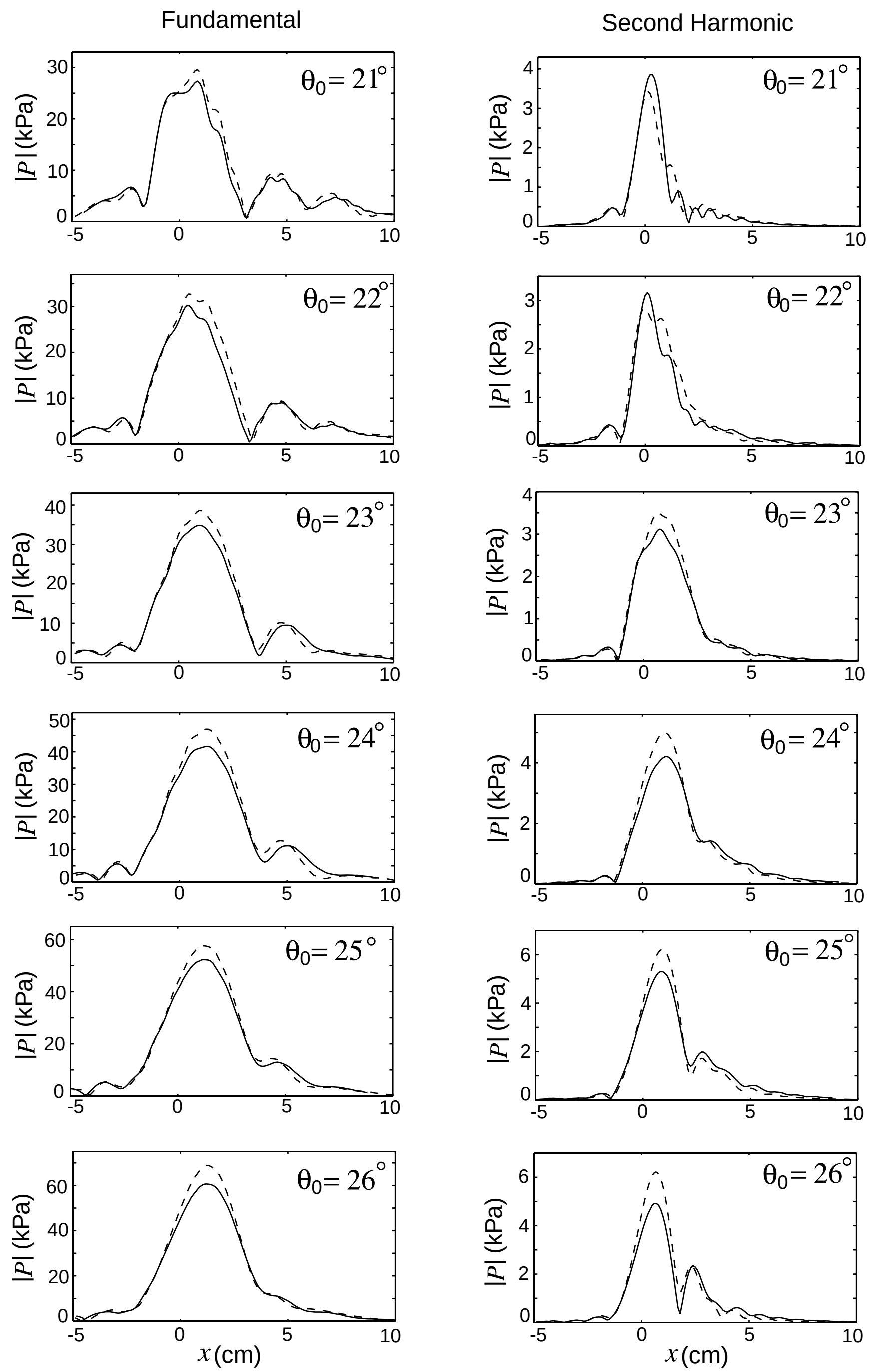

Figure 4.13: Transmission through 1/8 in. aluminum plate, $d_i = d_t = 150$ mm, from $\theta_0 = 21°$ to $\theta_0 = 26°$.

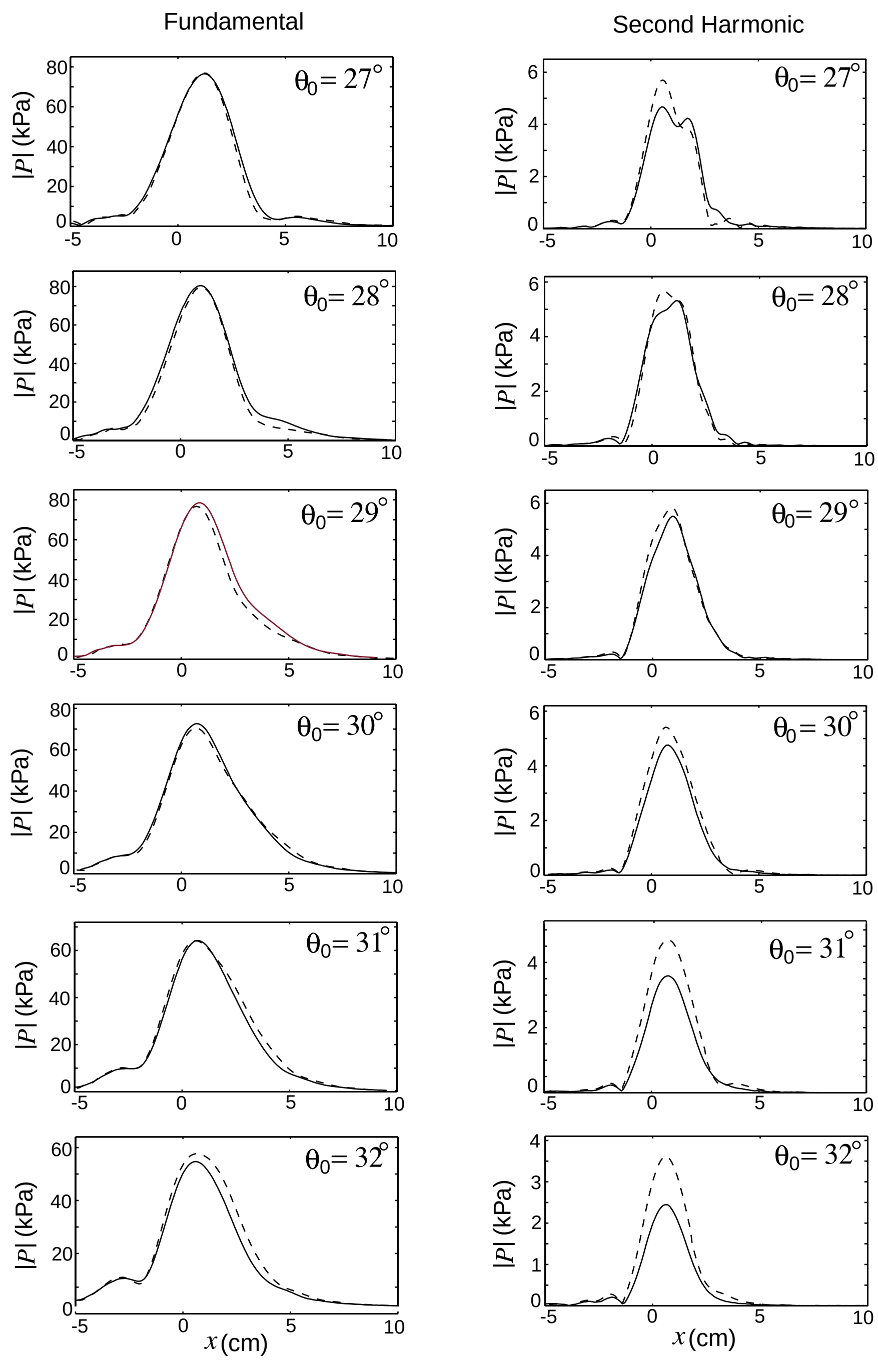

Figure 4.14: Transmission through 1/8 in. aluminum plate, $d_i = d_t = 150$ mm, from $\theta_0 = 27°$ to $\theta_0 = 32°$.

over this range of anlges. Changes in W over that range of angles due to the a_0 mode are apparently the cause of the distortion of the beam pattern. The corresponding reflection of the fundamental from 21° to 25°, shown in Fig. 4.15, does not exhibit significant beam distortion. Above 27° there are no more nulls in the transmitted sound beam at the fundamental, even though the a_0 mode is excited near 31°.

The transmitted and reflected fields at the second harmonic are more complicated than those at the fundamental frequency. For the second harmonic field there are two potential causes of nonspecular effects. First, the second harmonic generated after interaction with the plate is subject to the changes in the field at the fundamental frequency, which is dictated by the reflection and transmission coefficients at that frequency. Second, the second harmonic generated before interaction with the plate is itself subject to nonspecular phenomena associated with transmission through, or reflection from, the plate. In this latter case, the transmission and reflection coefficients at the second harmonic frequency dictate the interaction.

Of particular interest in the transmitted second harmonic is near 26°. As shown in Fig. 4.13, a well-defined null is present in the transmitted beam pattern. This corresponds to excitation of the a_1 mode by the second harmonic, shown in Fig. 4.8, and also to the excitation of the a_1 mode by the fundamental at 27°. There is a corresponding transmission maximum at the fundamental; however, this maximum extends over a few degrees. This result implies that, in certain cases, the second harmonic may provide clearer information than the fundamental when determining Lamb wave excitation angles.

As θ_0 approaches 32°, theory for the second harmonic amplitude significantly overestimates the measurement. Figures 4.7 and 4.8 indicate that the transmission coefficients at the fundamental and second harmonic frequencies rapidly approach zero after 30°. Small deviations in the material parameters of the plate, such as local fluctuations in thickness, may affect this behavior strongly.

Figures 4.15 and 4.16 show reflected fields. Because the source and its mounting hardware disturb the reflected field at small angles, only reflection at larger values of θ_0 could be measured. The receiver was positioned at $d_r = 300$ mm from the plate in order to keep it out of the way of the source, which was positioned at $d_i = 150$ mm. In general, nonspecular effects are stronger for the reflected fields than for the transmitted fields. Near $\theta_0 = 25°$ the reflected field at the fundamental frequnency is mildly distorted; however, the second harmonic field displays very strong interference phenomena corresponding to the presence of the a_1 mode. Figures 4.7 and 4.8 show that 25° is a Lamb angle at the second harmonic, so that small changes in incident angle translate to large differences in reflection. Changes in the reflection coefficient with angle of incidence near 25° are more gradual at the fundamental frequency. In general, very strong nonspecular effects occur between 27° and 31°. At 29° nonspecular effects due to Lamb angles at 27° and 31° combine.

The reflected and transmitted pressure fields are very sensitive to small variations in the parameters of the plate. Variations on the order of a few percent have a very strong effect on the results. Because the measurements were not made all at once, different portions of the plate were irradiated for measurements made at different values of θ_0. It is probable that there is some variation in the material properties over the expanse of the plate, because theory may be matched almost perfectly with experiment for any individual measurement by varying the values of the material constants in the code by a few percent. This is illustrated in Fig. 4.17. By varying in the calculations the shear sound speed c_t by about one percent, and the thickness l by about five percent, from their nominal values, theory may be matched closely with measurement for the reflected sound beam at $\theta_0 = 30°$. At other angles, however, these values for the parameters of the plate will lead to large discrepancies between theory and measurement.

4.3.1 Discussion

Comparison of theory with measurement shows that our model predicts accurately the reflection and transmission of a sound beam incident upon an isotropic plate at the fundamental and second harmonic frequencies. Although the received second harmonic depends on the interaction of the sound beam with

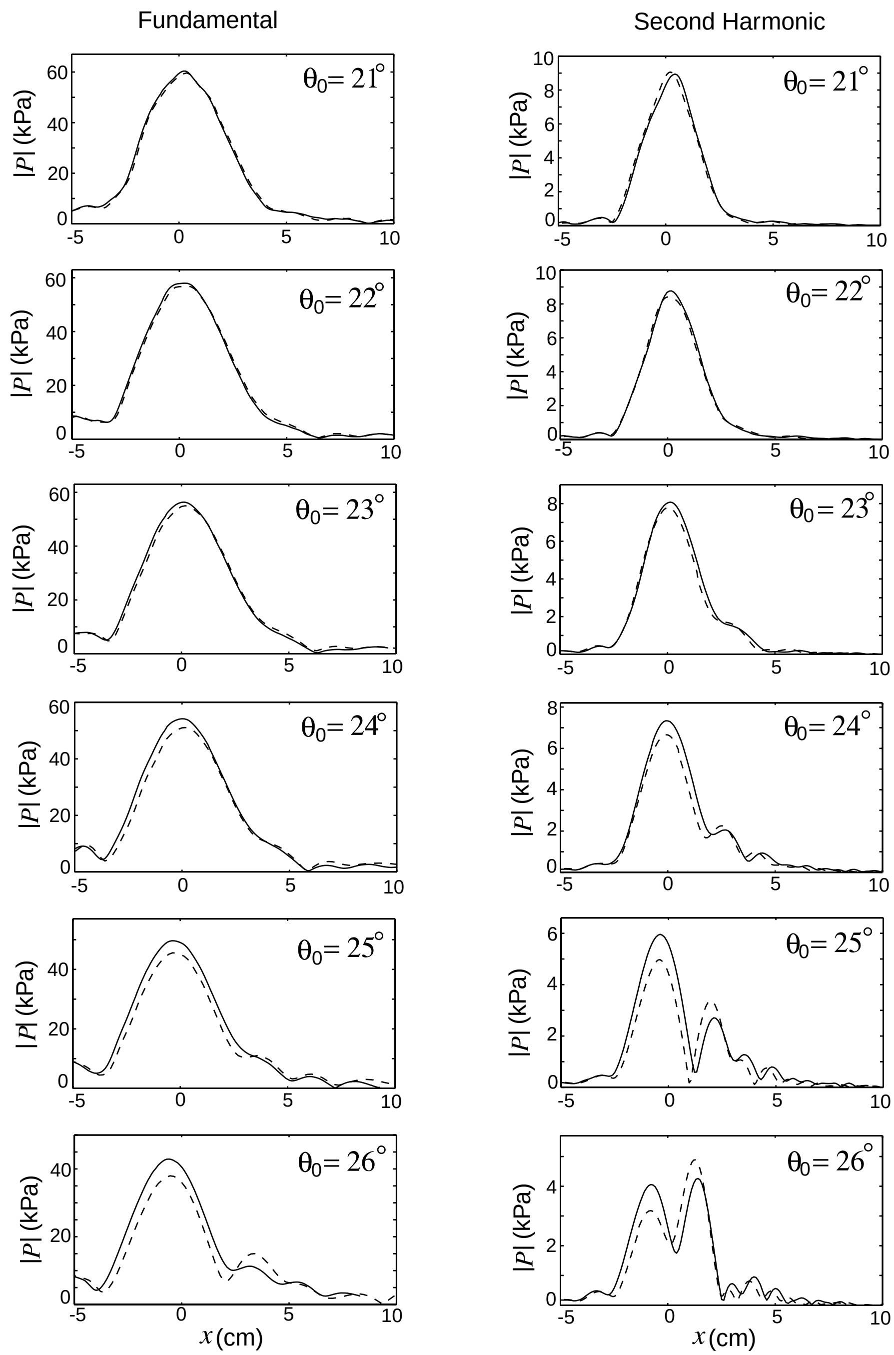

Figure 4.15: Reflection from 1/8 in. aluminum plate, $d_i = 150$ mm, $d_r = 300$ mm, from $\theta_0 = 21^\circ$ to $\theta_0 = 26^\circ$.

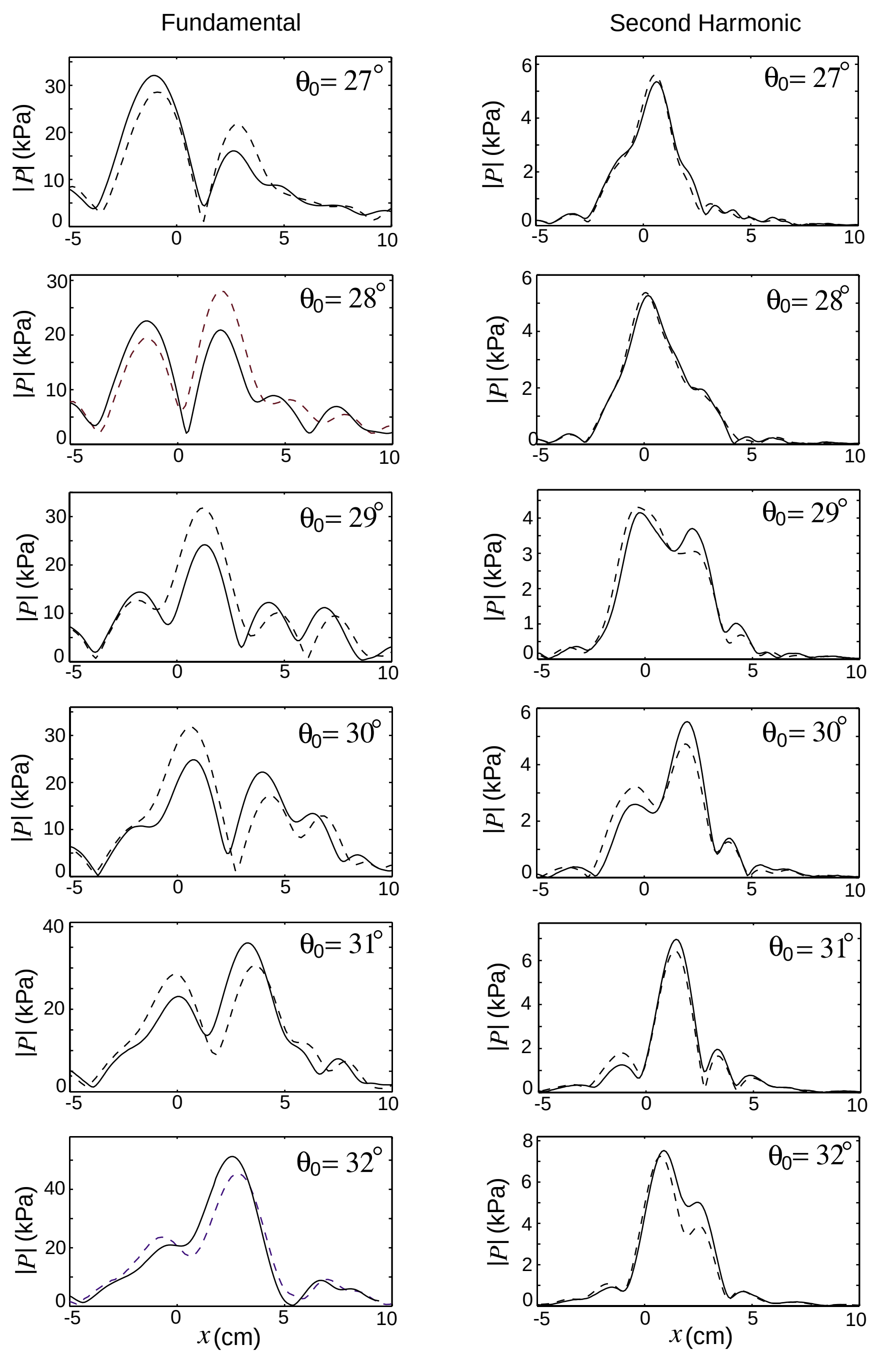

Figure 4.16: Reflection from 1/8 in. aluminum plate, $d_i = 150$ mm, $d_r = 300$ mm, from $\theta_0 = 27°$ to $\theta_0 = 32°$.

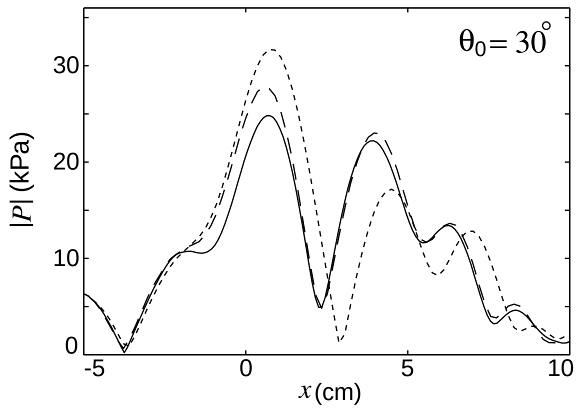

Figure 4.17: Comparison of measurement (solid) with theory for the reflected sound beam at $\theta_0 = 30°$. Parameters are $\rho = 2727$ kg/m^3, $c_l = 6317$ m/s, $c_t = 3128$ m/s, and $l = 3.048$ mm (short dash), and, from Table A.1, $\rho = 2727$ kg/m^3, $c_l = 6317$ m/s, $c_t = 3163$ m/s, and $l = 3.191$ mm (long dash).

the plate at both f and $2f$, our results (for example, the reflected pressure at $\theta_0 = 25°$, shown in Fig. 4.15) suggest that the measured second harmonic can be used to determine the excitation angle for some Lamb modes at frequency $2f$.

The reflection and transmission coefficients used in our model, while exact, do not allow us to examine the effects of different Lamb modes seperately from one another. However, as long as other transmission and reflection coefficients can be expressed as functions of $\boldsymbol{\kappa}$ it is straightforward to substitute them into our model. Approximate expressions that expand the reflection and transmission coefficients as a sum of resonance terms corresponding to the excitation Lamb modes, such as those developed by Fiorito et al.,[48] could be used to explore the effects of individual Lamb modes.

Chapter 5

SUMMARY AND CONCLUSIONS

This dissertation reports an investigation of the interaction of ultrasound with layers and plates. Both theoretical and experimental work are reported. Models were developed that describe the interaction of ultrasound with plates, and then those models were evaluated experimentally. Effects of weak nonlinearity were included in the models, and measurements included amplitudes of the second (and sometimes third) harmonics. In Chaps. 2 and 3 we considered the interaction of plane waves with plates at normal incidence. In Chap. 4 we considered diffracting sound beams obliquely incident upon plates.

This work was motivated by studies in the field of acoustic nondestructive testing. Ultrasonic inspection has long proved to be a useful method for probing a sample's characteristics. Traditional ultrasonic inspection techniques utilize the linear propagation characteristics of the sound in the structure. Several recent investigations indicate that fatigue and damage of a material cause changes in the nonlinear parameters of the material, which can be orders of magnitude larger than the changes in the linear parameters. For this reason, nonlinear acoustic techniques for nondestructive evaluation have potential advantages over linear techniques.

In Chap. 2 we presented theory and measurements for the second harmonic and sum frequency pressures generated nonlinearly in, and radiated from, an isotropic elastic layer. We first attempted to measure the nonlinearity of the layer by measuring the second harmonic propagating back towards the source upon interaction with the plate. Diffraction effects in the sound beam cause reflections in the incident sound beam, even at pass-band frequencies. The second harmonic generated in the fluid and reflected from the plate could not be distinguished from the second harmonic generated in the plate and radiated back from the source. An alternative configuration was studied, in which two sound beams with different source frequencies were normally incident upon the plate from opposite directions. Nonlinear effects arising in the plate could not be identified because the nonlinear generation occurred primarily in the fluid. Also, diffraction effects in the sound beam were strong enough that the plane-wave model was inadequate to describe the interaction.

In Chap. 3 the interaction of ultrasound with two plates meeting at a compliant, nonlinear boundary was investigated. Theory was presented that predicted both the linear and nonlinear response of a defective plate to a normally-incident plane wave. The linear behavior was observed qualitatively in the measurements. As the contact boundary increased in compliance, changes were predicted theoretically and observed experimentally in the reflection and transmission coefficients. Higher harmonic generation at the contact boundary was not observed in our experiments; rather, all observed higher harmonic generation was attributable to nonlinear effects in the fluid. One linear effect caused by the inclusion of a compliant boundary between the plates is the shifting of pass-band frequencies. If the incident sound beam contains significant harmonics, reflection and transmission of those harmonics will be disproportionate because of this shifting of resonance frequencies. For this reason care must be taken when attempting to measure the nonlinearity of a plate not to confuse effects of linear resonance shifting with nonlinear harmonic generation in the plate.

In Chap. 4 the reflection and transmission of a sound beam at oblique incidence upon a homogeneous, isotropic plate was examined theoretically and experimentally. Effects of diffraction, absorption, and weak nonlinearity are included in the model. Diffraction in the sound beam is modeled using a Fourier spectrum technique, in which the sound beam is represented as the superposition of plane waves propagating in different directions. Second harmonic generation in the fluid is taken into account using a model that is based on the analytic solution for harmonic generation by pairs of noncollinear plane waves. The second harmonic generated by each pair of plane waves is superposed numerically to give the total second harmonic at the target plane. The theoretical model is fully three-dimensional. All effects of interaction of the sound beam with the plate, including the excitation and propagation of leaky Lamb waves, are taken into account in the plane-wave reflection and transmission coefficients. Quantitative agreement was found between theory and experiment at the fundamental and second harmonic frequencies. Theoretical predictions indicate that the reflected and transmitted sound fields are very sensitive to variations in the material parameters of the plate.

One situation not examined in this dissertation is the reflection and transmission of ultrasound through anisotropic and inhomogeneous plates, such as composites and laminates. Such an investigation may prove valuable, considering the increasing use of these materials. The theory described in Chap. 4 could be adapted readily to accommodate such materials.

The overarching goal of this work was to explore practical arrangements for using ultrasound for evaluating immersed plates, with an emphasis placed on nonlinear effects. In Chap. 2 we found that, contrary to our motivating hypothesis, the nonlinear generation of second harmonic in an isotropic plate was not significantly enhanced by resonance effects. Also, diffraction effects and nonlinearity in the sound beam were strong enough to obscure the second harmonic generated in the plate, even under the best circumstances we could devise. Work by a number of authors indicated that harmonic generation in the plate could be enhanced by introducing contact nonlinearity. As reported in Chap. 3, we attempted to observe this enhanced harmonic generation but were unable to do so. One explanation for this is that most other authors used optically polished samples that were pressed together, and typically excited the samples using contact transducers. We chose to examine immersed, weakly bonded samples because we felt this arrangement had the potential to be particularly useful for industrial applications. Also, the use of contact transducers on the plates would have disturbed resonances excited in the plate. However, any anomalous nonlinearity generated in our experiments because of weak bonding was obscured by the nonlinearity generated in the sound beam as it propagated in the water.

Although nonlinear effects were not observed in the plates, we obtained some results that are potentially useful. Observations of the linear reflection and transmission coefficients of plates with planar, spring-like boundaries, described in Chap. 2, are potentially useful for estimating the bond strength between two joined plates. Also, the experiments reported in Chap. 4 are in good agreement with theory. The beam patterns of the reflected and transmitted sound beam are quite sensitive to the material parameters of the plate, and as such can be used to characterize the sample.

Appendix A

Experimental Apparatus

All measurements reported in this dissertation were made at the Ultrasonics Laboratory in the Mechanical Engineering Department of The University of Texas at Austin. Details of the apparatus are given by Averkiou,[75] TenCate,[76] and Landsberger.[77] This appendix includes information from their descriptions.

A.1 Tank and positioning system

The heart of the ultrasonics laboratory is the immersion tank. The walls of the tank are 1/2 in. thick glass panes with dimensions 0.9 m $\times$ 0.9 m $\times$ 1.5 m. The tank is filled with filtered, degassed, deionized water. Although there is no temperature control for the tank, the temperature is monitored continuously during testing and the room is kept at approximately 21°C by the climate control system of the building. The position of either the source or the receiver is computer controlled with high precision. The positioning system has a 20 μm readout resolution along the x and y axes, an 8 μm resolution along the z axis, and 0.002° angular resolution in rotation about the vertical axis. The apparatus is controlled by a Macintosh computer running LabVIEW by National Instruments. Photographs of the laboratory and the tank are shown in Figs. A.1 and A.2, respectively. These photographs are repeated from the dissertation by Landsberger.[77]

A.2 Laboratory equipment

A.2.1 Sources

The sources used in our measurements were piezoelectric immersion transducers made by Panametrics Inc. Source diameters were 1 in. and 1.5 in., with resonance

Figure A.1: Photograph of the ultrasonics laboratory (after Landsberger).

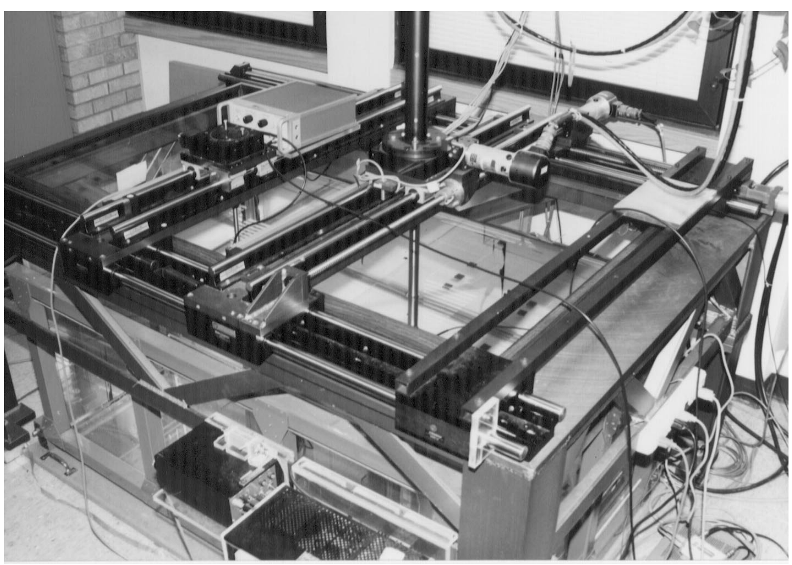

Figure A.2: Photograph of water tank with positioning apparatus (after Landsberger).

frequencies of 1 MHz and 2.25 MHz. Both focused and plane piston sources were used.

Calibration of the experimental apparatus is performed by exploiting the nonlinear propagation of a sound beam in water, which can be modeled with high accuracy. The only assumption is that the response of the hydrophone is flat between the fundamental and second harmonic frequencies. In the supplied calibration information, Marconi states that, between 1 MHz and 2 MHz, the response of the membrane hydrophone is flat to within 0.5 dB. Source pressure of the sound beam is determined by matching measurements of the sound field in water with theory at the fundamental and second harmonic. Because the coefficient of nonlinearity for fresh water at room temperature is known to be $\beta = 3.5$,[78] the source pressure may be determined.

Experimental measurements of the sound beam were matched to numerical solutions of the KZK equation for a circular, plane piston source[79] and for a circular, focused piston source.[80] As an example, comparison between theory and experiment for a 1 MHz, 1 in. diameter plane piston source is shown in Fig. A.3. Source pressure is determined to be 97.5 kPa for an input of 39.8 volts to the source. The measured source radius is $a = 1.225$ cm, which is slightly less than the manufacturer's specification of $a = 1.27$ cm. The small differences between theory and measurement may be the result of a slight nonuniformity in the pressure distribution at the piston face.

A.2.2 Hydrophones and preamplifiers

The hydrophone used in most of our measurements is a PVDF membrane hydrophone made by GEC-Marconi. The hydrophone, shown in Fig. A.4, is made of a thin membrane stretched out onto a rigid hoop (like a drum head). The active element, with a diameter of 1 mm, is at the center of the membrane. The membrane is approximately impedance matched to the water, such that the transmission loss at 2.25 MHz is approximately 0.5 dB.[75] The distance from the active element to the hoop is 50 mm, and as a result an incident tone burst

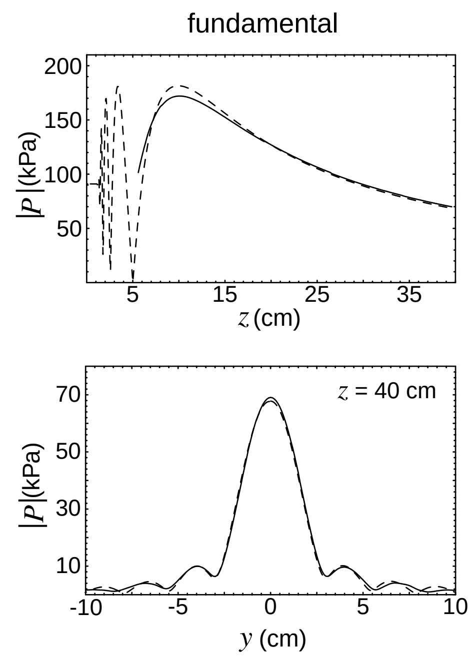

Figure A.3: Axial propagation curve and beam pattern at $z = 40$ cm for a plane piston source, $f = 1$ MHz, $p_0 = 97.5$ kPa and $a = 1.225$ cm. Theory (- -) vs. experiment (—) at the fundamental (left) and second harmonic (right).

should be limited to about 30 μs in duration in order to avoid contamination due to reflections from the hoop.

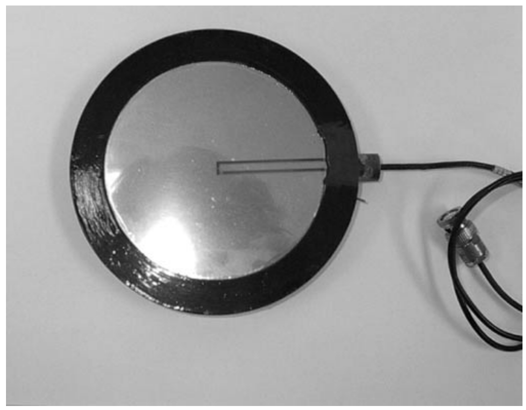

Figure A.4: Photograph of the PVDF membrane hydrophone used for most experiments.

Directionality of the membrane hydrophone was measured by Landsberger[77] at 1 MHz and 2 MHz. The hydrophone response was found to be flat to within approximately 1 dB at both frequencies for angles of incidence within 5° of normal incidence. For the measurements made in this dissertation we keep the membrane hydrophone as close as possible to normal with the incident sound beam, usually within a few degrees.

For some measurements an NTR-TNU001A (NP-1000) PVDF membrane, needlepoint hydrophone was used. The active element is 0.5 mm in diameter. This hydrophone was used when we needed to receive signals of longer than about 30 μs duration. A styrofoam shroud was constructed to deflect the incident sound field away from the needle body, which caused interference with the field measured at the active element. The needlepoint hydrophone was used in situations where the sound field needed to be measured for durations longer than 30 μs from the first arrival at the hydrophone.

The hydrophones were connected to an EG&G model 115 wideband preamplifier. The preamplifier had two fixed settings of either 20 or 40 dB of gain. The input impedance of the preamplifier was either 50 Ω or 1 MΩ, and the output impedance was 50 Ω. Connecting the preamplifier output to a high impedance oscilloscope or digitizer input gives an additional 6 dB of gain, but no adverse effects due to the large impedance mismatch were observed.

A.3 Signal generators and amplifiers

Waveforms used in this research were generated by an HP 3314A function generator and by a LeCroy model 112 arbitrary function generator. The HP was used for most situations because of its simplicity, especially when changing frequencies. The LeCroy function generator was used when source waveforms needed to be windowed, or two signals were generated at once. The function generators were computer-controlled via a GPIB connection to the Macintosh computer running LabVIEW. Signals from the function generators were amplified using ENI power amplifiers. An ENI model 2100L RF amplifier providing 55 dB of gain was used for all measurements involving a single source. When two sources were used, an ENI model 240L, which provides 50 dB of gain, was used to drive the second source.

A.4 Material Characteristics

Material constants for the plates used in this dissertation are given in Table A.1. Parameters given are velocities for longitudial waves c_l and transverse waves c_t, density ρ, coefficient of nonlinearity β, plate thickness l, and absorption α. Most of the measurements were made using an aluminum plate with thickness $l = 3.048$ mm ($\approx 1/8$ in.). Some measurements were made using bonded 1/16 in. thick aluminum plates, and bonded 0.093 in. (2.362 mm) thick acrylic plates. (This is a standard thickness for acrylic plates.)

Material constants used for aluminum (except for β) were determined in our laboratory. The coefficient of nonlinearity β for longitudinal waves in aluminum was derived using Eqn. (2.16), and measurements for the third-order elastic constants which were reported by Landolt-Bornstein.[81] Material constants used in this work for acrylic were reported by Landsberger and Hamilton[64] and Landsberger.[77]

Although no experiments were performed using steel plates, predictions of transmission, reflection, and second harmonic radiation involving steel plates are given in Secs. 3.1.4 and 3.2.4. For these predictions, the material constants used were taken from Kinsler *et al.*.[82]

Material	c_l (m/s)	c_t (m/s)	ρ (kg/m^3)	β	l (mm)	α_l 1 MHz (Np/m)	2 MHz (Np/m)
water	1486[a]		998[a]	3.5[c]		.025[b]	.10[b]
aluminum	6317	3128	2727	8.5[f]	3.048*	.025[e]	
acrylic	2760[d]		1182[d]	10[d]	2.362*		
steel	6100[a]		7700[a]		1.588		

Table A.1: Physical parameters for the materials used in this dissertation. *Plate thickness, unless otherwise specified. Sources of data: (a) Kinsler, *et al.*,[82] (b) Francois and Garrison,[83] (c) Beyer,[78] (d) Landsberger and Hamilton,[64] (e) Landsberger,[77] (f) Landolt-Bornstein.[81] All other data were determined in our laboratory.

A.5 Signal processing

The signal from the preamplifier was fed into a Tektronix RTD 710 digitizer, which samples with 10 bits of resolution at a maximum sampling frequency of 200 MHz. The input gain is also adjustable in discrete steps to maximize the signal-to-noise ratio of the digitized signal. We used a sampling frequency of 100

MHz, because the Nyquist frequency of 50 MHz is much higher than the response of the Marconi which rolls off higher than about 20 MHz.

Digitized waveforms were sent to the computer via a GPIB connection. The sampled waveform was usually 1024 points long (10.24 μs at the 100 MHz sampling frequency), and although the source waveforms were tone bursts, the portion of the received signal windowed was, as much as possible, in the steady state. A Blackman-Harris window was applied to the sampled waveform in order to more effectively discriminate among the harmonics.

Averaging was applied by the digitizer to increase the signal-to-noise ratio. Typically, averaging over 128 samples gave a sufficient signal to noise ratio (approximately 90 dB). However, for discriminating very low-amplitude signals up to 4096 samples were averaged. Even after averaging over 4096 samples, however, the signal-to-noise ratio is limited to about 100 dB because of word length of the digitizer output and windowing artifacts.

Appendix B

Full Expression for Nonlinear Generation in an Isotropic Layer

In this appendix we solve for the sum-frequency pressure that is generated in an isotropic plate due to normally-incident plane waves from opposite sides and radiated into the fluid. The solution of Eqn. (2.46) in Sec. 2.3.2 is

$$P^{(2)}(0 \le x \le l) = (\mathcal{H}x + \mathcal{C}_1)\, e^{-jk_+ x} + (\mathcal{I}x + \mathcal{C}_2)\, e^{jk_+ x} + \mathcal{J} e^{-jk_- x} + \mathcal{K} e^{jk_- x}\,, \tag{B.1}$$

where

$$\mathcal{H} = \frac{j\mathcal{D}}{2k_+}\,, \quad \mathcal{I} = -\frac{j\mathcal{E}}{2k_+}\,, \quad \mathcal{J} = \frac{\mathcal{F}}{k_+^2 - k_-^2}\,, \quad \mathcal{K} = \frac{\mathcal{G}}{k_+^2 - k_-^2}\,, \tag{B.2}$$

and $\mathcal{C}_1$ and $\mathcal{C}_1$ are the two homogeneous solutions of Eqn. (2.46). The pressure amplitudes of the waves radiated into the fluid are

$$P^{(2)} = \begin{cases} P^+_{\text{left}} e^{jk_{f+}} & x \le 0 \\ P^+_{\text{right}} e^{-jk_{f+}(x-l)} & x \ge l\,, \end{cases} \tag{B.3}$$

where $k_{f+} = \omega_+ / c_f$. Use of the one-dimensional linear momentum equation, Eqn. (2.3), in Eqns. (B.1) and (B.3) gives the particle velocity amplitude,

$$U^{(2)} = \begin{cases} -\frac{L_+}{z_f} e^{jk_{f+}x}\,, & x \le 0\,, \\ \left[(\mathcal{H}x + \mathcal{C}_1)\, e^{-jk_+ x} - (\mathcal{I}x + \mathcal{C}_2)\, e^{jk_+ x} + \frac{\omega_-}{\omega_+}\mathcal{J} e^{-jk_- x} - \frac{\omega_-}{\omega_+}\mathcal{K} e^{jk_- x}\right] / z_s\,, & \\ & 0 \le x \le l\,, \\ \frac{R_+}{z_f} e^{-jk_{f+}(x-l)}\,, & x \ge l\,. \end{cases} \tag{B.4}$$

We now apply boundary conditions. As in Secs. 2.1 and 2.2, pressure and particle velocity are equated across the interfaces $x = 0$ and $x = l$. Equating pressures across interfaces gives

$$\frac{P^+_{\text{left}}}{2} = \mathcal{C}_1 + \mathcal{C}_2 + \mathcal{J} + \mathcal{K} \tag{B.5}$$

at $x = 0$ and

$$\frac{P^+_{\text{right}}}{2} = (\mathcal{H}l + \mathcal{C}_1)\, e^{-jk_+l} + (\mathcal{I}l + \mathcal{C}_2)\, e^{jk_+l} + \mathcal{J}e^{-jk_-l} + \mathcal{K}e^{jk_-l} \tag{B.6}$$

at $x = l$. Equating particle velocities across the interfaces at $x = 0$ and $x = l$ yields

$$-\frac{z_s P^+_{\text{left}}}{2z_f} = \mathcal{C}_1 - \mathcal{C}_2 + \frac{\omega_-}{\omega_+}\mathcal{J} - \frac{\omega_-}{\omega_+}\mathcal{K} \tag{B.7}$$

at $x = 0$ and

$$\frac{z_s P^+_{\text{right}}}{2z_f} = (\mathcal{H}l + \mathcal{C}_1)\, e^{-jk_+l} - (\mathcal{I}l + \mathcal{C}_2)\, e^{jk_+l} + \frac{\omega_-}{\omega_+}\mathcal{J}e^{-jk_-l} - \frac{\omega_-}{\omega_+}\mathcal{K}e^{jk_-l} \tag{B.8}$$

at $x = l$.

Equations (B.5)–(B.8) may be solved for the four unknowns $P^+_{\text{left}}, P^+_{\text{right}}, \mathcal{C}_1$, and $\mathcal{C}_2$. The amplitudes P^+_{left} and P^+_{right} are

$$\begin{aligned}
P^+_{\text{left}} = -\Bigg\{ & j\left[\mathcal{J}\left(\frac{\omega_-}{\omega_+} - \frac{z_f}{z_s}\right) - \mathcal{K}\left(\frac{\omega_-}{\omega_+} + \frac{z_f}{z_s}\right)\right]\sin k_+l \\
&+ \left[\mathcal{J}\left(\frac{\omega_- z_f}{\omega_+ z_s} - 1\right) + \mathcal{K}\left(\frac{\omega_- z_f}{\omega_+ z_s} + 1\right)\right]\cos k_+l \\
&+ \mathcal{H}le^{-jk_+l}\left(1 - \frac{z_f}{z_s}\right) + \mathcal{I}le^{jk_+l}\left(1 + \frac{z_f}{z_s}\right) \\
&- \mathcal{J}e^{-jk_-l}\left(1 - \frac{\omega_- z_f}{\omega_+ z_s}\right) - \mathcal{K}e^{jk_-l}\left(1 + \frac{\omega_- z_f}{\omega_+ z_s}\right)\Bigg\}\Bigg/ \\
&\left[\cos k_+l + \frac{j}{2}\left(\frac{z_f}{z_s} + \frac{z_s}{z_f}\right)\sin k_+l\right],
\end{aligned} \tag{B.9}$$

and

$$\begin{aligned}
P^+_{\text{right}} = \Bigg\{ & j\left[\mathcal{J}e^{-jk_-l}\left(\frac{z_f}{z_s} + \frac{\omega_-}{\omega_+}\right) + \mathcal{K}e^{jk_-l}\left(\frac{z_f}{z_s} - \frac{\omega_-}{\omega_+}\right)\right]\sin k_+l \\
&+ \left[\mathcal{J}e^{-jk_-l}\left(1 + \frac{\omega_- z_f}{\omega_+ z_s}\right) + \mathcal{K}e^{jk_-l}\left(1 - \frac{\omega_- z_f}{\omega_+ z_s}\right)\right]\cos k_+l \\
&+ (\mathcal{H}l + \mathcal{I}l - \mathcal{J} - \mathcal{K}) + \frac{z_f}{z_s}(\mathcal{H}l - \mathcal{I}l - \mathcal{J} + \mathcal{K})\Bigg\}\Bigg/ \\
&\left[\cos k_+l + \frac{j}{2}\left(\frac{z_f}{z_s} + \frac{z_s}{z_f}\right)\sin k_+l\right],
\end{aligned} \tag{B.10}$$

where

$$\mathcal{H} = \frac{j\beta_s\omega_+}{2\rho_s c_s^3} A_1 A_2\,, \quad \mathcal{I} = -\frac{j\beta_s\omega_+}{2\rho_s c_s^3} B_1 B_2\,,$$
$$\mathcal{J} = \frac{(\beta_s - 1)\omega_+^2 - \omega_-^2}{(\omega_+^2 - \omega_-^2)\rho_s c_s^2} A_1 B_2\,, \quad \mathcal{K} = \frac{(\beta_s - 1)\omega_+^2 - \omega_-^2}{(\omega_+^2 - \omega_-^2)\rho_s c_s^2} B_1 A_2\,, \qquad \text{(B.11)}$$

and A_1, A_2, B_1, and B_2 are the first-order pressure amplitudes in the layer which were determined in Sec. 2.1. In Fig. B.1 we compare the full solution with the approximate solution as a function of f_1, with f_2 held at 2.06 MHz. Differences in both magnitude and phase between full and approximate expressions are small.

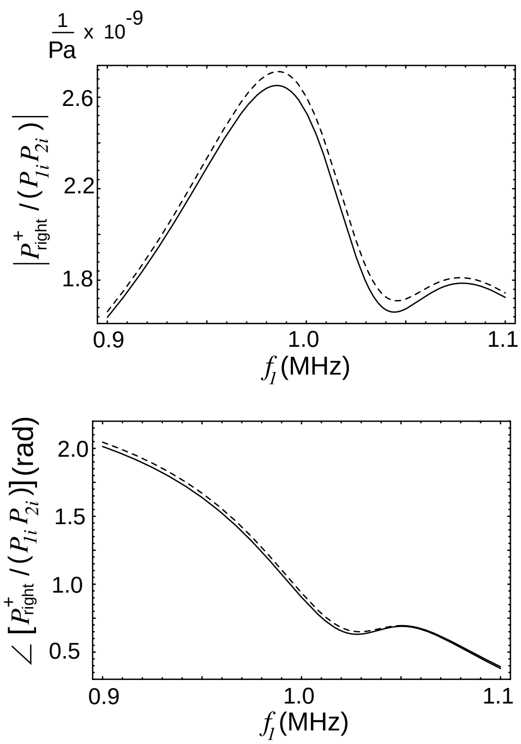

Figure B.1: Comparison of magnitude and phase of approximate expression for P^+_{right} (- - -) with full expression (——), for an aluminum plate, $f_2 = 2.10$ MHz.

Appendix C

Time Domain

In Chaps. 2 and 3 we considered the interaction of time-harmonic plane waves with plates. In this appendix we report investigations of the interaction of plane waves and sound beams with sawtooth waveforms normally incident upon plates. Linear theory is presented for interaction of a plane sawtooth wave with an isotropic layer and a layer with a defect, and experimental results are presented for the transmission of an intense, focused sound beam through a plate of aluminum.

This work is motivated partly by work by Hedberg and Rudenko, who examined the response of a layer to an incident pulse.[84] The authors considered nonlinear layers that were soft with respect to the surrounding medium, and were thin with respect to the length of the pulse so that resonance effects were not included. In this appendix, we consider only linear effects, and resonance effects are important.

C.1 Sawtooth Wave

According to weak shock theory for plane waves,[70] a time-harmonic plane wave for which nonlinear effects dominate over effects of thermoviscous absorption will eventually develop into a shock wave. This shock wave has a broad frequency spectrum. It is possible to exploit this property to probe a sample over a broad range of frequencies, which extends over the bandwidth of most sources.

The shock wave takes a sawtooth form. The waveform $p(t)$ is shown in Fig. C.1. The Fourier series representation for the shock wave (at the shock formation distance) is[70]

$$p(t) = p_0 \sum_{n=1}^{\infty} \frac{1}{n} \sin n\omega t \ , \tag{C.1}$$

where p_0 is the pressure amplitude of the undistorted wave. The amplitude of this wave decays with distance from the source, but here we are concerned only with the shape, and not the amplitude, of the waveform. According to Eqn. (C.1),

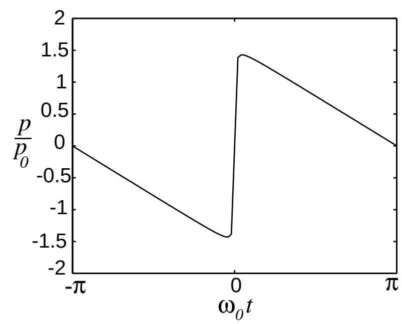

Figure C.1: Sawtooth wave.

the sawtooth wave contains harmonic components at angular frequencies $n\omega$, where ω is the frequency of the plane wave before steepening. The amplitudes of the frequency components are proportional to $1/n$. The shock front carries the high-frequency information, and it is sensitive to any changes in the distribution of the harmonics from Eqn. (C.1). It is reasonable to expect a change in the character of the shock front as it interacts with a layer.

C.1.1 Interaction model

We consider the transmission of a sawtooth wave in water at normal incidence through a layer with sound speed c_s and thickness l. The transmission coefficient is given by Eqn. (2.5), easily expressed as a function of frequency:

$$W(\omega) = \frac{P_t}{P_i} = \frac{1}{\cos\left(\frac{\omega l}{c_s}\right) + \frac{j}{2}\left(\frac{Z_f}{Z_s} + \frac{Z_s}{Z_f}\right)\sin\left(\frac{\omega l}{c_s}\right)}, \tag{C.2}$$

where P_i and P_t are amplitudes of time-harmonic incident and transmitted waves, respectively. We assume the harmonics of the sawtooth wave interact with the plate independently. In that case the transmitted pressure p_t is

$$p_t = 2A \sum_{n=1}^{\infty} \frac{1}{n} W(n\omega) \sin n\omega t \ , \tag{C.3}$$

where $W(n\omega)$ is the value of the transmission coefficient at angular frequency $n\omega$.

Waveforms of the transmitted sawtooth waves as the frequency is swept through the resonance at $f = 2.075$ MHz are shown in Fig. C.2. As the phases of the harmonics change when the primary frequency is swept through resonance, the waveform changes rapidly. When the primary frequency is at resonance, $f_0 = 2.075$ MHz (middle), the waveform is nearly indistinguishable from Fig. C.1. Figure C.2 indicates that the changes in the sawtooth waveform upon transmission through a plate may provide a sensitive means of determining the resonance frequency of the sample.

C.1.2 Experimental results

Experiments were performed using a focused source with effective source radius $a = 18$ mm and focal length $d = 162$ mm normally incident upon an aluminum plate, which is approximately 1/8 in. thick (properties for the plate are given in Table A.1). The resonance frequency of the source was 2.25 MHz. The source-plate distance was 150 mm, and the distance from the plate to the hydrophone was 20 mm.

A direct comparison between waveforms with and without the plate could not be made, because the pressure amplitude of the wave without the plate is high enough to overload the preamplifier. We use a well-tested time-domain computational model[85] to predict the waveform at the receiver with no plate between the source and receiver. The waveform is shown in Fig. C.3. Because of diffraction effects, the incident waveform does not achieve a sawtooth form. However, the predicted waveform indicates that a shock wave has formed, so the waveform contains significant high-frequency information.

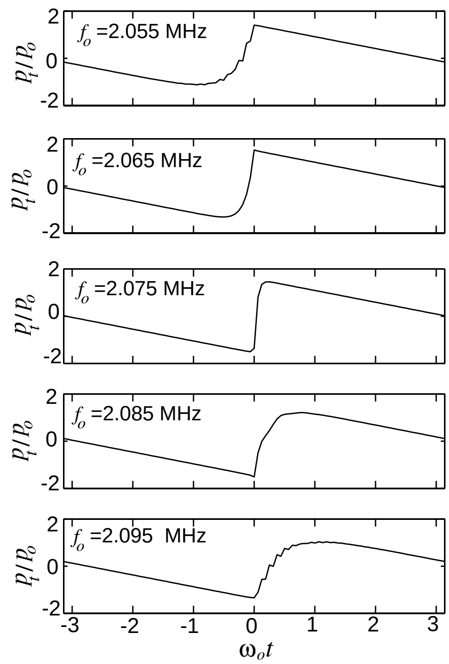

Figure C.2: Theory for sawtooth wave interacting with an aluminum plate. 100 harmonics are used. Properties for the plate are given in Table A.1.

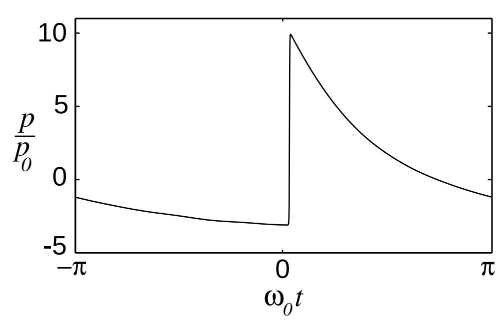

Figure C.3: Predicted waveform at 170 mm from a focused source, $a = 18$ mm, $d = 162$ mm, and $p_0 = 72$ kPa.

Figure C.4 shows the transmitted waveform for $f_0 = 1.98$ MHz to $f_0 = 2.28$ MHz. Although the results do not resemble Fig. C.2 for a plane wave, the waveform changes shape as the source frequency sweeps through the pass band. This is due to the shifting of the phases of the harmonics in the incident with respect to one another as the frequency is swept through the resonance. Another characteristic of Fig. C.2 is that the waveform is steepened, but not shocked as in Fig. C.3, indicating that the higher harmonics are attenuated significantly upon transmission through the plate. Also, changes the waveforms shown in Fig. C.4 occur over a range of about 0.2 MHz, whereas changes occur in the waveforms shown in Fig. C.2 over a range of about 0.01 MHz. It is possible that this disparity is due to the strong attenuation of the higher harmonics in the measured waveforms.

C.1.3 Plates with defects

The transmission of a plane sawtooth wave through bonded plates was also modeled. This was accomplished by replacing the transmission coefficient for an isotropic layer, Eqn. (C.2), with the transmission coefficient for a plate with a compliant planar boundary, derived in Chap. 3. Only linear phenomena are considered.

Predictions are shown in Fig. C.5. We first consider two bonded 1/16 in. aluminum plates (the bond is located at $\eta = x/l = 0.5$, left column). The stiffness is $K = 2 \times 10^{15}$ Pa/m, which was chosen because the effects of the defect are significant but the sawtooth character of the transmitted waveform is intact. As the excitation frequency sweeps from 0.985 MHz to the pass band at 0.995 MHz, a spike appears which is centered at $\omega t = 0$. As the frequency shifts above the pass band the spike starts to vanish. If the frequency is tuned to $f_2 \approx 2$ MHz, the spike does not appear. This is because the pressure is zero at the interface (as shown in Fig. 2.4 for $\lambda_2 = l$), so the spring boundary is not activated.

Next we consider bonded plates with different thicknesses. The total thickness of the bonded plates is 1/8 in., with the bond located at η (right column). Frequency is fixed at the pass band at 0.995 MHz. For $\eta = 0.1$, the spikes are

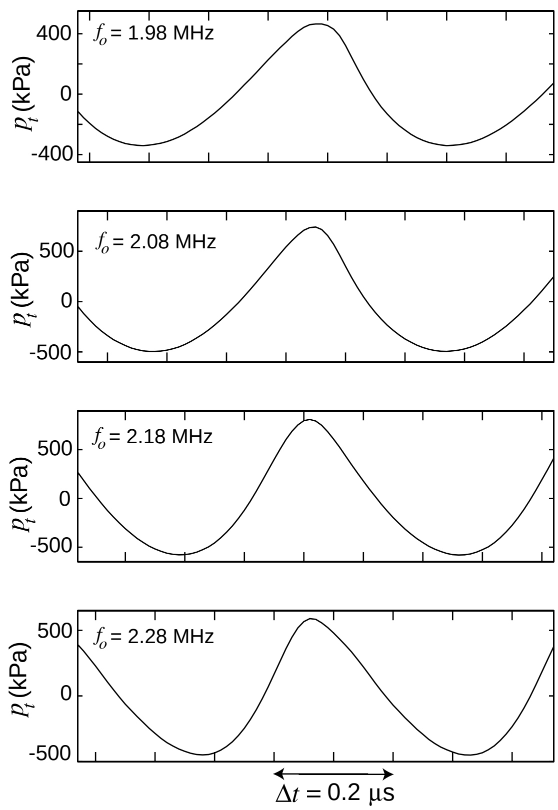

Figure C.4: Measurement of waveforms transmitted through aluminum plate.

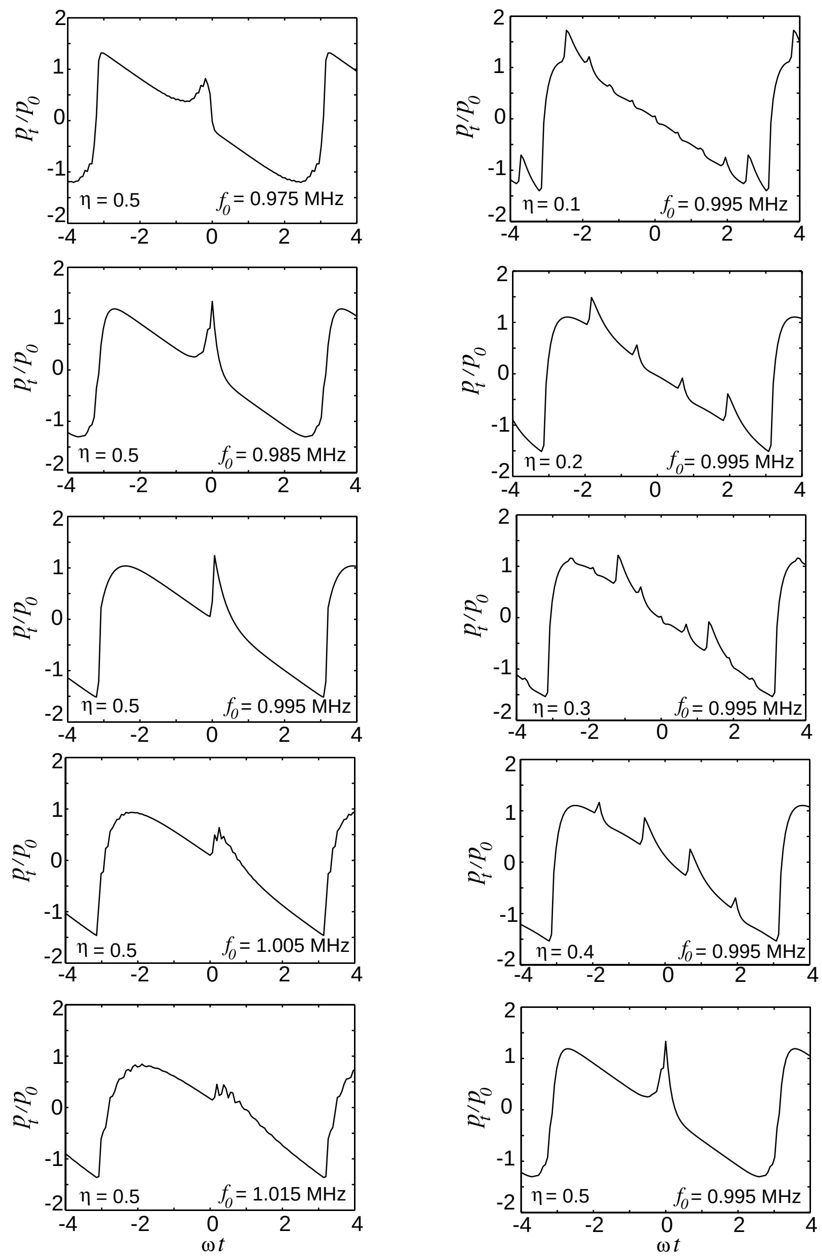

Figure C.5: Predicted waveforms for varied fundamental frequency f_0 (left column) and bond at $\eta = x/l$ (right column) through two aluminum plates joined with bond with stiffness $K = 2 \times 10^{15}$ Pa/m. Total thickness is $l = 1/8$ in.

near the maximum and minimum pressures on the waveform. As the bond is moved towards the center of the plates ($\eta = 0.5$) the spikes grow in magnitude and approach $\omega t = 0$. This result suggests that it may be possible to localize the position of a crack or defect by examining the received waveform.

Bibliography

[1] Y. Zheng, R. G. Meav, and I. Y. Solodov, "Nonlinear acoustic applications for material characterization: A review," *Canadian Journal of Physics* **77,** 927–967 (1999).

[2] V. E. Nazarov and L. A. Ostrovsky, "Elastic waves in media with strong acoustic nonlinearity," *Sov. Phys. Acoust.* **36,** 57–60 (1990).

[3] D. E. Chimenti, "Guided waves in plates and their use in materials characterization," *Appl. Mech. Rev.* **50,** 247–284 (1997).

[4] M. A. Breazeale and J. Philip, "Determination of third-order elastic constants from ultrasonic harmonic generation measurements," in *Physical Acoustics*, edited by W. P. Mason and R. Thurston (Academic Press, 1984), Vol. 17.

[5] A. N. Norris, "Finite-amplitude waves in solids," in *Nonlinear Acoustics*, edited by M. F. Hamilton and D. T. Blackstock (Academic Press, New York, 1998), Chap. 9.

[6] L. A. Ostrovsky, "Wave processes in media with strong acoustic nonlinearity," *J. Acoust. Soc. Am.* **90,** 3332–3337 (1991).

[7] V. Y. Zaitsev, V. E. Nazarov, and I. Y. Belyaeva, "The equation of state of a microinhomogeneous medium and the frequency dependence of its elastic nonlinearity," *Acoust. Phys.* **47,** 178–183 (2001).

[8] V. Y. Zaitsev, "A model of anomalous elastic nonlinearity of microinhomogenous media," *Acoust. Lett.* **19,** 171–174 (1996).

[9] V. E. Nazarov, L. A. Ostrovsky, I. A. Soustova, and A. M. Sutin, "Nonlinear acoustics of micro-inhomogeneous media," *Physics of the Earth and Planetary Interiors* **50,** 65–73 (1988).

[10] A. S. Korotkov, M. M. Slavinskii, and A. M. Sutin, "Variations of acoustic nonlinear parameters with the concentration of defects in steel," *Acoust. Phys.* **40,** 71–74 (1994).

[11] V. Y. Zaitsev, A. M. Sutin, I. Y. Belyaeva, and V. E. Nazarov, "Nonlinear interaction of acoustical waves due to cracks and its possible usage for cracks detection," *J. Vib. Control* **1,** 335–344 (1995).

[12] V. E. Nazarov and A. M. Sutin, "Nonlinear elastic constants of solids with cracks," *J. Acoust. Soc. Am.* **102,** 3349–3354 (1997).

[13] L. Adler and C. Mattei, "Impacts of nonlinear acoustics on nondestructive evaluation and acousto-optics," in *Nonlinear Acoustics at the Turn of the Millenium: ISNA 15*, edited by W. Lauterborn and T. Kurz (2000), pp. 317–320.

[14] R. A. Guyer and P. A. Johnson, "Nonlinear mesoscopic elasticity: Evidence for a new class of materials," *Physics Today* **52,** 30–36 (April 1999).

[15] I. Y. Belyaeva, L. A. Ostrovsky, and E. M. Timanin, "Experiments on harmonic generation in grainy media," *Acoust. Lett.* **15,** 221–224 (1992).

[16] I. Y. Belyaeva, V. Y. Zaitsev, and L. A. Ostrovsky, "Nonlinear acoustoelastic properties of granular media," *Acoust. Phys.* **39,** 11–15 (1993).

[17] I. Y. Belyaeva, V. Y. Zaitsev, and E. M. Timanin, "Experimental study of nonlinear elastic properties of granular media with nonideal packing," *Acoust. Phys.* **40,** 789–793 (1994).

[18] V. Y. Zaitsev, "Nonideally packed granular media: Numerical modeling of elastic nonlinear properties," *Acoust. Phys.* **41,** 385–391 (1995).

[19] I. N. Didenkulov, A. M. Sutin, V. V. Kakazov, A. E. Ekimov, and S. W. Yoon, "Nonlinear acoustic technique of crack location," in *Nonlinear Acoustics at the Turn of the Millenium: ISNA 15*, edited by W. Lauterborn and T. Kurz (2000), pp. 329–332.

[20] K. R. McCall and R. A. Guyer, "A new theoretical paradigm to describe hysteresis, discrete memory and nonlinear elastic wave propagation in rock," *Nonlinear Processes in Geophysics* **3,** 89–101 (1996).

[21] K. Van den Abeele, P. A. Johnson, R. A. Guyer, and K. R. McCall, "On the quasi-analytic treatment of hysteretic nonlinear response in elastic wave propagation," *J. Acoust. Soc. Am.* **101,** 1885–1898 (1997).

[22] J. S. Popovics and J. L. Rose, "A survey of developments in ultrasonic NDE of concrete," *IEEE Trans. Ultrasonics, Ferroelectrics, and Freq. Control* **41,** 140–143 (1994).

[23] K. Van den Abeele and J. De Visscher, "Damage assessment in reinforced concrete using spectral and temporal nonliner vibration techniques," *Cement and Concrete Research* **30,** 1453–1464 (2000).

[24] I. N. Didenkulov, A. M. Sutin, A. E. Ekimov, and V. V. Kakazov, "Interaction of sound and vibrations in concrete with cracks," in *Nonlinear Acoustics at the Turn of the Millenium: ISNA 15*, edited by W. Lauterborn and T. Kurz (2000), pp. 279–282.

[25] J. Chen, W. Jiang, and Y. Shui, "Observation of nonlinear acoustic effects at isotropic solid-solid interfaces," *J. Acoust. Soc. Am.* **109,** 501–507 (2001).

[26] K. S. Len, F. M. Severin, and I. Y. Solodov, "Experimental observation of the influence of contact nonlinearity on the reflection of bulk acoustic waves and the propagation of surface acoustic waves," *Sov. Phys. Acoust.* **37,** 610–612 (1991).

[27] K. S. Len and I. Y. Solodov, "Nonlinear reflection of surface waves at a contact interface between two solids," *Sov. Phys. Acoust.* **39,** 149–151 (1993).

[28] J. M. Richardson, "Harmonic Generation at an Unbonded Interface—I. Planar interface between semi-infinite elastic media," *Int. J. Engng. Sci.* **17,** 73–85 (1979).

[29] O. Buck, W. L. Morris, and J. M. Richardson, "Acoustic harmonic generation at unbonded interfaces and fatigue cracks," *Appl. Phys. Lett.* **33,** 371–373 (1978).

[30] O. V. Rudenko and C. A. Vu, "Nonlinear acoustic properties of a rough surface contact and acoustodiagnostics of a roughness height distribution," *Acoust. Phys.* **40,** 593–596 (1994).

[31] F. M. Severin and I. Y. Solodov, "Experimental observation of acoustic demodulation in reflection from a solid-solid interface," *Sov. Phys. Acoust.* **35,** 447–448 (1989).

[32] I. Y. Solodov and C. A. Vu, "'Popping' nonlinearity and chaos in vibrations of a contact interface between solids," *Acous. Phys.* **39,** 476–479 (1993).

[33] I. Y. Solodov, "Ultrasonics of non-linear contacts: propagation, reflection, and NDE-applications," *Ultrasonics* **36,** 383–390 (1998).

[34] L. D. Landau and E. M. Lifshitz, *Theory of Elasticity* (Pergamon Press Ltd., New York, 1986).

[35] J. D. Achenbach and O. K. Parikh, "Ultrasonic analysis of nonlinear response and strength of adhesive bonds," *J. Adhesion Sci. Technol.* **5,** 601–618 (1991).

[36] S. Hirsekorn, "Nonlinear transfer of ultrasound by adhesive joints—a theoretical description," *Ultrasonics* **39,** 57–68 (2001).

[37] M. Rothenfusser, M. Mayr, and J. Baumann, "Acoustic nonlinearities in adhesive joints," *Ultrasonics* **38,** 322–326 (2000).

[38] H. Lamb, "On waves in an elastic plate," *Proc. Roy. Soc. A* **93,** 114–128 (1917).

[39] S. K. Datta, A. H. Shah, R. L. Bratton, and T. Chakraborty, "Wave propagation in laminated composite plates," *J. Acoust. Soc. Am.* **83,** 2020–2026 (1988).

[40] M. D. Seale, B. T. Smith, W. H. Prosser and J. N. Zalameda, "Lamb wave assessment of fiber volume fraction in composites," *J. Acoust. Soc. Am.* **104,** 1399–1403 (1998).

[41] V. Dayal and V. K. Kinra, "Leaky Lamb waves in an anisotropic plate. I: An exact solution and experiments," *J. Acoust. Soc. Am.* **85,** 2268–2276 (1989).

[42] V. Dayal and V. K. Kinra, "Leaky Lamb waves in an anisotropic plate. II: Nonestructive evaluation of matrix cracks in fiber-reinforced composites," *J. Acoust. Soc. Am.* **89,** 1590–1598 (1991).

[43] L. G. Merkulov, "Damping of normal modes in a plate immersed in a liquid," *Sov. Phys. Acoust.* **10,** 169–173 (1964).

[44] W. J. de Lima, "Harmonic generation in isotropic elastic waveguides," Ph.D. Dissertation, The University of Texas at Austin, 2000.

[45] V. A. Schoch, "Der Schalldurchgang durch Platten," *Acustica* **2,** 1–17 (1952).

[46] W. Madigosky and R. Fiorito, "Modal resonance analysis of acoustic transmission and reflection losses in viscoelastic plates," *J. Acoust. Soc. Am.* **65,** 1105–1115 (1979).

[47] R. Fiorito and H. Überall, "Resonance theory of acoustic reflection and transmission through a fluid layer," *J. Acoust. Soc. Am.* **65,** 9–14 (1979).

[48] R. Fiorito, W. Madigosky, and H. Überall, "Resonance theory of acoustic waves interacting with an elastic plate," *J. Acoust. Soc. Am.* **66,** 1857–1866 (1979).

[49] R. Fiorito, W. Madigosky, and H. Überall, "Acoustic resonances and the determination of the material parameters of a viscous fluid layer," *J. Acoust. Soc. Am.* **69,** 897–903 (1979).

[50] R. Fiorito, W. Madigosky, and H. Überall, "An exact resonance decomposition of the acoustic transmission and reflection coefficients of a fluid layer," *J. Acoust. Soc. Am.* **79,** 222–229 (1986).

[51] G. Guidarelli, A. Marini, and L. Palmieri, "Ultrasonic method for determining attenuation coefficients in plate-shaped materials," *J. Acoust. Soc. Am.* **94,** 1476–1481 (1993).

[52] G. Guidarelli, A. Marini, and L. Palmieri, "Experimental method for investigating the acoustic transmissivity of fluid-loaded elastic plates," *Acoust. Lett.* **15,** 1–7 (1991).

[53] G. R. Barnard, J. L. Bardin, and J. W. Whiteley, "Acoustic reflection and transmission characteristics for thin plates," *J. Acoust. Soc. Am.* **57,** 577–584 (1975).

[54] V. A. Schoch, "Seitliche versetzung eines total reflektierten strahls bei ultraschwellen," *Acustica* **2,** 18–19 (1952).

[55] W. G. Neubauer, "Ultrasonic reflection of a bounded beam at Rayleigh and critical angles for a plane liquid-solid interface," *J. Appl. Phys.* **44,** 48–55 (1973).

[56] H. L. Bertoni and T. Tamir, "Unified theory of Rayleigh-angle phenomena for acoustic beams at liquid-solid interfaces," *J. Appl. Phys.* **2,** 157–172 (1973).

[57] T. D. K. Ngoc and W. G. Mayer, "Numerical integration method for reflected beam profiles near Rayleigh angle," *J. Acoust. Soc. Am.* **67,** 1149–1152 (1980).

[58] T. J. Plona, L. E. Pitts, and W. G. Mayer, "Ultrasonic bounded beam reflection and transmission effects at a liquid/solid-plate/liquid interface," *J. Acoust. Soc. Am.* **59,** 1324–1328 (1976).

[59] M. Rousseau and P. Gatignol, "Asymptotic analysis of nonspecular effects for the reflection and the transmission of a Gaussian acoustic beam incident on a solid plate," *J. Acoust. Soc. Am.* **80,** 325–332 (1986).

[60] A. L. V. Buren and M. A. Breazeale, "Reflection of finite-amplitude ultrasonic waves. II. Phase shift," *J. Acoust. Soc. Am.* **44,** 1014–1020 (1968).

[61] T. D. K. Ngoc, K. R. King, and W. G. Mayer, "A numerical model for nonlinear and attenuative propagation and reflection of an ultrasonic bounded beam," *J. Acoust. Soc. Am.* **81,** 874–880 (1987).

[62] S. Sato, "Second harmonic component in focused ultrasound transmitted through a solid plate," in *Nonlinear Acoustics at the Turn of the Millenium: ISNA 15*, edited by W. Lauterborn and T. Kurz (2000), pp. 199–202.

[63] V. E. Nazarov, "Frequency doubling of an acoustic wave on a nonlinear layer," *Sov. Phys. Acoust.* **36,** 398–399 (1990).

[64] B. J. Landsberger and M. F. Hamilton, "Second-harmonic generation in sound beams reflected from, and transmitted through, immersed elastic solids," *J. Acoust. Soc. Am.* **109,** 488–500 (2001).

[65] D. T. Blackstock, "Propagation of plane sound waves of finite amplitude in nondissipative fluids," *J. Acoust. Soc. Am.* **34,** 9–30 (1962).

[66] D. T. Blackstock, *Fundamentals of Physical Acoustics* (John Wiley and Sons, Inc., New York, 2000).

[67] M. F. Hamilton, "Model Equations," in *Nonlinear Acoustics*, edited by M. F. Hamilton and D. T. Blackstock (Academic Press, New York, 1998), Chap. 3.

[68] R. T. Beyer, "Parameter of nonlinearity in fluids," *J. Acoust. Soc. Am.* **32,** 719–721 (1960).

[69] P. K. Morse and K. U. Ingard, *Theoretical Acoustics* (Princeton University Press, Princeton, New Jersey, 1968), p. 377.

[70] D. T. Blackstock, M. F. Hamilton, and A. D. Pierce, "Progressive Waves in Lossless and Lossy Fluids," in *Nonlinear Acoustics*, edited by M. F. Hamilton and D. T. Blackstock (Academic Press, New York, 1998), Chap. 4.

[71] J. D. Achenbach, O. K. Parikh, and D. A. Sotiropoulos, "Nonlinear effects in the reflection from adhesive bonds," in *Review of Progress in Quantitative NDE*, edited by D. O. Thompson and D. E. Chimenti (Plenum Press, 1989), Vol. 8B, pp. 1401–1407.

[72] K. F. Graff, *Wave motion in elastic solids* (Dover Publications, New York, 1975).

[73] J. W. Goodman, *Introduction to Fourier Optics* (McGraw-Hill, Inc., New York, 1968).

[74] L. M. Brekhovskikh, *Waves in Layered Media* (Academic Press, New York, 1980).

[75] M. A. Averkiou, "Experimental investigation of propagation and reflection phenomena in finite amplitude sound beams," Ph.D. Dissertation, The University of Texas at Austin, 1993.

[76] J. A. TenCate, "Scattering of sound by sound: nonlinear interaction of colinear and noncolinear sound beams," Ph.D. Dissertation, The University of Texas at Austin, 1992.

[77] B. J. Landsberger, "Second harmonic generation in sound beams reflected from and transmitted through immersed elastic solids," Ph.D. Dissertation, The University of Texas at Austin, 1997.

[78] R. T. Beyer, "The parameter B/A," in *Nonlinear Acoustics*, edited by M. F. Hamilton and D. T. Blackstock (Academic Press, New York, 1998), Chap. 2.

[79] J. Naze Tjøtta, S. Tjøtta, and E. H. Vefring, "Propagation and interaction of two collinear finite-amplitude sound beams," *J. Acoust. Soc. Am.* **88,** 2859–2870 (1990).

[80] T. S. Hart and M. F. Hamilton, "Nonlinear effects in the focused sound beams," *J. Acoust. Soc. Am.* **84,** 1488–1496 (1988).

[81] Landolt-Bornstein, *Numerical Data and Functional Relationships in Science and Technology*, Vol. 11 of *New Series* (Springer–Verlag, New York, 1979).

[82] L. E. Kinsler, A. R. Frey, A. B. Coppens, and J. V. Sanders, *Fundamentals of Acoustics* (John Wiley and Sons, New York, 1982).

[83] R. E. Francois and G. R. Garrison, "Sound absorption based on ocean measurements. Part II: Boric acid contribution and equation for total absorption," *J. Acoust. Soc. Am.* **72,** 1879–1890 (1982).

[84] C. M. Hedberg and O. V. Rudenko, "Pulse response of a nonlinear layer," *J. Acoust. Soc. Am.* **110,** 2340–2350 (2001).

[85] M. A. Averkiou and M. F. Hamilton, "Nonlinear distortion of short pulses radiated by plane and focused circular pistons," *J. Acoust. Soc. Am.* **102,** 2539–2548 (1997).

VITA

Steven Joseph Younghouse was born on July 23, 1972 and raised in Boonton, New Jersey, the son of Lawrence and Mary Younghouse. After graduating from Boonton High School in 1990 he was admitted into Cornell University. He graduated from Cornell University in 1994 with a degree in Applied and Engineering Physics. He was admitted into the Graduate School of The University of Texas in the fall of 1994, and received the degree of Master of Science in Mechanical Engineering in the area of Acoustics in 1998. He currently lives in Austin with his wife Cynthia and dog Stinky.

Permanent address: Austin, Texas

This dissertation was typeset* with LaTeX by the author.
